

# Efficient and Open-Source Tool for the Prediction of Thermowell Structural Response



**Swansea University**  
**Prifysgol Abertawe**

**Callum Lloyd Jones, MPhys (Hons)**

Submitted to Swansea University in fulfilment of the requirements for an MPhil in Materials  
Engineering

**September 2023**

Faculty of Science and Engineering  
Swansea University

Copyright: The Author, Callum Lloyd Jones, 2023

# Abstract

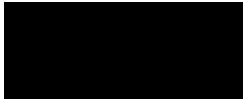
Thermowells are widely used in the aid of the measurement of temperature in high velocity or corrosive flow in large industrial installations. They are susceptible to vortex induced vibration which can be a cause of two types of damage; fatigue failure and resonance failure. Hence it is important to understand the mechanisms that may avoid vortex induced vibration as failure of a thermowell can cause a leak in the pipe or vessel it is installed on. An industry standard for the sizing and installation of a thermowell in order to avoid failure due to vortex induced vibration, hydrostatic pressure or static bending already exists. The standard is thorough and has been amended as recently as 2016 in order to increase safety in working with thermowells. However, it has its shortcomings with some assumptions it makes and when considering unique designs. A unique design of particular interest from industry is that of a cylindrical well with helical strakes attached. This affects the boundary layer of the fluid on the thermowell.

In this work, a novel tool is developed for computing the structural response of a thermowell depending on the flow environment in which it is placed in. The tool exploits one-way coupling requiring the physics of fluid flow and solid dynamics. The incompressible Navier-Stokes equations with a RANS turbulence model and a structural modal superposition method are used to solve for the fluid and the solid. An experimental setup was also proposed with the purpose of benchmarking the numerical approach, however, experimental testing was not pursued.

The numerical model showed a significant reduction in time dynamic oscillatory force being applied to the thermowell when helical strakes are introduced but an increase in steady state force. Therefore, with the presence of helical strakes, the dynamics stress levels that the thermowell experiences is reduced making the thermowell less susceptible to failure.


**Declarations**

This work has not previously been accepted in substance for any degree and is not being concurrently submitted in candidature for any degree.

Signed....  .....


Date.....30/09/23.....

This thesis is the result of my own investigations, except where otherwise stated. Other sources are acknowledged by footnotes giving explicit references. A bibliography is appended.

Signed...  .....


Date.....30/09/23.....

I hereby give consent for my thesis, if accepted, to be available for electronic sharing

Signed...  .....

Date.....30/09/23.....

The University's ethical procedures have been followed and, where appropriate, that ethical approval has been granted.

Signed..  .....

Date.....30/09/23.....

# Contents

<b>List of Figures</b>	<b>vi</b>
<b>List of Tables</b>	<b>xii</b>
<b>1 Introduction</b>	<b>1</b>
1.1 Background and Motivation . . . . .	1
1.2 Understanding Thermowell Design and Function . . . . .	2
1.3 Traditional Thermowell Design Problems . . . . .	5
1.4 State of the Art . . . . .	6
1.4.1 Computational Fluid Dynamics . . . . .	7
1.4.2 Fluid Structure Interaction . . . . .	13
1.4.3 Experimental Studies . . . . .	15
1.5 Thesis Overview . . . . .	17
1.5.1 Objectives . . . . .	17
1.5.2 Thesis Outline . . . . .	18
<b>2 Industrial Application</b>	<b>20</b>
2.1 Industry Standards . . . . .	20
2.1.1 Frequency Check . . . . .	22
2.1.2 Dynamic Stress Check . . . . .	27
2.1.3 Steady Stress Check . . . . .	28
2.1.4 Pressure Stress Check . . . . .	29
2.1.5 Assumptions in the Industry Standards . . . . .	29
2.2 Proposal for Experimental Validation Study . . . . .	31
2.2.1 Existing Experimental Set Up . . . . .	31
2.2.2 Assessing Existing Set-up Capability . . . . .	32

2.2.3	Proposed Modifications . . . . .	35
2.3	Conclusions . . . . .	37
<b>3</b>	<b>Fluid Mechanics Computational Modelling</b>	<b>39</b>
3.1	Aspects of Fluid Mechanics . . . . .	39
3.1.1	Conservation Laws . . . . .	39
3.1.2	Constitutive laws . . . . .	42
3.1.3	Turbulence . . . . .	43
3.1.4	Physical Boundary Conditions . . . . .	45
3.1.5	Relevant Parameters . . . . .	48
3.1.6	Wall Functions . . . . .	51
3.2	Computational Fluid Dynamics . . . . .	52
3.2.1	Software . . . . .	53
3.2.2	Spatial Discretisation . . . . .	53
3.2.3	Finite Volume Method for Unsteady Flows . . . . .	54
3.2.4	Numerical Schemes . . . . .	55
3.2.5	Indicators of Discretisation Quality . . . . .	57
3.3	Conclusions . . . . .	61
<b>4</b>	<b>Structural Mechanics Computational Modelling</b>	<b>62</b>
4.1	Aspects of Solid Mechanics . . . . .	62
4.1.1	Continuum Mechanics . . . . .	62
4.2	Boundary Load Transfer . . . . .	68
4.2.1	Newmark-beta Time Integration . . . . .	69
4.3	Reduced Order Model . . . . .	70
4.4	Implementation . . . . .	74
4.5	Conclusions . . . . .	74
<b>5</b>	<b>Numerical Results</b>	<b>76</b>
5.1	Fluid Model Benchmarking . . . . .	76
5.1.1	2D Fluid Model . . . . .	77
5.1.2	2D Fluid Results . . . . .	80
5.1.3	3D Fluid Model . . . . .	86
5.1.4	3D Fluid Results . . . . .	90

5.2	Fluid Structure Interaction for Finite Height Geometries . . . . .	95
5.2.1	Flow Modelling Results . . . . .	102
5.2.2	Frequency Response of the Structure . . . . .	109
5.2.3	Solid Solver Benchmarking . . . . .	109
5.2.4	Results of the Solid Solver . . . . .	117
5.3	Discussion and Outputs . . . . .	121
5.3.1	Significance of the Results . . . . .	121
<b>6</b>	<b>Conclusions</b>	<b>123</b>
6.1	Completion of Research Objectives . . . . .	123
6.2	Closure of the Work . . . . .	125
6.3	Future Work . . . . .	125
	<b>References</b>	<b>128</b>

# List of Figures

1.1	Diagram of a thermowell labelled by parts. . . . .	2
1.2	Different types of thermowells. (a) Threaded with stepped shank (b) Flanged with straight shank (c) Flanged with helical shank (d) Welded with tapered shank (e) Sanitary insert with straight shank. . . . .	3
1.3	Diagram of a thermowell installed with a stand-off mechanism. . . . .	5
2.1	A schematic diagram of both types of thermowell stems and the labels corresponding to each part of the thermowells. These diagrams are found in [3].	21
2.2	Plot of the Strouhal number vs Reynolds number defined by (2.2) in [3]. . . . .	23
2.3	Current experimental set up of the study which needs to be adapted to a high flow rate/ low pressure flow past a thermowell. . . . .	31
2.4	Set of of the proposed rig. . . . .	36
3.1	(a) Diagram to aid the descriptive definition of non orthogonality using surface normal at the common face centre and the vector connecting cell centroids. (b) Diagram to aid non orthogonality definition using surface normal at the common face centre and the vector connecting cell centroid to face centre. . . . .	59
3.2	Diagram to aid non orthogonality definition using surface normal at the common face centre and the vector connecting cell centroid to face centre. . . . .	60
4.1	3D set up for flow around a cylinder for a straight cylinder with labelled boundaries. . . . .	63
4.2	Illustration of how NPIM is implemented in 2D. Where the red dashed lines (---) represent the fluid boundary edges and the black dashed lines (---) represent the solid boundary edges. The corresponding crosses represent the face centres. . . . .	69

5.1	Domain of the 2D flow problem with labelled boundaries and dimensions. . . . .	77
5.2	Visualisation of the 2D mesh used in benchmarking. . . . .	78
5.3	Results for a mesh independency test for a 2D cylinder using the number of elements in the mesh vs (a) average drag coefficient (b) Root mean squared of the lift coefficient. . . . .	80
5.4	(a) Contour plot of velocity magnitude in the surface plane with a normal in the z direction at $Re = 50$ with the colour bar and range shown in the units $\text{ms}^{-1}$ . (b) Streamline plot of velocity flowing around a 2D cylinder for $Re = 50$ . . . . .	81
5.5	Contour plot of velocity magnitude in the surface plane with a normal in the z direction with relevant colour bars and ranges shown in the units $\text{ms}^{-1}$ . . . . .	82
5.6	Streamline plot of velocity flowing around a 2D cylinder for various input velocities and Reynolds numbers. . . . .	82
5.7	Plots to show (a) the time history of the lift (—) and drag (—) coefficient in the 2D fluid simulations at $Re = 50$ . Lift and drag are found using (3.21a) and (3.21b). (b) The discrete Fourier transform of the lift coefficient with respect to frequency in order to observe what frequencies of vortex shedding are present in the 2D fluid simulations at $Re = 50$ . . . . .	83
5.8	Plots to show the time history of the lift (—) and drag (—) coefficient in the 2D fluid simulations. Lift and drag are found using (3.21a) and (3.21b). . . . .	84
5.9	Plots to show the discrete Fourier transform of the lift coefficient with respect to frequency in order to observe what frequencies of vortex shedding are present in the 2D fluid simulations. . . . .	85
5.10	Plots to show the obtained Strouhal number of the wake of the fluid (●) for each simulation with respect to the flows Reynolds number compared with the expected Strouhal number trend line (—) defined in [3]. . . . .	85
5.11	3D set up for flow around a cylinder for a straight cylinder with labelled boundaries. . . . .	87
5.12	(a) Planar surface cut of the mesh displaying the different regions of refinement. (b) 3D mesh surface for the flow around a long cylinder with the inlet and outlet surfaces missing. The units of measurement are in mm. . . . .	88



5.13	Results for a mesh independency test for a cylinder of infinite height using the number of elements in the mesh vs (a) average drag coefficient (b) Root mean squared of the lift coefficient. . . . .	89
5.14	Above view of the 2D planar contour plots representing the scalar velocity magnitude. Each plane was in passed through the centre height of the cylinder. The colour bars and ranges are displayed separately for each case with the ranges in units $\text{ms}^{-1}$ . . . . .	91
5.15	Side view of the 2D planar contour plots representing the scalar velocity magnitude. The colour bars and ranges are displayed separately for each case with the ranges in units $\text{ms}^{-1}$ . . . . .	91
5.16	Plot of isovolumes of the turbulent viscosity $\nu_t$ at a Reynolds number of $1 \times 10^5$ .	92
5.17	Plots to show the time history of the lift (—) and drag (—) coefficient in the 3D fluid simulations at various Reynolds numbers. Lift and drag are found using (3.21a) and (3.21b). . . . .	93
5.18	Plots to show the discrete Fourier transform of the lift coefficient with respect to frequency of vortex shedding are present in the 3D fluid simulations. . . . .	94
5.19	(a) Strouhal number vs Reynolds number for a range of Reynolds numbers up to $1 \times 10^6$ . The black markers (●) represent the experimental findings from various studies reported in [57, 58]. The results from all the simulations are displayed as (●). (b) Average Drag Coefficient vs Reynolds number for a range of Reynolds numbers up to $1 \times 10^7$ . The black markers (●) represent the experimental findings from various studies reported in [64]. The results from the 3D simulation are displayed as (●). . . . .	95
5.20	Workflow of the fluid-structure interaction tool from the geometry creation to the time varying displacement vector field. . . . .	97
5.21	Sketch of the fluid domain with labelled boundaries for each case of finite height geometry. . . . .	98
5.22	(a) Above view of the planar surface cut displaying the mesh for straight cylinder. (b) Side view of the Planar surface cut displaying the mesh for straight cylinder. All measurements are in the units mm. . . . .	99
5.23	Planar surface cuts of the inflation layers for (a) Straight cylinder (b) Helical Cylinder. . . . .	100

5.24	Results for a mesh independency test for a straight cylinder of finite height using the number of elements in the mesh vs (a) average drag coefficient (b) Root mean squared of the lift coefficient. . . . .	101
5.25	Comparison for the isovolumes of the turbulent viscosity $\nu_t$ at a Reynolds number of $1 \times 10^5$ . (a) Flow around a straight cylinder. (b) Flow around a cylinder with sharp finned helical strakes. . . . .	103
5.26	Comparison for the planar surface streamlines of the fluid velocity at a Reynolds number of $1 \times 10^5$ for a straight cylinder vs a cylinder with helical strakes. (a) Straight cylinder (b) Helical cylinder. . . . .	103
5.27	Comparison for the planar contour plots of the fluid velocity magnitude at a Reynolds number of $1 \times 10^5$ for (a) a straight cylinder vs (b) a cylinder with helical strakes. Separate colour bars and ranges are displayed with the units of $\text{ms}^{-1}$ . . . . .	104
5.28	Plots of the lift (—) and drag (—) coefficients of the forces acting on the cylinder for various Reynolds numbers. Lift and drag are found using (3.21a) and (3.21b). . . . .	105
5.29	Plots of the discrete Fourier transform of the lift coefficient of the force acting on the cylinder before (—) and after interpolation (—) for various Reynolds numbers. . . . .	106
5.30	Plots of the lift (—) and drag (—) coefficients of the forces acting on the cylinder with helical strakes for various Reynolds numbers. Lift and drag are found using (3.21a) and (3.21b). . . . .	107
5.31	Plots of the discrete Fourier transform of the lift coefficient of the force acting on the cylinder before (—) and after interpolation (—) for various Reynolds numbers. Steady state term at 0 Hz is ignored for scaling. . . . .	108
5.32	Solid domain $\Omega$ used for the benchmarking for the reduced order solid solver. Displaying the Dirichlet boundary, $\partial\Omega_D$ , with a fixed face and the face, $\partial\Omega_f$ , receiving the known trial time varying force vectors. . . . .	109
5.33	Mode shapes of the simple sold structure and the corresponding modal frequency with the displacement scaled by an arbitrary value. . . . .	110

5.34	(a) Time history of a displacement of a solid structure while applying time varying arbitrary load. Solved using Newmark time integration (—) and then comparing by solving the FFT method for 4 modes (—), 3 modes (—), 2 modes (—), 1 modes (—) (b) The time averaged absolute error of the displacement of the selected node against how many modes are solved for. . . . .	111
5.35	The first 4 mode shapes of the straight cylinder and the corresponding modal frequency with the displacement scaled by an arbitrary value. . . . .	111
5.36	The first 4 mode shapes of the cylinder with helical strakes and the corresponding modal frequency with the displacement scaled by an arbitrary value. . . . .	112
5.37	Plots of the results of a grid refinement study on the mapping process of fluid forces. (a) shows L2 vs axial divisions. (b) shows L2 vs circumferential divisions.	113
5.38	Solid domain displaying the hollow nature of the (a) straight cylinder (b) helical cylinder displaying Dirichlet boundary with a fixed condition $\partial\Omega_D$ and the face at which the traction force is applied $\partial\Omega_f$ . . . . .	114
5.39	Plots of the total force acting on the cylinder after interpolation for Reynolds numbers (a) $Re = 1 \times 10^5$ (b) $Re = 1 \times 10^6$ . . . . .	115
5.40	Plots of the absolute error of the total force generated by the nearest face mapping interpolation. . . . .	116
5.41	Plots of the total force acting on the cylinder with strake after interpolation for Reynolds numbers (a) $Re = 1 \times 10^5$ (b) $Re = 1 \times 10^6$ . . . . .	117
5.42	Plots of the residual error of the total force generated by the nearest face mapping interpolation for various Reynolds numbers. . . . .	117
5.43	Plots of the displacement for a node at the tip of the straight (—) and helical (—) thermowells at the location (-0.15, 0, 300) for various Reynolds numbers. For each of these plots in the smaller windows had the constant component removed so they only display the oscillating component. . . . .	118
5.44	Plots of the von Mises stress at the base of the straight (—) and helical (—) thermowells at the location (-0.15, 0, 300) for various Reynolds numbers. For each of these plots in the smaller windows had the constant component removed so they only display the oscillating component. . . . .	119

5.45 Plot of the contour plots of the von Mises stress of each element for a straight cylinder for a Reynolds number of  $5 \times 10^5$ . The units are in Pa . . . . . 120

5.46 Plot of the contour plots of von Mises stress of each element for the cylinder with strakes for a Reynolds number of  $5 \times 10^5$ . The units are in Pa. . . . . 120

# List of Tables

2.1	Experimental set ups for the 6” diameter pipe and the 12” diameter pipe by Knight et al. [60]. . . . .	33
2.2	Flow parameters from Okazaki test runs by Lee et al. [61]. . . . .	33
2.3	Comparison summary of experiments in literature by Lee et al. [61] and Knight et al. [54] and customer requirements by looking at an order sheet for thermowells provided by the previous sponsor of this project. The furthest right column displays the experimental rig’s capability running at maximum flow rate.	34
2.4	Dimensions of a proposed thermowell to be tested in the experimental rig. . . . .	36
3.1	Constants used by Menter [67] for $k - \omega$ SST formulation. . . . .	45
3.2	Selected discretisation methods utilised in the fluid simulations conducted in this study. . . . .	56
5.1	Time step at each Reynolds number for the 2D case for flow around a cylinder.	79
5.2	Initial conditions for the 2D case for flow around a cylinder. . . . .	79
5.3	Peak frequencies and Strouhal numbers found for each 2D simulation at varying Reynolds numbers. . . . .	84
5.4	The average mesh sizes for each sub-volume found in the 3D simulations with an infinitely long cylinder. . . . .	87
5.5	Time step at each Reynolds number for the 3D case for flow around a cylinder.	88
5.6	Initial conditions for the 3D case for flow around a cylindrical geometry. . . . .	90
5.7	Peak frequencies, Strouhal numbers and average drag coefficients found for each 3D simulation at varying Reynolds numbers. . . . .	93
5.8	The initial conditions for the 3D simulation of the flow around a cylinder of finite height provided for both cases, with and without strakes. . . . .	101

5.9 Sampling settings of the force field acting on the thermowell surface for both geometrical variants. . . . . 114

# Acknowledgements

I would like to thank the Materials and Manufacturing Academy and COATED CDT (COATED M2A) in Swansea University, and the European Social Fund via the Welsh Government (WEFO) for supporting the work described in this thesis. I want to express my deepest gratitude to my mentors, Prof. Gil and Dr Rolland. Working with them over the years has been an incredible privilege. Their wisdom and guidance have been a source of inspiration and learning for me. I would also like to extend my heartfelt thanks to my family, who have consistently supported me emotionally throughout a challenging time in my academic journey.

To all of you, I am thankful.

# Chapter 1

## Introduction

In this opening chapter, the key themes and motivations that underpin this research are presented. The chapter begins by establishing the broader context and motivation for the study. The crucial role of thermowell design in the context of temperature measurement and control is emphasised. Furthermore, the fundamental principles of thermowell design and their functional importance are covered. Thermowells are integral to temperature measurement in processes where the operation environment can be challenging, thus requiring a balance between equipment integrity and performance. This chapter also outlines the problems and constraints associated with current thermowell designs, setting the stage for the research objectives.

To provide perspective, exploration of the state of the art in thermowell research is carried out. This includes a discussion of both computational fluid dynamics and experimental studies, offering insights into the current state of research and development in this field.

### 1.1 Background and Motivation

A thermowell serves as a protective device between a temperature measurement sensor and the surrounding medium in a flow process. However, the flow-induced mechanical stress on the thermowell can result in vibrational resonance behaviour or fatigue failure [1]. For example, a notable incident occurred in a nuclear power plant in Japan (MONJU) where a failed thermowell caused sodium leak, which led to a fire when the leaked sodium came into contact with oxygen in the air. The root cause of this failure was attributed to weld point failure, likely due to in-line resonance [2]. Following this incident, industry standards were improved



with the introduction of ASME PTC 19.3 [3], which addresses in-line vibration, dynamic stress, and fatigue failure of thermowells. This improvement was necessary as the previous standard failed to account for these factors [4].

Prior to the commencement of this project, there was industrial interest in the study and application of a particular thermowell design feature, and its consequential effects on the flow behaviour surrounding it, as well as the resulting mechanical response of the thermowell itself. Specifically, the design feature in question involves the strategic addition of helical strakes to the outer surface of the thermowell stem.

## 1.2 Understanding Thermowell Design and Function

A thermowell is a protective device used in process industries to shield temperature sensors from harsh process environments while allowing accurate measurement of temperature. The thermowell is a hollow tube closed at one end (well) that is installed into the process piping or vessel and contains a temperature sensor, such as a thermocouple or resistance thermometer, which measures the temperature of the process fluid without the sensor coming into direct contact with the fluid. The thermowell ensures that the temperature sensor is not damaged or degraded by the process fluid, and that it can be easily removed or replaced for maintenance or calibration purposes. The thermowell also provides a barrier against process contamination, preventing the process fluid from entering the sensor and affecting the accuracy of the temperature measurement [5].

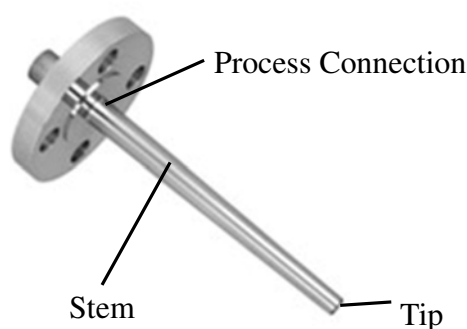


Figure 1.1: Diagram of a thermowell labelled by parts.

The design of a thermowell is critical to its function, as it must be able to withstand the high pressures, temperatures, and corrosive or abrasive conditions of the process fluid without affecting the accuracy of the temperature measurement. As seen in Figure 1.1, the main

components of a thermowell are the stem, the tip, and the process connection. The stem is the long, thin part of the thermowell that extends into the process fluid and houses the temperature sensor. It is typically made of a material that is suitable to the process fluid and has good thermal conductivity, such as stainless steel, Inconel, or Hastelloy. The diameter and length of the stem are determined by the process conditions, such as the pressure, temperature, and flow rate of the fluid. The stem of the thermowell can be tapered, straight, stepped or contain a helical strake. Different types of thermowells can be seen in Figure 1.2. The tip is the part of the thermowell that protects the temperature sensor from the process fluid. It is typically designed to minimise the effects of the process fluid on the sensor and to facilitate accurate temperature measurement. The tip can be tapered, rounded, or flat, depending on the specific process conditions and sensor type. The process connection is the part of the thermowell that connects it to the process piping or vessel. It can be threaded, flanged, or welded, and is typically made of a material that is compatible with the process fluid and has good mechanical strength. The choice of thermowell mounting depends on the specific requirements of the process and the desired level of protection. Some common methods of mounting thermowells are seen in Figure 1.2. The most common methods are threaded, flanged, weld-in and sanitary mounting.

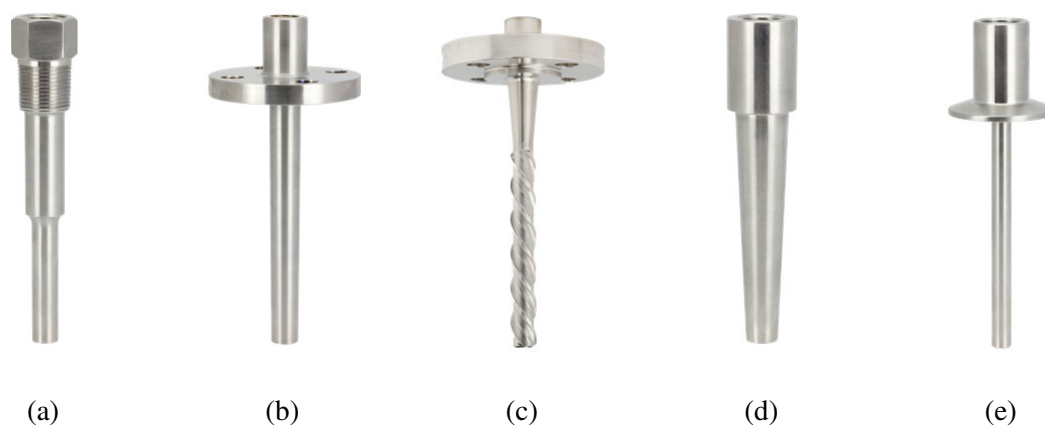


Figure 1.2: Different types of thermowells. (a) Threaded with stepped shank (b) Flanged with straight shank (c) Flanged with helical shank (d) Welded with tapered shank (e) Sanitary insert with straight shank.

Threaded thermowells are installed directly into a threaded opening in a pipe or vessel. They are commonly used in applications where the thermowell can be screwed into the process without welding. Threaded thermowells are easy to install and remove, making them suitable for applications that require occasional sensor replacement. Flanged thermowells

are attached to a pipe or vessel using flanges and gaskets. The flange connection allows for easy installation and removal of the thermowell without welding. Flanged thermowells are often used in applications that require frequent maintenance or where thermowell replacement is necessary. Weld-in thermowells are permanently welded into the process pipe or vessel. They provide a secure and leak-proof connection, making them suitable for high-pressure and high-temperature applications. Weld-in thermowells are not designed for easy removal and replacement. Sanitary thermowells are used in industries such as food, pharmaceuticals, and biotechnology. They are designed for hygienic applications and are often tri-clamp mounted. Sanitary thermowells are easy to clean and maintain.

Due to the thermowells thermal inertia there is a delay between the temperature changes of the fluid and the detection of this change by the sensors when surrounded by a thermowell. The delay is due to two factors, the thermal conduction of the thermowell and the thermal convection of the fluid. The thermal convection may be enhanced by introducing turbulence at the surface of the thermowell therefore increasing mixing of the fluid [6]. The choice of thermowell mounting method depends on factors such as process conditions (e.g., pressure, temperature, fluid type), maintenance requirements, and the need for sensor replacement. Proper installation and selection of the mounting method are crucial to ensure accurate temperature measurements and the safety of the equipment and personnel in industrial processes. It is essential to follow industry standards and guidelines when mounting thermowells [3].

When it comes to thermowell installation, an alternative approach often involves incorporating a stand-off within the pipeline. A stand-off denotes the separation or clearance between the thermowell's outer surface and the adjacent pipe or vessel wall as seen in Figure 1.3. The stand-off distance holds significance during the placement of thermowells in industrial applications, especially when precise temperature measurement or control is necessary within process piping systems or vessels. In the installation of a thermowell via a pipe stand-off, the insertion length is extended because of the elongated stem protruding from the pipe. Consequently, the thermowell may not align with conventional standards. Sometimes, to reduce the unsupported length, collars are affixed to the thermowell, ensuring a tight fit with the pipe stand-off. This adjustment effectively diminishes the unsupported length, thereby enhancing the stability of the thermowell within the flowing stream [7].

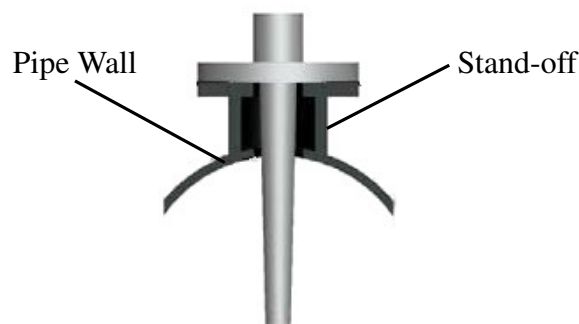


Figure 1.3: Diagram of a thermowell installed with a stand-off mechanism.

The purpose of having a standoff in mounting a thermowell is to isolate the temperature sensor from the potentially harsh or corrosive environment inside the pipe. Another reason is to facilitate sensor replacement. Having a stand-off allows for easier access to the temperature sensor inside the thermowell when maintenance or sensor replacement is necessary. The appropriate stand-off distance can vary depending on the specific application, process conditions, and the design of the thermowell. Factors such as fluid properties, temperature range, and pressure should be considered when determining the stand-off distance.

### 1.3 Traditional Thermowell Design Problems

When fluid flows past a stationary object, such as a thermowell, it causes the formation of low-pressure areas and vortices downstream of the object. Due to the adverse pressure gradient, the flow can experience flow separation, which results in the formation of a separated shear layer [8]. Furthermore, the interaction between the separated shear layer and the free shear layer in the wake of the object can lead to the shedding of vortices [9]. This phenomenon is known as vortex shedding, which occurs in a repeating pattern downstream in what is called a Kármán vortex street [10]. The alternating pattern of these vortices can create oscillating drag and lift forces that act as a driving force for the oscillation of the thermowell. Kármán vortex shedding can occur at a wide range of Reynolds numbers <sup>1</sup>. It is most commonly observed at high Reynolds numbers, where the fluid flow is turbulent and the inertial forces are dominant. Additionally, the flow can transition from a laminar to a turbulent regime in the region close to the boundary of the bluff body, which introduces further complexity to the fluid dynamics [11].

---

<sup>1</sup>Reynolds number is a dimensionless quantity used to determine the turbulent regime of the flow. This is further outlined in Section 3.1.5 (for further details, see equation (2.1))

If the frequency of the vortex shedding coincides with a natural frequency of the thermowell, resonance can occur, and the resulting coupling between the fluid and solid can cause large dynamic <sup>2</sup> stress and potentially lead to failure. Moreover, even smaller vibrational amplitudes of the thermowell can cause fatigue failure over time [12, 13]. In this study, the natural frequency of a structure is referred to as the first modal frequency at which the structure vibrates when subjected to a disturbance. The mode shape describes how the system deforms in response to a particular mode of excitation.

To address this issue, surface features can be developed for thermowells, such as the addition of helical strakes on the surface of the thermowell. These helical strakes promote turbulence at the surface, which then disturbs the generation of periodic vortex streets downstream. Such a design has been proven to minimise the vibration of the thermowell due to vortex shedding and reduce the risk of dynamic stress and failure [14].

Several companies currently manufacture thermowells with this helical design, and it has been shown to be effective in mitigating the effects of vortex shedding. However, it is important to note that the helical design is not currently included in any thermowell standards, hence the motivation behind this work.

## 1.4 State of the Art

The following subsections will contain an in depth review of relevant literature. The aim of this literature review is to attain a greater understanding of the state of the art in this subject matter including Computational Fluid Dynamics (CFD), vortex shedding, and mechanical vibrations. This section will delve into the analysis and design tools used in CFD for cases relating to flow around a cylindrical body similar to a thermowell as well as cases related to the structural response of a structure when placed in a high velocity flow. There will also be an investigation on how solid behaves under cyclic loads (modal analysis, time integration methods). This section will also delve into the coupling of fluid and solid problems.

---

<sup>2</sup>Throughout this work, the term 'dynamic' is used to emphasise that the stress is generated under time varying (not quasi-static) conditions.

### 1.4.1 Computational Fluid Dynamics

Vortex shedding and flow around obstructing objects have been extensively studied in computational simulations. In particular, the operation of thermowells, which can be approximated as a finite height cantilever cylinder placed in a flow, have been investigated [15, 16].

The wake of a bluff body, such as a thermowell, involves the interactions of three distinct shear layers. The first layer is the boundary layer, which is the thin layer of fluid that forms on the surface of the thermowell due to the no-slip condition. The second layer is the separating free shear layer, which is the region of the flow where the boundary layer separates from the surface of the thermowell and transitions to a free shear layer. Finally, the third layer is the wake, which is the region of the flow behind the thermowell where vortices are shed and turbulence is generated [17].

Understanding the complex interactions between these three shear layers is essential for predicting the behaviour of the flow around a thermowell and for designing thermowells that operate effectively and reliably in a given fluid flow. Computational simulations and experimental studies have played a crucial role in advancing our understanding of these phenomena and in developing models and theories to describe them. Williamson et al. [18] discuss the regimes of flow around a cylinder and how they arise between different Reynolds number ranges. At a low Reynolds number it is seen that it is suitable to run simulations with a 2D domain [19–22]. There are numerous studies on the fluid structure interaction that takes place between a solid cylinder placed in flow and the flow itself [19, 23].

Placzek et al. [20] ran numerical simulations of a oscillating cylinder at low Reynolds number. The study investigated incompressible flow around a cylinder by solving 2D Navier-Stokes equations using the Finite Volume method. Simulations were run at a Reynolds number below 100. The relationship between Strouhal number <sup>3</sup> and Reynolds number was compared. This relationship is crucial to understanding the vortex shedding frequency changes in different turbulent regimes.

Sato et al. [19] investigated 2D incompressible flow around a cylinder at low Reynolds number (below 1000) to investigate the flow patterns, flow separation, excitation of fluid

---

<sup>3</sup>Strouhal number is a dimensionless quantity used to define the frequency of vortex shedding. This is further outlined in Section 3.1.5 (For further details, see equation (3.23))

force on the cylinder and Strouhal number. Good agreement was found between all of these parameters with prior experimental results found in [24].

Guilmineau et al. [21] studied vortex shedding from an oscillating cylinder. This study was carried out via numerical 2D unsteady Navier-Stokes solutions. The article studied two phenomena, one was the flow induced by the harmonic in-line oscillation of the cylinder in water at rest, the other was an investigation into transverse oscillation of a cylinder in uniform flow at fixed Reynolds number of 185. The study uses the PISO algorithm for coupling of pressure and velocity. For the fixed cylinder the Strouhal number was found of a range of Reynolds numbers from 50 to 200 with good agreement with previous literature. The simulations involving in line oscillations used a Reynolds number of 100. The resultant vortex shedding is vortices with symmetrical location with respect to the line of motion of the oscillating cylinder. In the second study the vortex shedding was a vortex switching from one side of the cylinder to the other.

Mathupriya et al. [22] studied the flow characteristics around a confined cylinder at low Reynolds number of 200 and 300 . The study ran direct numerical simulations in 2D using the Finite Volume method. The paper observed two modes of shedding frequencies at higher Reynolds number due to confinement effects. The domain was set up with a high blockage ratio of 0.5. The study tested the code of icoFOAM, pimpleFOAM and pisoFOAM. The paper demonstrated that the large blockage ratio promoted a higher Strouhal number of around 0.3433 for icoFoam and pimpleFoam and 0.248 for pisoFoam.

Several works have aimed to study high Reynolds numbers flows in a 2D domain using a wide variety of meshes and turbulence modelling [25–29]. Lehmkuhl et al. [25] studies the unsteady forces on the cylinder at critical Reynolds numbers. This was done via LES of flow with Reynolds number in the range of  $2.5 \times 10^5 - 6.5 \times 10^5$ . The paper finds a drop in drag coefficient at this transition between regimes, this phenomena is also seen in the results by Bearman et al. [30], this reduction is known as the drag crisis. As the Reynolds number increases past this crisis, it was found that the Strouhal number increased to around 0.44 as the shear layers approach each other by increasing pressure gradients and the flow is forced to interact with higher periodicity.

Ye et al. [26] ran studies for to assess the accuracy, stability, and efficiency of the overset grid approach coupled with the RANS model through benchmark computations of flows around a stationary smooth circular cylinder using wall functions. The numerical investigations focus

on two-dimensional simulations across a wide range of Reynolds numbers, ranging from  $6.31 \times 10^4$  to  $7.57 \times 10^5$ , including the critical flow regime. The simulations utilise the RANS solver `pimpleFoam` which uses SIMPLE and PISO iterations in its algorithm. The drag crisis is seen with the drag dropping from 1.2 to 0.6.

Catalano et al. [27] ran a 2D LES with wall modelling study on flow past a cylinder at high Reynolds numbers of  $5 \times 10^5$  and  $10^6$ . The study focuses on assessing the viability and accuracy of large-eddy simulation (LES) with wall modelling for complex turbulent flows at high Reynolds numbers. Specifically, the flow around a circular cylinder in the supercritical regime is investigated. A simplified wall stress model is utilised to provide approximate boundary conditions for the LES. The findings reveal that the LES solutions exhibit higher accuracy compared to the RANS results. They successfully capture important phenomena such as delayed boundary layer separation and reduced drag coefficients observed in experimental measurements after the drag crisis.

Rodríguez et al. [28] studied the flow characteristics and vortex shedding process at different Reynolds numbers (Re) ranging from  $2.5 \times 10^5$  to  $8.5 \times 10^5$  are examined using LES for a circular cylinder. Additionally, there is a sharp decrease in the fluctuating lift as the flow enters the super-critical regime. In the super-critical regime, the Strouhal number remains nearly constant at 0.44. Additionally, there is a sharp decrease in the fluctuating lift as the flow enters the super-critical regime.

However, Thompson et al. [31] discussed the importance of the 3D effects of turbulence, highlighting different modes of instabilities in the wake structure downstream of the cylinder at larger Reynolds numbers. Several simulation studies have been carried out on cylindrical structures similar to that of a thermowell placed into fluid flow [32, 33].

Chan et al. [32] studied the effect of aspect ratio and geometry of a cylinder and cuboid of finite height on flow dynamics. The aspect ratio of the cylinder was varied from 3 to 7 and the Reynolds number based on the cylindrical diameter was kept at 20,000. The flow was solved using the RANS  $k-\omega$  SST turbulence model. The average drag coefficient was found to be around 0.858 for an aspect ratio of 7.

Palau-Salvador et al. [33] presented experimental and numerical findings related to the flow around a circular cylinder mounted on a surface. The study focuses on two different height-to-diameter ratios: 2.5 and 5. For these cases, the Reynolds numbers were 43,000 and 22,000, respectively. The boundary layer of the approaching flow has a thickness



of approximately 10% of the cylinder height. The experimental investigations involve visualisations using dye and measurements of mean velocity and fluctuation components using laser Doppler velocimetry. The numerical analysis employs a large eddy simulation method on a staggered Cartesian grid, utilising the immersed boundary technique. In the case of the longer cylinder, alternating shedding is observed over a significant portion of the height, while for the shorter cylinder, shedding occurs primarily near the ground.

Kornet et al. [34] performed a study of unsteady flow forces on a thermowell of a steam temperature sensor. 3D numerical analysis was presented in this paper using a computational FSI approach. The model used the  $k - \varepsilon$  model. The viscous stress tensor was defined by Navier-Stokes constitutive equation and the  $k - \varepsilon$  model was applied to the Reynolds stress tensor. Once the CFD analysis was complete the aerodynamics loads were applied to the solid thermowell model and the tensile stress of the thermowell was found.

There have also been a few studies on the effectiveness of different bluff bodies or geometrical designs in the reduction of vortex induced vibration. Ranjith et al. [35] investigated the effectiveness of helical strakes in suppressing vortex induced vibration. The paper presents a CFD study on two cylinders fixed at both ends, one being a smooth cylinder and the other having three strakes are provided for the helical design. The author solved incompressible Navier-Stokes equations for a fluid with the properties of water using the Finite Volume method. The algorithm used was the PISO algorithm. The cylinder was rigid and there was no fluid-solid coupling. The flow was studied at two Reynolds numbers (100 and 28,000) based off the cylinders diameter. It was found that straked cylinders gave a larger drag coefficient but vibration amplitude is reduced by 99%. It is found that, as expected, the straked cylinder has a higher drag coefficient in comparison with a smooth bare cylinder. The helical strakes can reduce VIV by about 99%.

Constaantindes and Oakley [36] presented a study of incompressible flow around a bare cylinder and a cylinder with helical strakes to study the effects of the helical strakes on vortex shedding. The software used was Acusolve which uses the finite element method to solve flow. Incompressible Navier Stokes equations were solved including buoyancy. Two turbulence models were also compared, a RANS turbulence model called Spalart Allmaras and DES. The studies found that the RANS turbulence model predicted higher drag coefficients than DES and did not capture the physics as well. It was found that the addition of helical strakes eliminated

vortex shedding and therefore flow induced vibration. It was found that the cylinder with strakes displayed a drag coefficient of around 1.6 for all reduced velocities and Reynolds numbers.

Designs with varying surface features other than helical strakes have also been studied. Baek et al [37] studied incompressible 2D and 3D flow using spectral hp elements at Reynolds numbers of 500 and 1200 with a cylinder with a parallel slit. Lift and drag were computed in time and with varying slit width. The simulations were ran on a software called NEKTAR which uses spectral hp elements in order to solve the fluid problem [38]. The flow through the parallel slit disturbs the eddy currents immediately downstream of the cylinder where the recirculation region is present. The effects of the slits were investigated for both fixed cylinders and free cylinders. The study claims that a parallel slit successfully suppresses lift and vortex induced vibration with a more than 70% reduction of displacement in the lift direction. The optimal width of the slit, however, changes with Reynolds number.

Pinto et al. [39] studied the suppression effects of discontinuous helicoidal fins around a cylinder. This was studied via numerical simulation using the software xnavis [40]. The method involved using the Finite Volume method to solve a 3D incompressible flow at Reynolds number of around  $1.6 \times 10^5$  so the flow around the cylinder would be classed as sub-critical. In order to solve for turbulence the Spalart Allmaras turbulence model was used. The study found the discontinuous helicoidal fins to reduce the peak frequency of the lift coefficient when compared to a bare cylinder although the paper states that a more sophisticated turbulence model is needed. Three dominating frequencies were found the Fast Fourier transform of the lift coefficient all at low frequencies when compared to the bare cylinder.

A journal by Dai et al. [15] predicted the vortex shedding suppression effects of a base splitter plate on circular cylinders. The study considers a 3D fully-turbulent, incompressible flow at high Reynolds number. The study was carried out via OpenFOAM software [41] so the Finite Volume method was used. The study was carried out at a Reynolds number of  $1.8 \times 10^5$  and to solve for turbulence the  $k - \epsilon$  model was used with one of the coefficients modified by the author as they state that the standard  $k - \epsilon$  model fails to sufficiently capture the occurrence and strength of vortex shedding for a cylinder. It was found that there was around a 90% reduction in the fluctuation of drag coefficient and a 80% reduction in the fluctuation in lift coefficient and a 30% reduction in "steady state" drag depending on the ratio between the cylinder height and the base splitter plate length.

Carmo et al. [42] studied the effect of a circular cylinder subjected to wake interference. This was achieved by setting up the simulation with two identical cylinders in tandem with a small distance between them. The incompressible Navier Stokes equations with no turbulence model were solved. The Reynolds number, defined by the cylinder diameter, was varied from 90 to 645 by varying the incoming velocity. The amplitude of vibration was found to be larger amplitudes of vibration when compared to vortex induced vibration solely. This study also notes that 3D simulations gave smaller amplitudes of vibration than the same cases in 2D. The Strouhal numbers for all of the Reynolds number range was constant at a value of around 0.19.

In summary of the computational studies, the current literature discusses various aspects related to vortex shedding and the flow around obstructing objects. It highlights the importance of understanding the interactions among the three distinct shear layers in the wake of a bluff body like a thermowell: the boundary layer, the separating free shear layer, and the wake itself. These interactions are crucial for predicting flow behaviour and designing effective thermowells. Computational simulations and experimental studies have significantly contributed to advancing the understanding of these phenomena and developing models and theories to describe them.

The literature also mentions the significance of Reynolds numbers in determining the appropriate simulation approach. At low Reynolds numbers, 2D simulations are often suitable, while higher Reynolds numbers require 3D simulations. The Strouhal number is discussed as a valuable parameter to benchmark and analyse in these simulations, providing insights into flow patterns and characteristics. The studies also highlight in the changes of regime comes various changes in the parameters, in particular the drag crisis at high Reynolds number. Furthermore, several studies that have explored flows around cylindrical structures similar to thermowells. These studies have investigated various aspects, including drag coefficients, vortex shedding, and the effects of different geometrical designs on flow dynamics. Some studies focused on suppressing vortex-induced vibration (VIV) by altering cylinder shapes or adding features like helical strakes or parallel slits. These investigations contributed to a deeper understanding of fluid-structure interactions and provided valuable insights for design improvements. From this study of literature it is evident that many approaches can be made in terms of the turbulence model but a RANS turbulence model appears to be accurate and computationally cost effective over other methods such as LES, although LES is said to have higher accuracy. PISO and SIMPLE algorithms both are used in literature and it is not evident that there is any favoured

method. The Finite Volume method is favoured and will be used in this work due abundance of examples of its use in literature, the fact that the method conserves mass and energy, its can be adapted to complex geometries easily and the abundance of well-developed commercial code i.e OpenFOAM and Fluent.

## 1.4.2 Fluid Structure Interaction

Fluid-Structure Interaction (FSI) can be exploited when examining the behaviour of a cantilever-like structure immersed in a fluid flow. This phenomenon occurs as the fluid's dynamic forces exert stress on the cantilever, causing it to undergo deformation. Simultaneously, the cantilever's deformation influences the surrounding fluid flow. FSI represents the bidirectional relationship between the solid structure and the fluid environment. Numerous studies have been carried out studying this phenomena.

Zakaria et al. [43] studied the flow around a cylinder with a splitter plate on OpenFOAM for low Reynolds number between 20 and 200. Although not benchmarked the article studies an fluid structure interaction approach of large deformations and added mass using the Arbitrary Lagrangian–Eulerian (ALE) Finite Volume method and mesh motion. The fluid uses the PISO algorithm and second order time and spatial discretisation schemes. This problem is also studied by Stefanini et al. [44], the paper outlines the development of a code using OpenFOAM. The paper outlines a FSI approach using modal superposition for the solution of the solid problem and the Finite Volume method to solve the fluid problem. The study looks at weak and strong coupling approaches.

Zhang et al. [45] proposes a FSI problem of a hollow cylinder with a built in piezo-beam. The study consisted of a wind tunnel experiment for benchmarking the computational work. A parameter identification method is used to determine the lift and drag coefficient and frequency and good agreement was found with experimental tests. A coupled fluid-structure electrical model was used via the lattice Boltzmann method. A local eddy viscosity model with a large eddy turbulence model was used for Reynolds numbers from 8400 to 42000.

Lorentzon et al. [46] studied the vortex induced vibration of a solid cuboid cantilever. The integration of open-source software packages, DEAL.II and OpenFOAM, has been employed to establish a linkage between a finite element structural formulation and a Finite Volume fluid formulation, applicable to gases or liquids. A C++ implementation of a staggered solution algorithm for FSI was achieved, incorporating the Aitkens relaxation method and a

Reduced-Order Model. The boundary was therefore strongly coupled with the transfer of displacements from the solid being transferred back into the fluid. The PISO algorithm was also found in this study. The algorithm was used to compute vortex-induced vibrations as a function of flow velocity, yielding successful comparisons with data found for strouhal number as a function of Reynolds number.

Modal Superposition is a computationally inexpensive method for solving structural problems and is often used in reduced order modelling. Ferhatoglu et al. [47] applied advanced reduced-order modelling techniques were to Micro-Electro-Mechanical Systems. The mode superposition technique, coupled with finite element solvers, was used to accurately represent the dynamic behavior of flexible MEMS components and their interactions with thermal, electrostatic, and fluid fields. The results yielded macromodels described by analytical terms, which can be seamlessly integrated into electronic and system simulators for virtual prototyping and device analysis. The conclusion highlights the effectiveness of these advanced macromodeling approaches based on mode superposition, emphasizing their reliability for MEMS design at the system level.

These studies share a common focus on fluid-structure interaction (FSI) phenomena, where fluid flow interacts with and influences the deformation of structures, and vice versa. OpenFOAM is used as a computational tool in multiple studies, highlighting its versatility for FSI simulations. Furthermore, various numerical techniques, such as modal superposition and reduced-order models, are employed to tackle the complexities of FSI. Although these studies focus on weak to strongly coupled FSI problems, in this case we do not wish to investigate any frequency lock-in regions due to coupling and only wish to investigate when the thermowell begins to display large displacements and therefore begins to fatigue the base of the thermowell.

Wijesooriya et al. [48] presents a cost-effective numerical approach to analyze the structural response of a super-tall building under turbulent wind conditions, as an alternative to expensive experimental tests. The innovative one-way Fluid-Structure Interaction (FSI) simulation technique, which took only 74 hours for 18 structural configurations, was compared to a time-consuming two-way FSI method, which required 4800 hours for only six configurations using commercial software. The one-way FSI method provided accurate results and exhibited good correlations with experimental observations, including vortex-induced resonance, making it a viable and efficient approach for estimating structural responses at a reasonable cost. This

study can serve as a justification for producing a one-way FSI workflow due to the reasonable accuracy and low computational cost.

### 1.4.3 Experimental Studies

There have been a number of experiments carried out measuring the vibration of thermowells and experiments measuring vibration of cylinders [49] and other bluff bodies [50,51].

Okajima et al. [51] investigated the flow induced in-line oscillation of circular cylinders. Two cases were studied, one case was a spring mounted 2D rigid cylinder and the other was a cantilevered cylinder in free-oscillation test. The experiments were carried out in a water tunnel. The study concluded that, for the spring mounted cylinder, there were two types of excitation phenomena and the response amplitude were very sensitive top the reduced mass-damping parameter in the first excitation region with symmetric vortices while alternate vortex streets shed periodically and locked-in with the oscillation of the cylinder. The cantilevered cylinder displayed two lock-in regions even at large aspect ratio.

Sui et al. [52] performed an experimental study of the effect of helical strakes on a flexibly mounted cylinder in suppressing vortex induced vibration with a large mass damping parameter. The Reynolds number of the flow was varying from  $2.7 \times 10^3$  to  $5.8 \times 10^4$ . The study used smoke, lasers, sensors and high speed imaging to obtain images of the flow patterns seen in the flow regime of study. From the flow visualisation of both the flow around the bare cylinder and the cylinder with helical strakes it was observed that the helical strake changes the separation points on the cylinder and avoids the interaction of the two shear layers as well as reduce the vortex shedding of the wake structure. The helical strake efficiency in reducing the root mean square of amplitude of lift and drag was plotted at a reduced velocity ranging between 8 and 32 for different cylinder heights and strakes. The most effective test was the cylinder with pitch to diameter ratio of 5 and fin height to diameter ratio of 0.14 with the square helical strake fins.

Zhou et al. [53] also studied vortex induced vibration on a cylinder with helical strakes. The study presented a three-strand helical strake with a pitch of 10 cylinder diameters and a strake height of 0.12 cylinder diameters. The helical strake cylinder was placed into a wind tunnel and used an X-probe at 4 different Reynolds numbers. It was found in the wind tunnel that vortex induced vibrations were reduced by 98% in terms of amplitude. The paper states that to

suppress vortex induced vibration, one can either change the natural frequency of the structure or to inhibit or disrupt vortices and their structural formation.

Knight et al. [54] studied thermowell vibration of thermowells meeting ASME industry standards against their equivalent thermowells utilising helical strakes as a means to suppress vibration caused by the process fluid. This study was performed by Orbital Gas, there was a total of 4 different thermowells that underwent vibration testing. Natural gas was used in as the test fluid in a 6" pipe and a 12" pipe where ASME thermowells and thermowells with helical strakes were installed. Tests were carried out in the Reynolds number range of  $2.52 \times 10^5$  to  $2.59 \times 10^6$  based on thermowell diameter. The study found that the straight ASME thermowells vibrated at an amplitude of two orders of magnitude higher than the helical strake counterparts. The same was result was found for measurements done by accelerometer and strain gauges. A transient temperature study was performed along with the vibration test which found that there is negligible difference in lag in temperature measurements between ASME thermowells and thermowells with helical strakes. The study concluded that for the 12" runs the oscillations of the straight thermowell were one to two orders of magnitude larger than those of the helical strake thermowell. For the 6" runs the helical strake thermowell experienced accelerations and calculated deflections approximately one-third to one-half of the values of a straight thermowell.

Lee et al. [55] also ran a test on helical thermowells against straight ASME thermowells for a design by Okazaki. Oil was used as the test fluid and two centrifugal pumps were placed in parallel. The test rig was set up so that the ASME standard thermowell was installed downstream of the thermowell with helical strakes. 5 test runs were carried out varying volumetric flow rate. The minimum Reynolds number in one of these runs is  $2.63 \times 10^4$  and the maximum Reynolds number in one of these runs is  $1.33 \times 10^5$ . The thermowells were fitted with strain gauges and it was found that the maximum dynamic load of the standard thermowell compared to the helical thermowell was 10 times more.

In summary of the experimental studies, these experiments collectively contribute to our understanding of thermowell and cylinder vibrations and provide valuable insights into the effectiveness of helical strakes in suppressing vortex-induced vibration across various flow conditions and applications. These studies agree that breaking up the formation of vortices via a passive method such as a geometry change, all significantly suppress the shedding.

## 1.5 Thesis Overview

This section will provide insight into the objectives of this work and an outline of how the following documentation is structured. This study aims to emphasise variations in fluid dynamics and subsequent structural responses when a structure is exposed to high-velocity fluid flow, comparing scenarios with surface flow disruption to those without.

### 1.5.1 Objectives

The primary goals of this thesis can be categorised into three main objectives. Firstly, the thesis aims to assess and compare the existing methodologies accepted in industry with numerical methods. By undertaking this evaluation, the research seeks to identify any limitations or deficiencies in current industry standards. Additionally, the objective is to enhance the prediction capabilities of thermowell failure through the utilisation of numerical approaches.

The second objective of the thesis is to propose and assess a computationally efficient, cost-effective tool for predicting the structural response of a thermowell when subjected to fluid flow, utilising one-way fluid-structure interaction. This predictive tool will involve the analysis of factors, including force mapping, modal frequency response analysis, and fluid flow analysis. By combining these aspects, the research intends to create a tool that can accurately forecast whether a modal response is at risk of being excited under the conditions of use of the thermowell. The emphasis here is on achieving a solution that is both computationally efficient and reliable, enabling practical applications in real-world engineering contexts. In developing the tool, an additional objective is to better understand the fluid flow around a cantilever-like structure.

The final objective is to propose an experimental apparatus based on existing industrial equipment which is cost effective using existing equipment and allowing the exploration of design outside the current designs. This can also be used to validate the prediction method developed in the second objective. To achieve this, the thesis involves designing a flow rig capable of replicating the most extreme flow conditions typically encountered in industrial settings. The proposal of an experimental setup lays the foundation for future benchmarking work of the tool developed by numerical simulation.



## 1.5.2 Thesis Outline

This thesis comprises six chapters, each with a distinct focus and contribution to the field of fluid-structure interaction. Each contribution will become important to building a reduced order, efficient tool in predicting the response of a thermowell placed in fluid flow. The document will begin to explain the industry standards and the shortcomings of the assumptions made in the calculation for structural response.

**Chapter 2** provides an overview of the current industry standards in sizing and manufacturing thermowells safely. The industry standards will include the calculations needed to check the modal frequency of the thermowell compared to the likely mode of vortex shedding, the stress and pressure checks. The chapter will also cover the assumptions made by the standard. The chapter will finally propose a experimental validation study.

**Chapter 3** provides a fundamental background on fluid mechanics, which is essential for the understanding and implementation of computational fluid dynamics (CFD) simulations. The chapter begins by introducing the basic conservation laws of fluid mechanics, including conservation of mass, momentum, and energy. The chapter then discusses boundary conditions, which are crucial for defining the fluid flow problem and solving the governing equations. Relevant parameters, such as Reynolds number, Strouhal number, lift and drag coefficients, are also discussed, and their relevance to fluid flow is highlighted. Furthermore, the chapter covers the physics of turbulence, which is an intrinsic part of many fluid flow problems. Finally, the chapter provides an overview of CFD, including the numerical methods used to discretise and solve the governing equations, as well as the software packages commonly used for CFD simulations.

**Chapter 4** focuses on the theory of solid mechanics, describing the conservation laws in strong and weak form, and introducing the finite element method for frequency modal analysis. In this chapter, a mathematical description of solid mechanics, including continuum mechanics, modal frequency analysis, software, finite element analysis, and fluid to solid mapping will be provided. This chapter will begin by introducing the basic concepts of continuum mechanics, including stress, strain, and the equations of motion. The chapter will then discuss modal frequency analysis, which is a technique used to determine the natural frequencies and mode shapes of structures. Next, an overview of software commonly used in solid mechanics, including commercial and open-source software will be presented. This chapter will, then, focus on finite element analysis, which is a numerical technique used to solve problems in

solid mechanics. Finally, the chapter will also discuss fluid to solid mapping, which is the process of transferring data from a fluid simulation to a solid simulation.

**Chapter 5** will begin by presenting the results from the fluid simulations covering a large range of Reynolds numbers and transition from 2D to 3D flow. Each example will begin with a visual description with provided figures for a better understanding of the flow behaviour. Additionally, the frequency modal solid solver has been benchmarked against a time-integration method. Having verified the accuracy of all aspects of the model, the full process of fluid-to-solid mapping will be analysed for both straight and helical geometries.

**Chapter 6** provides a summary of the research findings and conclusions drawn from the thesis. This chapter also discusses potential avenues for future research that can build upon the work presented in this document.

# Chapter 2

## Industrial Application

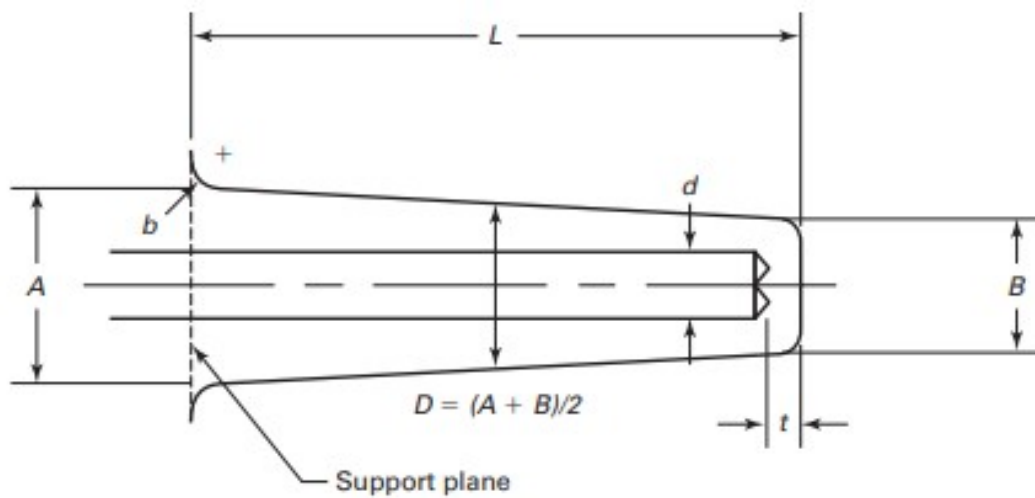
This chapter presents the current industry standards for predicting the structural response of a thermowell placed in a flow process. The pass/fail criteria for safety of the product will be detailed from modal frequency checks to assessing dynamic and steady state stress. The fundamental assumptions of the standards are outlined in order to identify the current shortcomings.

Additionally, we present a proposal for an experimental validation study, underlining our commitment to bridging the gap between theory and practical application. This proposed study provides a tangible opportunity to test theoretical knowledge and validate its suitability in industrial contexts.

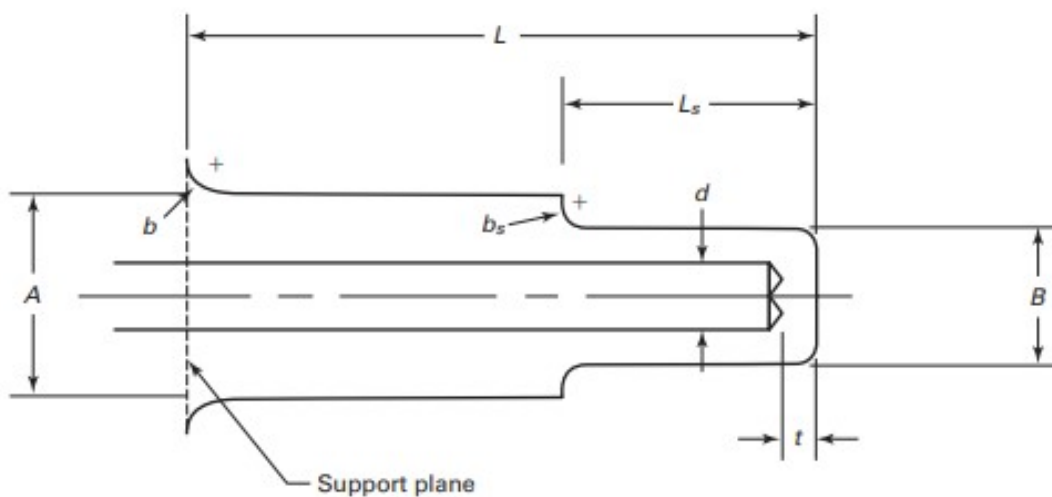
### 2.1 Industry Standards

In order to gain a thorough understanding of the methods used to size thermowells for manufacture, a decision was made to undertake a detailed calculation following the ASME PTC 19.3 TW-2016 industry standards. All equations listed in this section will be from this industry standard [3]. These standards specify four key requirements for thermowells: the first resonant frequency of the thermowell must be high enough to prevent excitation from fluid flow, the maximum dynamic stress should not exceed the allowable fatigue stress limit, the maximum steady state stress on the thermowell must not exceed the von Mises criteria, and the external pressure on the thermowell tip, shank, and flange must not exceed their respective pressure ratings. Additionally, these standards provide several dimensional constraints for thermowells. The labels for each part of the thermowells used for calculating several metrics

used for thermowell checks are displayed in Figure 2.1. These labelled will be used in the following sections.



(a) Dimensions of a straight thermowell.



(b) Dimensions of a step-shank thermowell.

Figure 2.1: A schematic diagram of both types of thermowell stems and the labels corresponding to each part of the thermowells. These diagrams are found in [3].

The current industry standards for thermowell sizing take into account various factors, such as thermowell dimensions, material, flow conditions, method of mounting, and sensor properties. The complete calculation procedure differs depending on the type of thermowell being used. Straight and tapered thermowells are calculated using a different method than stepped thermowells.

To determine the frequency of the thermowell, all thermowells are first treated as an idealised beam with the mean dimensions of the thermowell. A series of correction factors are then applied to account for deviations from a solid beam of uniform cross-section, added

mass of the fluid and sensor, and mounting compliance. The frequency of the thermowell must deviate sufficiently from the vortex shedding frequency to pass the check.

For the dynamic stress calculation, the stress levels at the base of the thermowell are determined to be the points of maximum stress for straight and tapered thermowells and for the base of the reduced diameter in stepped thermowells. The dynamic stress is based on the stresses arising from oscillation of the thermowell taking in consideration the lift and drag stresses. If the peak oscillatory bending stress amplitude exceeds the fatigue endurance limit, the thermowell will not pass the check. The fatigue endurance limit is determined by the material selected for the thermowell.

To calculate the steady state stress, the combined effects of hydrostatic pressure and the non-oscillating drag force produce the point of maximum stress at the base of the thermowell. This stress is then used to calculate the von Mises stress by applying radial stress, tangential stress, and the difference between them. The von Mises criteria for failure compares the maximum allowable stress for the thermowell to the von Mises stress. The maximum allowable stress is determined according to the standards for most materials commonly used in thermowell manufacturing.

For the pressure check, the design pressure rating for the thermowell tip and shank are calculated using thermowell dimensions and the maximum working stress for the material. The minimum value for design pressure for a part of the thermowell is the pressure rating for the whole structure. If the hydrostatic operating pressure exceeds the pressure rating of the thermowell, the pressure check fails.

Overall, the ASME calculation procedure requires input of the process fluid, pressure, temperature, fluid velocity, application, and weldability in order to determine the appropriate sizing of a thermowell for manufacturing purposes.

### **2.1.1 Frequency Check**

The frequency check tests whether the natural frequency (i.e first natural frequency) of the thermowell will coincide with its vortex shedding frequency under the working conditions, which would excite the thermowell into resonance and lead to damage. First the vortex shedding frequency is calculated then the first natural frequency of the thermowell is estimated. The frequency of vortex shedding and the natural frequency of the thermowell have to be calculated to ensure that the thermowell does not enter mechanical resonance.

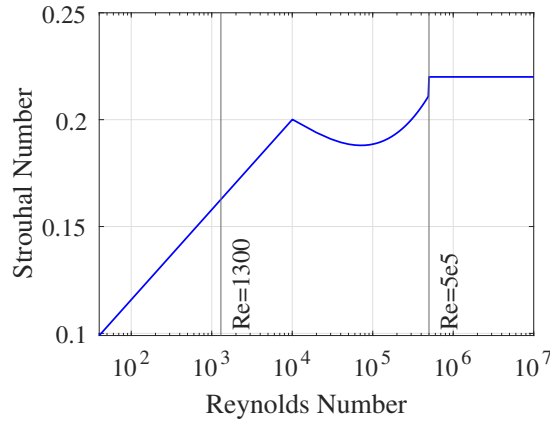


Figure 2.2: Plot of the Strouhal number vs Reynolds number defined by (2.2) in [3].

### Vortex shedding Frequency

In the calculation, firstly, the frequency of vortex shedding is found using available data from [56] which was a study of flow around a cylinder to outline the trend between the Strouhal number and the Reynolds number. The Reynolds number is defined as

$$Re = \frac{VB}{\nu}, \quad (2.1)$$

where  $\nu$  is kinematic viscosity,  $V$  is the process fluid velocity and  $B$  is the tip diameter of the thermowell. The Strouhal number,  $N_s$ , is calculated differently for different Reynolds number regimes in equation as follows,

$$N_s = \begin{cases} 0.22(1 - 22/Re) & 22 \leq Re < 1300 \\ 0.213 - 0.0248[\log_{10}(Re/1300)]^2 + 0.0095[\log_{10}(1300)]^3 & 1300 \leq Re < 5 \times 10^5 \\ 0.22 & 5 \times 10^5 \leq Re < 5 \times 10^7 \end{cases} \quad (2.2)$$

The Strouhal number is a non-dimensionalised frequency of vortex shedding found in (2.2). A plot of this function for Strouhal number can be seen in Figure 2.2 and it is a idealised trend line approximating what is seen in literature [57, 58]. To find the actual frequency of vortex shedding the following must be used,

$$f_s = N_s \frac{V}{B}. \quad (2.3)$$

### Natural Frequency of the Thermowell

As per industry standards [3], the natural frequency of the thermowell is approximated to be equal to the natural frequency of a idealised beam seen in equation,

$$f_a = \frac{1.875^2}{2\pi} \left( \frac{EI}{m} \right)^{1/2} \frac{1}{L^2}, \quad (2.4)$$

where  $E$  is the elastic modulus at the operating temperature,  $I$  is the second moment of inertia defined by  $I = \pi(D_a^4 - d^4)/64$ , where  $D_a$  is the average thermowell diameter,  $d$  is the bore diameter,  $L$  is the length of the thermowell and  $m$  is the mass per unit length of the thermowell defined by  $m = \rho_m \pi(D_a^2 - d^2)$  is the mass per unit length of the thermowell. The boundary conditions in this idealised beam case is that of a cantilever with a fixed end and all other boundaries considered free. At this point of the calculation the thermowell is assumed to be solid and straight. The natural frequency is then corrected to take into account the deviations from a beam of uniform cross section. The correction factor is

$$H_f = \frac{0.99[1 + (1 - B/A) + (1 - B/A)^2]}{1 + 1.1(D_a/L)^3[1 - 0.8(d/D_a)]}, \quad (2.5)$$

where  $A$  is the diameter at the base of the thermowell. The frequency is again corrected for the added mass of the fluid and the added sensor mass of the sensor inside the thermowell. The correct factor for added mass of the fluid is as follows

$$H_{a,f} = 1 - \frac{\rho}{2\rho_m}, \quad (2.6)$$

where  $\rho_m$  is the density of the thermowell and  $\rho$  is fluid density. The correction factor for the added mass of the sensor inside of the thermowell is as follows

$$H_{a,s} = 1 - \frac{\rho_s}{2\rho_m} \left[ \frac{1}{(D_a/d)^2 - 1} \right], \quad (2.7)$$

where  $\rho_s$  is the density of the sensor. The natural frequency of the thermowell is then defined as

$$f_n = H_f H_{a,f} H_{a,s} f_a. \quad (2.8)$$

There is a last addition correction factor to take into account the mounting compliance of the thermowell and defined as

$$H_c = \frac{1}{(K_M/E)} \frac{\pi(A^4 + d^4)}{32L[1 + 1.5(b/A)]^2}, \quad (2.9)$$

where  $b$  is the fillet radius and  $K_M$  rotational stiffness of the thermowell support defined by

$$K_M = \frac{E}{1.95e^{11}} \frac{A^3}{8}. \quad (2.10)$$

The natural frequency (first harmonic mode) of the thermowell with selected mounting is therefor calculated via the following equation:

$$f_n^c = H_c f_n. \quad (2.11)$$

The vortex shedding and the natural frequency of the thermowell mounted are then compared. The thermowell is found compliant with the standard if the following condition is met:  $f_s < 0.4 f_n^c$ .

### Frequency Limit for Low-Density Gases

For fluid of sufficiently low density with lower Reynolds number, the intrinsic damping of the thermowell suppresses the in-line vibrations sufficiently. The frequency criteria is also met if in-line resonance is suppressed by having a Scruton number,  $N_{Sc}$ , of over 2.5 and a Reynolds number of under  $10^5$  (as well as  $f_s < 0.8 f_n^c$ ). Scruton number is defined by.

$$N_{Sc} = \pi^2 \zeta (\rho_m / \rho) [1 - (d/B)^2], \quad (2.12)$$

where  $\zeta$  is the damping factor. The amplitude of vortex induced vibration is said to decrease with larger Scruton numbers [59].

### Frequency Limit for General Cases

According to the standards [3], in-line resonance stress checks must be made if  $0.8 f_n^c > f_s > 0.4 f_n^c$  and in-line resonance is not suppressed. Firstly the fluid velocity for the in-line



resonance is calculated in equation (2.13).

$$V_{IR} = \begin{cases} \frac{Bf_n^c}{2N_s} \left( 1 - \frac{22\mu}{B\rho V} \right) + \frac{22\mu}{B\rho} & \text{for } 22 \leq Re < 1300 \\ \frac{Bf_n^c}{2N_s} \left[ 1 - \frac{a(R)}{N_s} \log_{10} \left( \frac{Bf_n^c}{2N_s V} \right) \right] & \text{for } 1300 \leq Re < 5 \times 10^5 \\ \frac{Bf_n^c}{2N_s} & \text{for } 5 \times 10^5 \leq Re < 5 \times 10^7 \end{cases} \quad (2.13)$$

where  $\mu$  is the fluid viscosity. The in-line stress is then calculated by firstly finding the G factor depending on how the thermowell is shielded from the flow. The G factor is a parameter appropriate for evaluating stress, which is formulated differently according to whether shielding is used or not (via a stand-off). The factor is related to where the maximum stress is seen in relation to the length of the thermowell and different calculations are used for different stems and whether or not the flow is shielded. If there is no shielding, the following equation is used.

$$G_{SP} = \frac{16L^2}{3\pi A^2 [1 - (d/A)^4]} [1 + 2(B/A)]. \quad (2.14)$$

If the thermowell shielded from the flow then the following equation is used:

$$G_{SP} = \frac{16L^2}{3\pi A^2 [1 - (d/A)^4]} \{ 3[1 - (L_0/L)^2] + 2(B/A - 1)[1 - (L_0/L)^3] \}, \quad (2.15)$$

where  $L_0$  is the length shielded from the flow. When evaluating in-line stress, a magnification factor is defined. This is the ratio of deflection and stress at a given frequency to the deflection and stress at zero frequency. The standard describes a lock-in band for shedding frequencies sufficiently close to the natural frequency of the thermowell. It states a magnification factor must be taken into account for frequencies low enough to appreciably excite the natural frequency. It is defined as

$$F'_M = \frac{1}{1 - (r')^2}, \quad (2.16)$$

where  $r' = \frac{2f_s}{f_n^c}$ . With G parameter, in line fluid velocity and a magnification factor, the oscillating drag stress can be calculated as follows,

$$S_d = 0.5\rho G_{SP} F'_M C_d V_{IR}^2, \quad (2.17)$$

where constant  $C_d = 0.1$ . Before moving forward it is important to not subscript  $D$  represents conventional steady-drag forces, subscript  $d$  represents oscillating-drag forces and subscript  $l$  represents oscillating lift forces.

The combined lift and drag coefficient can then be calculated by only accounting for the drag force lift (zero lift force in in-line resonance) and multiplying by a stress concentration factor defined as

$$K_t = \begin{cases} 1.1 + 0.033(A/b) & \text{for } A/b < 33 \\ 2.2 & \text{for } A/b \geq 33 \\ 2.3 & \text{If threaded mounting} \end{cases}, \quad (2.18)$$

This concentration factor assumes stress is concentrated at the base of the thermowell. The combined concentrated lift and drag stress is calculated by the following

$$S_{0,max} = K_t (S_d^2 + S_l^2)^{1/2}. \quad (2.19)$$

The in-line stress resonance stress is checked and is passed if the following condition is met:  $S_f F_T F_E > S_{0,max}$ , where  $S_f$  is the fatigue stress limit (defined by material type in the standard),  $F_T = E/195$  GPa is the temperature de-rating factor and  $F_E = 1$  is the environmental factor.

## 2.1.2 Dynamic Stress Check

Dynamic stress checks are the stresses seen at the base of the thermowell when the thermowell is oscillating. In the industry standards [3], firstly, magnification factors must be calculated via equation (2.20) and equation (2.16).

$$F_M = \frac{1}{1 - r^2}, \quad (2.20)$$

where  $r = \frac{f_s}{f_n^c}$ .

Then as the stress calculation for in-line resonance the drag stress must be calculated using fluid velocity instead of in-line resonance fluid velocity. In this case lift stress is non-zero so this must be calculated too. The lift and drag oscillating stresses,  $S_l$  and  $S_d$ , were calculated as

follows

$$S_l = 0.5\rho G_{SP}F_M C_l V^2 \quad (2.21a)$$

$$S_d = 0.5\rho G_{SP}F_M C_d V^2, \quad (2.21b)$$

where  $C_l = 1$  and  $C_d = 0.1$ . The  $C_l$  and  $C_d$  are the oscillatory component of the lift and drag coefficient and are estimated from literature [26], however, no source is cited.

The combined lift and drag coefficient is now calculated by adding lift and drag forces in quadrature and multiplying by a stress concentration factor in equation (2.22).

$$S_{0,max} = K_t (S_d^2 + S_l^2)^{1/2}. \quad (2.22)$$

The dynamic stress is checked and is passed if the following condition is met:  $S_f F_T F_E > S_{0,max}$ .

### 2.1.3 Steady Stress Check

Steady state stress refers to the stress that the thermowell undergoes at its base assuming there are no oscillatory components of the fluid forces. The von Mises stress is calculated and compared to the maximum allowable working stress assigned by the material type of the thermowell. According to standards [3], the von Mises stress is calculated using radial pressure stress (calculated in equation (2.23a)), tangential pressure stress (calculated in equation (2.23b)), axial pressure stress (calculated in equation (2.23c)) and steady-state drag stress (calculated in equation (2.23d)).

$$S_r = P \quad (2.23a)$$

$$S_t = P \frac{1 + (d/A)^2}{1 - (d/A)^2} \quad (2.23b)$$

$$S_a = \frac{P}{1 - (d/A)^2} \quad (2.23c)$$

$$S_D = 0.5\rho G_{SP}F_M C_D V^2 \quad (2.23d)$$

$$S_{max} = S_D + S_a \quad (2.23e)$$

where  $C_D = 1.4$  and represents the constant (steady state) component of the drag coefficient. Von Mises stresses is then calculated in equation (2.24).

$$\sigma_{vm} = \sqrt{\frac{(S_{max} - S_r)^2 + (S_{max} - S_t)^2 + (S_t - S_r)^2}{2}}. \quad (2.24)$$

Then the steady state pressure check is passed if the von Mises stress meets the following condition:  $\sigma_{vm} \leq 1.5S$ , where  $S$  is the maximum allowable working stress.

### 2.1.4 Pressure Stress Check

The pressure check, as seen in [3], tests whether all parts of the thermowell can withstand the hydrostatic pressure of the application. The design pressure at the stem and the tip are defined the in equations (2.25a) and (2.25b) respectively.

$$P_c = 0.66S \left[ \frac{2.167}{2B/(B-d)} - 0.083 \right] \quad (2.25a)$$

$$P_t = \frac{S}{0.13} \left( \frac{t}{d} \right)^2, \quad (2.25b)$$

The minimum value for design pressure of a part of the thermowell is checked via the following condition:  $\min(P_c, P_t) > P$ . This states that the minimum design pressure between the thermowell tip and shank exceeds the operating pressure.

### 2.1.5 Assumptions in the Industry Standards

The current industry standards make certain assumptions that may introduce errors in the calculation of thermowell behaviour, particularly in comparison to real-world applications.

#### Infinitely Long Thermowell

The standard assumes that the frequency of vortex shedding and the associated Strouhal number follow the characteristics observed in infinitely long cylinders. It assumes that the flow over the tip of the cantilever-like structure does not affect the frequency of vortex shedding. While this assumption may hold true for infinitely cylinders, it becomes a potential source of error when applied to finite thermowells. In reality, the flow over tip of the thermowell

can have an impact on the frequency of oscillation, leading to deviations from the standard's assumptions.

### **Natural Frequency of the Structure**

The standard assumes that the natural frequency of the thermowell is equal to the analytical solution for an idealised beam, with correction factors. The standard incorporates correction factors for various factors such as shielding of the thermowell, cross-section variation, added mass, and sensor mass. These correction factors are typically determined through experimental means. However, a more accurate determination of the thermowell's natural frequency can be obtained using finite element analysis or other advanced numerical methods.

### **Change in Turbulent Regime**

The stress checks outlined in the standard utilise fixed lift and drag coefficients of 1 and 0.1, respectively. However, these fixed coefficients do not account for the change in flow regime observed at higher Reynolds numbers nor the presence of the drag crisis phenomenon. The flow regime transition and the drag crisis significantly impact the lift and drag coefficients, thereby affecting the accuracy of stress calculations. Ignoring these flow regime changes can lead to incorrect predictions of stress levels in thermowells operating under such conditions.

### **Surface Features**

The standard also fails to address any design deviation besides from a tapered, stepped and straight thermowell. When it comes to the inclusion of helical strakes on the outside of the thermowell structure, the industry standards fall short in addressing this aspect comprehensively. The standard lacks specific guidelines or methodologies for accurately accounting for the effects of helical strakes, which are commonly used to modify flow characteristics and reduce vortex shedding. As a result, the standard may not provide accurate predictions for thermowells equipped with helical strakes, leading to potential errors in the stress analysis.

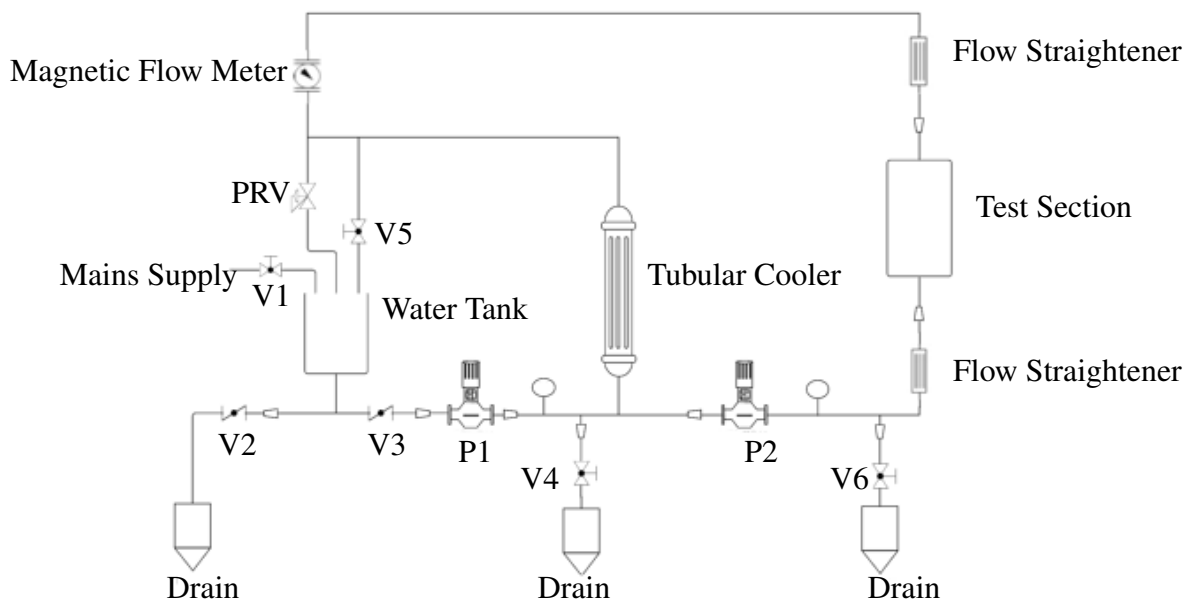


Figure 2.3: Current experimental set up of the study which needs to be adapted to a high flow rate/ low pressure flow past a thermowell.

## 2.2 Proposal for Experimental Validation Study

Prior industrial interest allows for the feasibility study for an experimental study for a thermowell testing rig designed to benchmark the numerical results is a critical step in determining the viability and practicality of such a project. This study aims to assess whether the development and implementation of the testing rig are feasible, economically sound, and aligned with the objectives of evaluating thermowell performance against established industry standards and computational models.

### 2.2.1 Existing Experimental Set Up

The sponsoring company of this project had an existing test rig in their facilities. The following proposal is to modify the existing rig in order to allow for the testing of thermowells. The rig in its existing set up can be seen in Figure 2.3.

The testing setup comprises an intricate system consisting of both an open loop and a closed loop nested within, illustrated in Figure 2.3. This system is driven by a pair of centrifugal pumps to facilitate its operation. Within the open loop, there is a water tank responsible for filling and supplying water to pump P1 in Figure 2.3. Meanwhile, the closed-loop configuration encompasses the actual test section, which is positioned downstream of these pumps.

Pump P1, a Lowara 5SVH16 model, serves as a high-pressure, low-flow-rate pump, primarily tasked with regulating the downstream pressure within the closed-loop system. This pump is located within the open loop and draws water directly from the water tank. Its outlet is connected downstream of the heat exchanger and upstream of pump P2. Pump P2, depicted in Figure 2.3, is employed to uphold the desired pressure differential and volumetric flow rate across test section. It is a Lowara 46SVH6 model, capable of generating lower pressure levels than P1 but excelling in terms of its capacity to handle higher flow rates.

Positioned within the open loop segment of the setup, P1 requires a ball valve V5 to introduce a restriction, enabling the pump to function optimally while achieving the desired downstream pressure. Ensuring the correct pressure at P1 requires configuring valve V5, attaining the target pressure without fully closing the valve. Complete closure of the valve would place the pump in a 'dead-headed' state, potentially causing damage. The adjustment of V5 also has a notable impact on the efficiency region within which pump P1 operates. Operating the pump inefficiently can result in heating of the water. An integrated shell and tube heat exchanger is positioned upstream of P2. This heat exchanger has been employed to chill cool the water passing through.

The existing rigs former purpose was to create appropriate testing conditions a flow measurement devices which required a high pressure and a low volumetric flow rate of the water. For the testing of thermowells the pressure is not of concern within the scope of this project, however, the flow rate is of the utmost importance.

### 2.2.2 Assessing Existing Set-up Capability

The volumetric flow rate capability of the existing equipment was assessed against the requirements for typical industrial use of thermowells. Data was first collected to characterise flow regimes in industry, before proceeding with the calculations of achievable flow rates given the current design. This led to the proposed design changes in the next section. This assessment involved comparing the flow rig's capabilities with those of flow rigs constructed by competitors, specifically for testing thermowell designs. Similar studies conducted by Knight et al. [60] and Lee et al. [61] were taken into consideration during this assessment. The experimental parameters for the study, by Knight et al, are found in Table 2.1.

Furthermore, the flow conditions capability of the rig was compared to the typical conditions encountered by customers who purchase thermowells. This valuable data was

provided by the previous sponsor, which highlighted various scenarios in which customers needed to install thermowells. From Table 2.1, it can be seen that the maximum thermowell

Parameter	Run 1 Value	Run 2 Value
Pipe Diameter	6"	12"
Bulk Velocity	$32.948 \text{ m s}^{-1}$	$9.05 \text{ m s}^{-1}$
Max Flow Rate	$0.598 \text{ m}^3 \text{ s}^{-1}$	$0.66 \text{ m}^3 \text{ s}^{-1}$
Thermowell Diameter	19.05 mm	19.05 mm
Length Exposed to Fluid	73.03 mm	193.68 mm
Max Pipe Reynolds Number	$2.09 \times 10^7$	$1.17 \times 10^7$
Max thermowell Reynolds Number	$2.59 \times 10^6$	$7.32 \times 10^5$
Blockage Ratio	0.172	0.051

Table 2.1: Experimental set ups for the 6" diameter pipe and the 12" diameter pipe by Knight et al. [60].

Reynolds number is around  $3 \times 10^6$ , meaning the set up can test the thermowell through all turbulent regimes. The set up also has a low blockage ratio. The flow parameters for Lee et al [61] for each run is found in Table 2.2. The comparison of the current experimental rig's

Parameter	Values				
	Run 1	Run 2	Run 3	Run 4	Run 5
Fluid Velocity	$1.07 \text{ m s}^{-1}$	$2.14 \text{ m s}^{-1}$	$3.22 \text{ m s}^{-1}$	$4.28 \text{ m s}^{-1}$	$5.82 \text{ m s}^{-1}$
Flow Rate	$0.02 \text{ m}^2 \text{ s}^{-1}$	$0.04 \text{ m}^2 \text{ s}^{-1}$	$0.06 \text{ m}^2 \text{ s}^{-1}$	$0.08 \text{ m}^2 \text{ s}^{-1}$	$0.1 \text{ m}^2 \text{ s}^{-1}$
Pressure	247690 Pa	251606 Pa	259679 Pa	271368 Pa	275048 Pa
Temperature	19.96 °C	19.99 °C	20.12 °C	20.271 °C	20.40 °C
Thermowell Reynolds Number	$2.65 \times 10^3$	$5.31 \times 10^3$	$8.02 \times 10^3$	$1.07 \times 10^4$	$1.35 \times 10^4$
Pipe Reynolds Number	$2.63 \times 10^4$	$5.27 \times 10^4$	$7.95 \times 10^4$	$1.06 \times 10^5$	$1.33 \times 10^5$

Table 2.2: Flow parameters from Okazaki test runs by Lee et al. [61].

flow capability to these typical conditions is presented in Table 2.3.

Expanding on this objective, the comparison of the flow rig's capability involved assessing factors such as flow rate, pressure, temperature, and other relevant parameters. By conducting this evaluation, it was possible to determine the suitability of the flow rig for simulating realistic flow conditions encountered in industrial applications. Additionally, the comparison with the conditions experienced by customers provided insights into the practicality and relevance of the rig's flow capability.

The data presented in Table 2.3 allows for a comprehensive understanding of how the flow rig's capabilities align with both competitor rigs and the conditions typically faced by customers. This information serves as a crucial reference for evaluating the performance and applicability of thermowell designs under different flow scenarios.



Parameter	Customer Requirements	Knight et al (2017)	Lee et al (2012)	Current Rig Capabilities
Thermowell Re	$1.94 \times 10^5 - 7 \times 10^6$	$7.32 \times 10^5 - 2.59 \times 10^6$	$2.65 \times 10^3 - 1.35 \times 10^4$	$\sim 9.67 \times 10^4$
Pipe Re	$5.39 \times 10^5 - 8.56 \times 10^7$	$4.78 \times 10^6 - 2.09 \times 10^7$	$2.63 \times 10^4 - 1.33 \times 10^5$	$\sim 2.01 \times 10^5$
Volumetric Flow Rate	$0.486 - 29.4 \text{ m}^3 \text{ s}^{-1}$	$0.598 - 0.660 \text{ m}^3 \text{ s}^{-1}$	$0.020 - 0.100 \text{ m}^3 \text{ s}^{-1}$	$\approx 0.0167 \text{ m}^3 \text{ s}^{-1}$
Pipe Diameter	0.102 - 1.016 m	0.152 - 0.305 m	0.152 m	0.102 m
Bulk Velocity	$19.26 - 123 \text{ m s}^{-1}$	$9.05 - 32.948 \text{ m s}^{-1}$	$1.07 - 5.82 \text{ m s}^{-1}$	$\sim 2.08 \text{ m s}^{-1}$
Length	155 - 310 mm	159 - 397 mm	300 mm	$\sim 66 \text{ mm}$
Tip Diameter	36 - 67 mm	19.05 mm	14.02 mm	$\sim 32 \text{ mm}$

Table 2.3: Comparison summary of experiments in literature by Lee et al. [61] and Knight et al. [54] and customer requirements by looking at an order sheet for thermowells provided by the previous sponsor of this project. The furthest right column displays the experimental rig's capability running at maximum flow rate.

The comparison presented in Table 2.3 reveals an important finding: the flow rig's capability falls short of achieving the same Reynolds number as required by customers. This discrepancy stems from a significant regime change occurring at a Reynolds number of  $3 \times 10^6$ .

Considering the flow conditions typically encountered in industry, it becomes evident that beyond this critical Reynolds number, the laminar boundary layer transitions into a turbulent regime [62]. This transition is a crucial phenomenon that must be accurately replicated by the flow rig. To elaborate further, the laminar-turbulent transition of the boundary layer significantly impacts the thermowell's behaviour and performance in real-world flow conditions. As the flow transitions from laminar to turbulent, it introduces various complexities and changes in flow patterns, such as increased turbulence intensity and altered boundary layer characteristics [63]. These changes can have a notable influence on the displacement and strain experienced by the thermowell. To ensure that the flow rig effectively simulates these important phenomena, it is essential to replicate the laminar-turbulent transition region accurately. This requires the rig to provide flow conditions that mimic the transition occurring around the critical Reynolds number. By achieving this, the rig becomes capable of simulating the realistic flow conditions experienced by customers and enables a more accurate evaluation of thermowell performance.

It is evident that the rig's current capability falls short in reproducing the laminar-turbulent transition at the desired Reynolds numbers. As a result, it becomes crucial to address this limitation and explore potential modifications or improvements to the rig that would enable it to replicate this critical flow regime accurately.

### 2.2.3 Proposed Modifications

Upon thorough analysis, several desirable modifications to the flow rig have been identified to address its limitations and enhance its capability for simulating realistic flow conditions and evaluating thermowell performance.

One key change is an increase in the flow rate. This can be achieved through adjustments to the pump or pump configuration. For instance, configuring the pumps in parallel can effectively boost the flow rate. By increasing the flow rate, the rig can better approximate the desired Reynolds numbers and offer a higher velocity of fluid passing through the system.

Additionally, a higher flow rate opens up the possibility of using a larger pipe diameter, allowing for a longer thermowell. This longer thermowell can help lower the first modal frequency, thus more easily allowing for the testing of the thermowells at with vortex shedding frequencies closer to their first natural frequency and allowing for larger displacements. A desirable modification is the implementation of a stand-off mechanism. The stand-off provides additional length to the thermowell and partially shields it from the flow as seen in Figure 1.3. This configuration more accurately replicates the conditions experienced by thermowells installed in practical industrial applications. However, it is important to consider that the introduction of a stand-off may pose challenges when benchmarking the numerical model against the experimental setup. The presence of the stand-off alters the flow characteristics around the thermowell, potentially affecting the measurements. Calibration and careful consideration are necessary to ensure that the numerical model accurately captures the effects of the stand-off on the thermowell's behaviour. By incorporating these proposed changes, the flow rig's capability can be significantly improved to be able to detect thermowell displacements and cover all turbulent regimes. The addition of a safety net or grid downstream of the test area must also be added to the rig in order to stop a thermowell from damaging downstream equipment such as the pumps if the thermowell were to fail. The most cost effective method was the setup in the Figure 2.4.

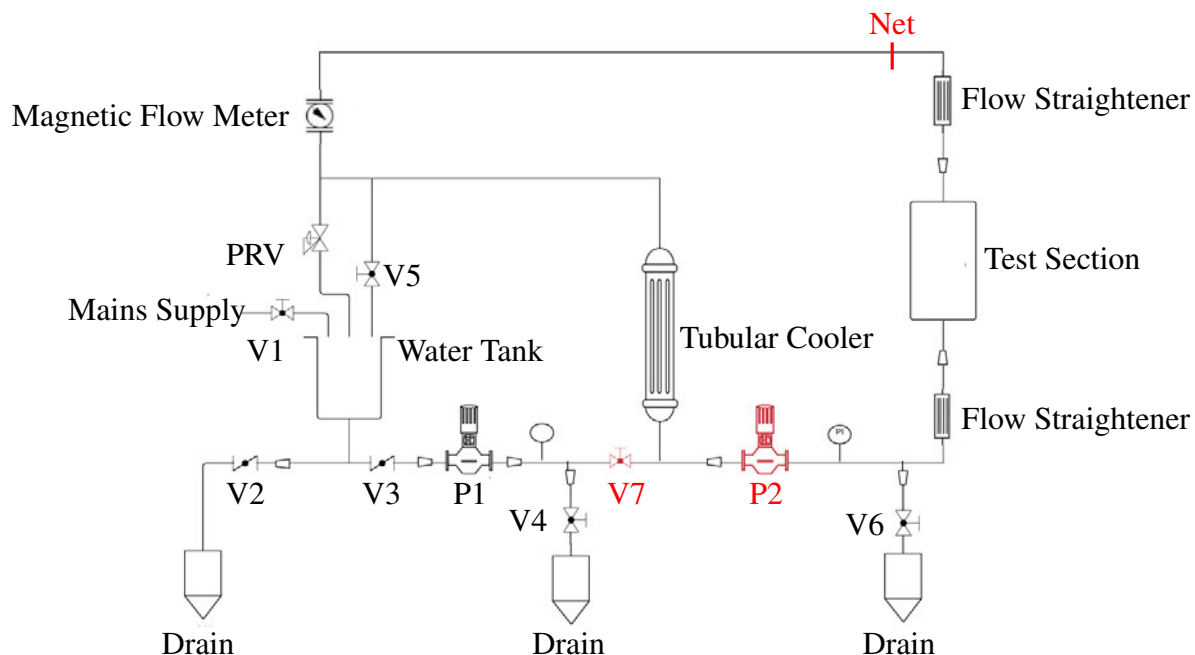


Figure 2.4: Set of of the proposed rig.

This required an additional valve to be installed (see V7 in Figure 2.4), to close the loop and allow the flow rate to be solely determined by P2 which was to be replaced with a pump of higher flow rate. The pump proposed was a Lowara W45VCC4 model vertical high volumetric flow rate pump. This pump was capable of  $900 \text{ m}^3 \text{ h}^{-1}$ . Installing a stand-off was not desirable to compare with numerics. The thermowell proposed for testing was a straight stemmed thermowell with a flanged mounting. The following dimensions of the thermowell were proposed in Table 2.4.

Thermowell Component	Dimension [mm]
Unsupported Length	66
Diameter	21
100	15
150	3
195	3

Table 2.4: Dimensions of a proposed thermowell to be tested in the experimental rig.

With a pipe of 6” diameter in the test section, the thermowell proposed would have had a Reynolds number of around  $4.5 \times 10^5$  at maximum pump capability, a significant improvement on the previous setup. To measure the thermowell response an accelerometer small enough

to be placed into a thermowell was priced and ordered. This accelerometer (Triaxial ICP® Accelerometer) was a cubic shape ( $10.2 \times 19.1 \times 10.2$ ) mm was planned to take acceleration data vs flow rate data taken by the magnetic flow meter. This information would allow for direct comparison to the solid solver results found in Chapter 5. However, The experiments could not be run due to financial restraints. The alteration was costed at £10,000.00, which was beyond the financial commitment of the project sponsor. The updated design was adopted as a project output for future consideration but could not be implemented for experimental work within this project. A design of a thermowell with the added feature of helical strakes could then be developed for testing with the same type mounting, stem and dimensions as the straight thermowell for a comparison of structural response.

## 2.3 Conclusions

This chapter provides an overview of the current industry standards and practices for predicting the structural response of thermowells in flow processes. It outlines the key requirements and calculations involved in sizing thermowells according to the ASME PTC 19.3 TW-2016 standards. These standards consider factors such as natural frequency, dynamic stress, steady-state stress, and pressure to ensure the safe and reliable operation of thermowells in various flow environments.

The assumptions made in the industry standards were reviewed to understand what approximations and errors may be introduced in the calculations. These assumptions include the neglect of the effects of flow over the thermowell tip, and using fixed lift and drag coefficients ignoring the change in turbulent regime. These assumptions can lead to inaccuracies in predicting thermowell behaviour, especially in real-world applications. The changes in Strouhal number above  $5 \times 10^5$  seen in sources of literature are ignored or unexplored as seen in many studies reported in [64].

Furthermore, the chapter proposes an experimental validation study to benchmark the displacement measurements of thermowells in high Reynolds number flow. The study aims to assess the flow rig's capability to replicate realistic flow conditions and evaluate thermowell performance accurately. The proposed modifications to the flow rig include increasing the flow rate, implementing a stand-off mechanism, and addressing the laminar-turbulent transition region. A experimental setup is proposed.

In conclusion, this chapter sheds light on the current industry practices for thermowell sizing and highlights the need for experimental validation to improve the accuracy of predictions. By addressing the limitations of the flow rig and incorporating proposed modifications, it becomes possible to better reproduce real-world flow conditions and enhance the reliability of thermowell performance assessments. This chapter clearly identifies the areas for improvement from the industry standards in line with objective 2 identified in Section [1.5.1](#).

# Chapter 3

## Fluid Mechanics Computational Modelling

This chapter provides a fundamental background on fluid mechanics, which is essential for the understanding and implementation of CFD simulations. The chapter begins by introducing the basic conservation laws of fluid mechanics, including conservation of mass, momentum, and energy as well as the constitutive equations closing the system of equations need to solve a fluid flow. The chapter then discusses boundary conditions, which are crucial for defining the fluid flow problem. Relevant parameters, such as Reynolds number, Strouhal number, lift and drag coefficients, are also discussed, and their relevance to fluid flow is highlighted.

Furthermore, the chapter covers the physics of turbulence, which is an intrinsic part of many fluid flow problems. Finally, the chapter provides an overview of CFD, including the numerical methods used to discretise and solve the governing equations, as well as meshing and the software packages commonly used for CFD simulations.

### 3.1 Aspects of Fluid Mechanics

This section aims to establish a foundational understanding of fluid mechanics from a physics perspective, including relevant parameters.

#### 3.1.1 Conservation Laws

Conservation laws in CFD form the fundamentals of our understanding and simulation of fluid flow phenomena. These fundamental principles, which encompass the conservation of

mass, momentum, and energy, underpin the mathematical and computational frameworks that allow us to model and analyse fluid dynamics. The concept of conservation laws is rooted in the fundamental physical laws of nature, and in the context of CFD, it serves as the cornerstone for accurate and reliable simulations. These laws dictate how mass, momentum, and energy are conserved within a fluid domain, providing the foundation upon which CFD solvers are built. In this introductory exploration, we will delve into the core principles of conservation laws in CFD. In this case, the energy equation is ignored as throughout this project, incompressible flow is simulated.

### Conservation of Mass

To interpret the conservation of mass law, it may be simple to consider a infinitesimally small control volume fixed in space. This element is of the volume  $\Omega$  bounded by the surface  $S = \partial\Omega$ . The rate of increase of mass inside this fluid element must be equal to the net rate of mass flow into the fluid element. Using divergence theorem for the mass flux  $\rho\mathbf{u}$  we state that the net flow of mass into a fluid element as

$$\int_{\Omega} \left( \frac{\partial \rho}{\partial t} + \nabla \cdot (\rho\mathbf{u}) \right) d\Omega = 0. \quad (3.1)$$

Setting the integrand of the volume integral to zero due to the fact that this equation must hold for any arbitrary volume we then get the following relation

$$\frac{\partial \rho}{\partial t} + \nabla \cdot (\rho\mathbf{u}) = 0. \quad (3.2)$$

For an incompressible flow, given that the density of the fluid in a given fluid element will not change, we can set the time derivative of density to zero so the following statement is true:

$$\frac{d\rho}{dt} = 0. \quad (3.3)$$

Substituting the above equation into (3.1), the equation reduces to  $\rho\nabla\mathbf{u} = 0$  and hence

$$\nabla \cdot \mathbf{u} = 0. \quad (3.4)$$

### Conservation of Momentum

The momentum equations represent Newton's second law which states that the rate of change of momentum of a fluid element is equal to the sum of all the forces acting upon it. Consider a moving mass of fluid in the domain  $\Omega$  enclosed by the surface  $S = \partial\Omega$ . These forces can be broadly classified into two types: body forces and surface forces. Body forces act throughout the fluid volume and are typically represented by a force per unit mass term. Gravitational force is an example of a body force. On the other hand, surface forces act on the surface of the fluid element and can be further classified into pressure forces and shear forces. Pressure forces arise due to the variation of pressure over the surface of the fluid element, whereas shear forces arise due to the tangential stress at the surface.

As the mass is moving we must use the substantial derivative on the total momentum of the fluid element this takes into account the time rate of change of momentum due to the movement of the control volume as follows,

$$\frac{D}{Dt} \int_{\Omega} \rho \mathbf{u} d\Omega = \int_{\Omega} \mathbf{f} d\Omega + \int_S \boldsymbol{\tau} dS, \quad (3.5)$$

where  $\mathbf{f}$  is body force per unit volume and  $\boldsymbol{\tau}$  is surface force per unit of surface area (traction) [65]. The traction force vector,  $\boldsymbol{\tau}$ , can be written in terms of the stress tensor by the following relation,

$$\boldsymbol{\tau} = \boldsymbol{\sigma} \mathbf{n}, \quad (3.6)$$

where  $\boldsymbol{\sigma}$  is the Cauchy stress tensor for a fluid. Equation (3.5) can be converted into an equation only containing Eulerian derivatives using Reynolds transport theorem (inclusion of the convective term) to take into account an element volume that is static as fluid passes through it. The traction force equation can also be substituted in to give

$$\int_{\Omega} \left( \frac{\partial}{\partial t} (\rho \mathbf{u}) + (\mathbf{u} \cdot \nabla) \rho \mathbf{u} \right) d\Omega = \int_{\Omega} \mathbf{f} d\Omega + \int_{\Omega} \nabla \cdot \boldsymbol{\sigma} d\Omega. \quad (3.7)$$

Applying this equation to any arbitrary volume and assuming the fluid is incompressible we get the following momentum equation [66]:

$$\rho \frac{\partial \mathbf{u}}{\partial t} + \rho \nabla \cdot (\mathbf{u} \otimes \mathbf{u}) = \nabla \cdot \boldsymbol{\sigma} + \mathbf{f}. \quad (3.8)$$



When it is assumed that the fluid is incompressible (no change in fluid density locally), the energy equation is not considered and the continuity can be simplified into the divergence free constraint in equation (3.4).

### 3.1.2 Constitutive laws

The constitutive law, often referred to as the constitutive equation, describes how the stress tensor is related to the velocity gradient (rate of deformation) in a fluid. It characterises the flow behaviour of different types of fluids, such as Newtonian fluids, non-Newtonian fluids, or viscoelastic fluids. By incorporating the constitutive law into the governing equations of the physical system, it provides closure by linking the stresses or strains to the velocities within the system.

The relationship between the Cauchy stress tensor and the strain rate tensor must be derived. The strain rate tensor is

$$\boldsymbol{\varepsilon} = \frac{1}{2} (\nabla \mathbf{u} + \nabla \mathbf{u}^T). \quad (3.9)$$

The strain rate tensor represents  $\boldsymbol{\varepsilon}(p,t)$  the rate at which the mean velocity changes in the medium as one moves away from point  $p$ . The Cauchy stress tensor can be written as

$$\boldsymbol{\sigma} = -p\mathbf{I} + \boldsymbol{\tau}, \quad (3.10)$$

where  $p$  is the hydrostatic pressure,  $\mathbf{I}$  is the identity matrix and  $\boldsymbol{\tau}$  is the viscous stress tensor. The first term is the hydrostatic pressure and the second term is the deviatoric stress otherwise known as the normal stress vector and the shear stress tensor. The deviatoric stress tensor is a function of the strain rate tensor. Newton suggested shear stress in a fluid is related to the time rate of strain linearly. Fluids in which it is assumed  $\boldsymbol{\tau}$  is directly proportional to  $\boldsymbol{\varepsilon}$  are called Newtonian fluids.

$$\boldsymbol{\sigma} = -p\mathbf{I} + 2\mu\boldsymbol{\varepsilon} + \lambda\mathbf{I}\text{tr}(\boldsymbol{\varepsilon}). \quad (3.11)$$

where  $\mu$  is the fluid dynamic viscosity,  $\lambda$  is second coefficient of viscosity,  $\text{tr}()$  is the trace operator. For an incompressible fluid,  $\nabla \cdot \mathbf{u} = 0$  and therefore  $\text{tr}(\boldsymbol{\varepsilon}) = 0$ . This simplifies the relation to the following

$$\boldsymbol{\sigma} = -p\mathbf{I} + 2\mu\boldsymbol{\varepsilon}. \quad (3.12)$$

Relating back to the momentum equation and therefore closing the system of equations by substituting (3.12) into (3.8), for an incompressible fluid, the momentum equation can be written as

$$\rho \frac{\partial \mathbf{u}}{\partial t} + \rho \nabla \cdot (\mathbf{u} \otimes \mathbf{u}) = -\nabla p + \mu \nabla \cdot [(\nabla \mathbf{u} + \nabla \mathbf{u}^T)] + \mathbf{f}. \quad (3.13)$$

The momentum equation can be separated into its terms for better understanding. The time variation term is represented by  $\frac{\partial \mathbf{u}}{\partial t}$ , the convection term is represented by  $\mathbf{u} \otimes \mathbf{u}$ , the diffusion term contained in the stress term as  $\mu \nabla \cdot [(\nabla \mathbf{u} + \nabla \mathbf{u}^T)]$  and the pressure gradient term is  $-\nabla p$ .

### 3.1.3 Turbulence

Turbulence models are employed to address the diffusion term of (3.13). The main purpose of a turbulence model is to provide closure for the governing equations of fluid flow by modelling the effects of turbulence. In reality, the direct numerical simulation of turbulent flows is computationally expensive and often infeasible due to the wide range of length and time scales involved.

Direct Numerical Simulations, DNS, assumes the flow to be fully resolved at the smallest scales. However, in many practical situations, there may be physical or geometric constraints that prevent resolving all the turbulent scales accurately. For example, in complex geometries or near-wall flows, resolving the smallest turbulent structures may require an excessively fine grid or boundary layer resolution, which may not be practical or even possible. Turbulence models offer a practical way to simulate and predict the behaviour of turbulent flows by providing approximations and simplifications based on empirical or theoretical considerations.

Turbulence models incorporate additional transport equations, known as Reynolds-averaged Navier-Stokes (RANS) equations, to account for the turbulent fluctuations in the flow. These additional equations represent the turbulent quantities, such as turbulent kinetic energy and turbulent viscosity, which capture the effects of turbulence on the mean flow field.

#### Reynolds Averaged Navier Stokes Equations (RANS)

A widely used approximation for applications of CFD is to average out the turbulent equations in time over the whole spectrum of turbulent fluctuations leading to the RANS equations. The most common turbulence models which use this approach are the  $k - \varepsilon$ ,  $k - \omega$

and the  $k - \omega$  shear stress transport (SST) turbulence models. These approaches significantly reduce computational expense rather than solving the Navier Stokes equations directly. They assume that the Reynolds stresses are directly proportional to the rate of deformation of the fluid, this is called the Boussinesq hypothesis. The turbulence model used predominately in this thesis is the  $k - \omega$  SST turbulence model.

The  $k - \omega$  SST model incorporates the  $k - \varepsilon$  and the  $k - \omega$  and is described by Menter [67]. It is known that the  $k - \varepsilon$  model is not able to capture the proper behaviour of turbulent boundary layers up to separation. Also, the  $k - \omega$  model does not properly capture the behaviour of flow with induced pressure separation and the  $\omega$  equation is too sensitive to the value of  $\omega$  in the free stream outside the boundary layer. So, the  $k - \omega$  SST model was developed to balance each models shortcomings. The model essentially switches between  $k - \varepsilon$  and  $k - \omega$  for volumes outside or inside the turbulent boundary layer respectively. The model is a two equation model defined as follows,

$$\frac{\partial \mathbf{u}}{\partial t} + \nabla \cdot (\mathbf{u} \otimes \mathbf{u}) = -\frac{1}{\rho} \nabla p + \nabla \cdot [(v + \nu_t)((\nabla \mathbf{u}) + (\nabla \mathbf{u}^T)) - \frac{2}{3} k \mathbf{I}] \quad (3.14a)$$

$$\frac{\partial k}{\partial t} + \nabla \cdot (\mathbf{u}k) = \nabla \cdot \left( (v + \nu_t \sigma_k) \nabla k \right) + \frac{P_k}{\rho} - \beta^* k \omega \quad (3.14b)$$

$$\frac{\partial \omega}{\partial t} + \nabla \cdot (\mathbf{u}\omega) = \nabla \cdot \left( (v + \nu_t \sigma_\omega) \nabla \omega \right) + \frac{\alpha}{\mu_t} P_k - \beta^* \omega^2 + 2(1 - F_1) \frac{\sigma_{w2}}{\omega} \nabla k \cdot \nabla \omega, \quad (3.14c)$$

where  $k$  is the kinetic turbulent energy,  $\omega$  is the specific turbulent dissipation, and  $\nu_t$  is the turbulent viscosity. The turbulent viscosity is defined as

$$\nu_t = a_1 \frac{k}{\max(a_1 \omega, F_{23} S)}. \quad (3.15)$$

$\nu_t$  has a blending function making the term is a viscosity limiter and the blending function  $F_{23}$  is calibrated empirically.  $\nu_t$  remains the original equation for mesh cells further away from the wall and is limited close to the wall. The eddy viscosity is limited to give an improved performance in flows with adverse pressure gradients and wake regions such as many examples of flow past an object. The  $k - \omega$  SST model used in this study is that described by Menter in 2003 [67, 68] with the constants found in Table 3.1.

$\beta^*$	$\alpha_1$	$\beta_1$	$\sigma_{k1}$	$\sigma_{\omega 1}$	$\alpha_2$	$\beta_2$	$\sigma_{k2}$	$\sigma_{\omega 2}$
0.09	5/9	3/40	0.85	0.5	0.44	0.0828	1	0.856

Table 3.1: Constants used by Menter [67] for  $k - \omega$  SST formulation.

Blending functions are used to achieve a smooth transition between the  $k - \omega$  model for near wall turbulence and the  $k - \varepsilon$  model for far field turbulence. Blending functions are also used for model constants that take constant  $C_1$  from the  $k - \omega$  model and the constant  $C_2$  from the  $k - \varepsilon$  model and the transformed SST model presents the following:

$$C = F_c C_1 + (1 - F_c) C_2.$$

When using a software package such as OpenFOAM, the user can input the type of blending function required (i.e stepped, linear, binomial etc.) to get accurate smoothing of the turbulence values at the boundary layer. In this study the selected blending function was that of the stepped function due to its low computational expense.

### 3.1.4 Physical Boundary Conditions

In Computational Fluid Dynamics (CFD) simulations, different types of boundary conditions are applied to define the behaviour of fluid flow at the boundaries of the computational domain. These boundary conditions play a crucial role in accurately representing the physical system being modelled.

**Inlet Boundary Condition:** This type of boundary condition specifies the properties of the incoming fluid entering the computational domain. Parameters such as velocity, pressure, and temperature are typically prescribed to represent the desired flow conditions at the inlet. Inlet conditions are crucial for initiating and defining the flow field within the domain. The inlet boundary conditions used in the  $k - \omega$  SST and in this work are as follows:

$$\mathbf{u} = (u_x \ 0 \ 0) \quad \text{on} \quad \partial\Omega_{\text{Inlet}} \times [0, T] \quad (3.16a)$$

$$\nabla p \cdot \hat{\mathbf{n}} = 0 \quad \text{on} \quad \partial\Omega_{\text{Inlet}} \times [0, T] \quad (3.16b)$$

$$k = 1.50 (0.16 u_x Re^{-1/8})^2 \quad \text{on} \quad \partial\Omega_{\text{Inlet}} \times [0, T] \quad (3.16c)$$

$$\omega = \frac{\sqrt{k}}{0.07D(0.09^{0.25})} \quad \text{on} \quad \partial\Omega_{\text{Inlet}} \times [0, T] \quad (3.16d)$$

$$v_t = 0 \quad \text{on} \quad \partial\Omega_{\text{Inlet}} \times [0, T]. \quad (3.16e)$$

Outlet Boundary Condition: The outlet boundary condition defines the flow properties at the exit of the computational domain. Typically, the outlet pressure is specified to represent the desired flow conditions at the domain's outflow. The outlet boundary conditions used in the  $k - \omega$  SST and in this work are as follows:

$$\mathbf{u} \cdot \hat{\mathbf{n}} = 0 \quad \text{on } \partial\Omega_{\text{Outlet}} \times [0, T] \quad (3.17a)$$

$$p = 0 \quad \text{on } \partial\Omega_{\text{Outlet}} \times [0, T] \quad (3.17b)$$

$$\nabla k \cdot \hat{\mathbf{n}} = 0 \quad \text{on } \partial\Omega_{\text{Outlet}} \times [0, T] \quad (3.17c)$$

$$\nabla \omega \cdot \hat{\mathbf{n}} = 0 \quad \text{on } \partial\Omega_{\text{Outlet}} \times [0, T] \quad (3.17d)$$

$$v_t = 0 \quad \text{on } \partial\Omega_{\text{Outlet}} \times [0, T]. \quad (3.17e)$$

Wall Boundary Condition: The wall boundary condition is applied to surfaces where fluid flow directly interacts with solid boundaries. This condition assumes a no-slip condition, meaning the fluid velocity at the wall is zero. The wall boundary conditions used in the  $k - \omega$  SST and in this work are as follows:

$$\mathbf{u} = \mathbf{0} \quad \text{on } \partial\Omega_{\text{Wall}} \times [0, T] \quad (3.18a)$$

$$\nabla p \cdot \hat{\mathbf{n}} = 0 \quad \text{on } \partial\Omega_{\text{Wall}} \times [0, T] \quad (3.18b)$$

$$\nabla k \cdot \hat{\mathbf{n}} = 0 \quad \text{on } \partial\Omega_{\text{Wall}} \times [0, T] \quad (3.18c)$$

$$\omega = f(\omega_{vis}, \omega_{log}) \quad \text{on } \partial\Omega_{\text{Wall}} \times [0, T] \quad (3.18d)$$

$$v_t = f(v_{tvis}, v_{tlog}) \quad \text{on } \partial\Omega_{\text{Wall}} \times [0, T]. \quad (3.18e)$$

Note that wall functions are used in this work, this will be further discussed in section 3.1.6. Symmetry Boundary Condition: The symmetry boundary condition is utilised when the computational domain exhibits a symmetry plane. This condition reflects the symmetry of the flow field by prescribing that properties such as velocity or pressure are symmetric across the symmetry plane. It allows for reducing the computational domain size by considering only one portion of the symmetrical geometry. The symmetry boundary conditions used in the  $k - \omega$  SST in this work are seen in the (3.19).

$$\mathbf{u} = (u_x \ 0 \ 0) \quad \text{on } \partial\Omega_{\text{Sym}} \times [0, T] \quad (3.19a)$$

$$\nabla p \cdot \hat{\mathbf{n}} = 0 \quad \text{on } \partial\Omega_{\text{Sym}} \times [0, T] \quad (3.19b)$$

$$\nabla k \cdot \hat{\mathbf{n}} = 0 \quad \text{on } \partial\Omega_{\text{Sym}} \times [0, T] \quad (3.19c)$$

$$\nabla \omega \cdot \hat{\mathbf{n}} = 0 \quad \text{on } \partial\Omega_{\text{Sym}} \times [0, T] \quad (3.19d)$$

$$\nabla v_t \cdot \hat{\mathbf{n}} = 0 \quad \text{on } \partial\Omega_{\text{Sym}} \times [0, T]. \quad (3.19e)$$

Cyclic Boundary Condition: The cyclic boundary condition is employed in situations where periodicity or symmetry exists within the computational domain. This condition ensures that the flow field behaves cyclically, allowing for a seamless connection between two boundary regions. It is particularly useful in cases where the same flow pattern repeats periodically within the domain. The cyclic boundary conditions used in the  $k - \omega$  SST and in this work are as follows:

$$\mathbf{u}_1 = \mathbf{u}_2 \quad \text{on } \partial\Omega_{\text{Cyclic1}} \times [0, T] \quad (3.20a)$$

$$\mathbf{u}_2 = \mathbf{u}_1 \quad \text{on } \partial\Omega_{\text{Cyclic2}} \times [0, T] \quad (3.20b)$$

$$p_1 = p_2 \quad \text{on } \partial\Omega_{\text{Cyclic1}} \times [0, T] \quad (3.20c)$$

$$p_2 = p_1 \quad \text{on } \partial\Omega_{\text{Cyclic2}} \times [0, T] \quad (3.20d)$$

$$k_1 = k_2 \quad \text{on } \partial\Omega_{\text{Cyclic1}} \times [0, T] \quad (3.20e)$$

$$k_2 = k_1 \quad \text{on } \partial\Omega_{\text{Cyclic2}} \times [0, T] \quad (3.20f)$$

$$\omega_1 = \omega_2 \quad \text{on } \partial\Omega_{\text{Cyclic1}} \times [0, T] \quad (3.20g)$$

$$\omega_2 = \omega_1 \quad \text{on } \partial\Omega_{\text{Cyclic2}} \times [0, T] \quad (3.20h)$$

$$v_{t1} = v_{t2} \quad \text{on } \partial\Omega_{\text{Cyclic1}} \times [0, T] \quad (3.20i)$$

$$v_{t2} = v_{t1} \quad \text{on } \partial\Omega_{\text{Cyclic2}} \times [0, T]. \quad (3.20j)$$

The cyclic boundary condition ensures that the flow variables on one side of the boundary are matched with the corresponding variables on the opposite side, enabling a seamless and cyclic flow behaviour within the specified regions.

### 3.1.5 Relevant Parameters

In this subsection, a set of crucial parameters will be explored, providing the foundation for comprehending and characterising fluid flow behaviour. These parameters offer valuable insights into the dynamics of fluid motion, turbulence, and the interaction between solid structures and the surrounding fluids. Through a detailed examination of these parameters, a comprehensive framework for interpreting and evaluating the computational study's results will be established.

#### Reynolds Number

The Reynolds number is a dimensionless quantity used to describe the flow of a fluid, whether it be a liquid or a gas. The Reynolds number is defined as the ratio of inertial forces to viscous forces within a fluid, as given in (2.1). The Reynolds number is used in this study as an indicator to which type of turbulence is occurring in the wake and boundary layer of the cylinder. It is also used as a benchmark against other parameters in comparison to other published work. The Reynolds number can be used to predict the type of flow that a fluid will exhibit, such as laminar or turbulent. A low Reynolds number indicates that the flow is laminar, while a high Reynolds number indicates that the flow is turbulent. In general, a transition from laminar to turbulent flow occurs at a critical Reynolds number that depends on the specific fluid and the flow conditions.

The Reynolds number is particularly important for the flow around a cylinder, as it determines whether the flow is laminar or turbulent. This, in turn, affects the drag force and pressure distribution on the cylinder. At low Reynolds numbers, the flow around a cylinder is typically laminar, with smooth and predictable flow patterns. In this regime, the drag force on the cylinder is relatively low and the pressure distribution is relatively symmetric. This is why streamlined shapes, like those used in submarines or high-speed trains, have a low drag coefficient and are often designed to promote laminar flow. However, as the Reynolds number increases, the flow around the cylinder becomes increasingly unstable and can transition to turbulent flow. In this regime, the flow patterns become chaotic and unpredictable, leading to higher drag forces and more asymmetric pressure distributions on the cylinder.

### Lift and Drag Coefficients

Lift and drag coefficients are dimensionless quantities used to describe the aerodynamic forces acting on an object, such as an airfoil, or a cylinder moving through a fluid. They are important parameters for the design and analysis of aircraft, wind turbines, and other engineering applications. The lift coefficient and drag coefficient depend on various factors, such as the shape of the object, the angle of attack, the fluid properties, and the velocity of the fluid. Engineers use wind tunnel tests and computational fluid dynamics (CFD) simulations to determine these coefficients and optimise the design of the object. They can provide insight into the aerodynamics involved in changing a thermowell design.

The lift coefficient and drag coefficients are dimensionless numbers that represent the ratio of the lift or drag force to the dynamic pressure and the reference area of the object. The lift and drag coefficients are defined as

$$C_L = \frac{\mathbf{F} \cdot \mathbf{y}}{0.5\rho AU_{ref}^2} \quad (3.21a)$$

$$C_D = \frac{\mathbf{F} \cdot \mathbf{x}}{0.5\rho AU_{ref}^2}, \quad (3.21b)$$

where  $\mathbf{F}$  is defined as the total force vector acting on the geometry,  $\rho$  is the density of the fluid and  $u$  is the velocity of the fluid relative to the object,  $A$  is the reference area of the object, which is usually the frontal area. Lift is the force perpendicular to the direction of the fluid flow, which opposes the dynamic pressure of the fluid, which is defined as  $0.5\rho\|u\|^2$ . Drag is the force parallel to the direction of the fluid flow, which opposes the motion of the object. The total force exerted upon an object is defined as

$$\mathbf{F} = \sum_i \rho \mathbf{s}_{f,i} (p_i - p_{ref}) + \mathbf{s}_{f,i} \cdot (\mu \mathbf{R}_{dev}), \quad (3.22)$$

where  $\rho$  is the density,  $\mathbf{s}_{f,i}$  the face area vector of each face of every control volume on the cylinder,  $p$  the pressure,  $\mu$  the dynamic viscosity and  $\mathbf{R}_{dev}$  the deviatoric stress tensor.

The lift and drag coefficients are used in this work to monitor the fluctuation in transverse and in-line pressure on the cylinder wall. This monitoring will provide the frequency of vortex shedding by analysing the frequency at which the lift oscillates. The average drag coefficient is also an indicator to which turbulence regime is present.



### Strouhal number

The Strouhal number is a dimensionless quantity used to describe the behaviour of oscillating systems, such as flow over a cylinder. It is named after the Czech physicist and mathematician Vincenc Strouhal. The Strouhal number is defined as the ratio of the product of frequency of vortex shedding and the characteristic length to the velocity of the fluid. It is calculated as follows

$$St = \frac{fD}{u}, \quad (3.23)$$

where  $f$  is the frequency of vortex shedding,  $D$  is the characteristic length of the oscillating system (such as the diameter of a cylinder),  $u$  is the velocity of the fluid. The Strouhal number is important and used in this work because it describes the relationship between the shedding of vortices and the frequency of oscillation of an object in a fluid flow.

### Wall Proximity

For turbulent flow conditions, the velocity profile can be divided into two regions: the viscous sublayer and the inertial layer. The inertial layer is found near a wall and the inertial layer is found further away from the wall. Velocity in the viscous sublayer is not greatly affected by the bulk flow velocity so the velocity must be alternatively calculated. The location of the transition between the two layers depends on the Reynolds number. In order to resolve the boundary layer in the near wall region the surrounding mesh must reach an appropriate fineness. The  $y^+$  of the viscous sublayer is defined by equation (3.24)

$$y^+ = \frac{\rho y u_\tau}{\mu}, \quad (3.24)$$

where  $u_\tau$  is the viscous velocity at the wall,  $y$  is the distance to the nearest wall,  $\rho$  is the fluid velocity and  $\mu$  is the local viscosity. A general requirement for simulating a turbulent flow is to achieve a  $y^+$  value of 1 through grid refinement. However, wall functions are commonly used to reduce the computational expense by allowing the reduction of grid resolution in the near wall region and allowing for a larger  $y^+$  value. Each wall function or turbulence model has limitations and recommended ranges of the  $y^+$  value.

### 3.1.6 Wall Functions

The use of a wall function in computational fluid dynamics (CFD) simulations is motivated by the need to capture the flow behaviour near solid walls while reducing computational costs. In CFD simulations, the region near a solid wall is characterized by a thin layer called the boundary layer, where velocity gradients and turbulent fluctuations are particularly intense. Resolving the boundary layer with a fine computational mesh throughout the entire domain can be computationally expensive, especially for large-scale simulations.

To address the large velocity gradient near the wall in CFD simulations, a linear piecewise approach is often used when a wall function is not employed. In this approach, the velocity is computed at the cell centre of each cell adjacent to the wall. However, since the velocity profile is non-linear, a fine resolution mesh is required in the near-wall region to capture the gradient and flow behaviour accurately. Alternatively, if a non-linear solution could predict the velocity, the number of cells in the near-wall region could be significantly reduced, allowing for a coarser mesh.

Wall functions provide an empirical approach to approximate the velocity behaviour near the wall. They are derived from observed velocity profiles and serve as a means to simplify the modelling process. There are various wall functions available for selection when setting up a CFD simulation. These wall functions are typically chosen based on their accuracy and suitability for specific flow conditions and geometries. Selecting an appropriate wall function is essential for accurately capturing the flow behaviour near the wall while also maintaining computational efficiency.

The purpose of a wall function is to provide an approximate representation of the flow near the wall without explicitly resolving the thin boundary layer. It allows for the use of a coarser computational mesh in the vicinity of the wall.

However, it's important to note that wall functions introduce certain limitations and assumptions. They are valid for fully turbulent flows and typically work best in cases where the flow is fully developed and the Reynolds number is sufficiently high. Wall functions may not accurately capture the flow near the wall in transitional or laminar flows, or in flows with specific wall treatments or complex wall geometries.

The wall functions for both the energy dissipation rate and turbulent viscosity are defined as

$$f(\omega_{vis}, \omega_{log}) = \begin{cases} \omega_{vis} = \frac{6v_w}{\beta_1 y^2} & \text{for } y^+ \leq y_{lam}^+ \\ \omega_{log} = \frac{\sqrt{k}}{C_\mu \kappa y} & \text{for } y^+ > y_{lam}^+ \end{cases} \quad (3.25)$$

$$f(v_{tvis}, v_{tlog}) = \begin{cases} v_{tvis} = 0 & \text{for } y^+ \leq y_{lam}^+ \\ v_{tlog} = v_w \left( \frac{y^+ \kappa}{\ln(Ey^+)} - 1 \right) & \text{for } y^+ > y_{lam}^+ \end{cases}. \quad (3.26)$$

In this work, step functions were used to distinguish between the viscous layer and the logarithmic layer of the overall boundary layer [69]. The logarithmic layer, is a region within the boundary layer that is characterised by a logarithmic velocity profile. It is located above the viscous sublayer and extends towards the outer region of the boundary layer. In this layer, the velocity of the fluid increases logarithmically with respect to the distance from the wall. The log layer is primarily influenced by the turbulent fluctuations and eddies present in the flow.

The viscous layer, also known as the laminar sublayer, is the region closest to the wall within the boundary layer. It is characterised by a slow and smooth velocity gradient, where the velocity profile is mostly linear. In this layer, viscous effects dominate, and the flow is predominantly laminar. The thickness of the viscous layer is typically on the order of the molecular mean free path and can be very thin.

## 3.2 Computational Fluid Dynamics

Computational fluid dynamics (CFD) is the analysis of systems involving fluid flow, heat transfer and associated phenomena by numerical techniques and computational simulation. All CFD codes are composed of a pre-processor, a solver and a post-processor. The pre-processor consists of defining the region of interest, generating a mesh of the geometry, selecting the physical phenomena to be modelled, defining fluid properties and defining boundary conditions. The solver will produce a solution for the velocity field and the pressure field of the fluid via its given method. The accuracy of the solution depends on the mesh density and, for a non-uniform mesh, the density distribution depending on the geometry.

All CFD techniques are based on the conservative and constitutive equations of fluid dynamics. These CFD equations are based on conservation principles; conservation of mass,

Newton's second law and the first law of thermodynamics. The finite volume method numerical algorithm consists of integrating these equations over all finite volumes in the mesh, discretising the equations to a system of algebraic equations and then solving the system of equations by some iterative method. When it is assumed that the fluid is incompressible (no change in fluid density locally), the energy equation is not considered as it becomes mathematically decoupled from the mass and momentum equations.

### 3.2.1 Software

OpenFOAM (Open-source Field Operation And Manipulation) software was used to simulate the fluid flow around a cylindrical bluff body. OpenFOAM works by using numerical methods to solve the equations that govern fluid flow, heat transfer, and other related phenomena. These equations are typically represented as partial differential equations (PDEs), which describe the behaviour of the fluid and the effects of various physical forces and boundary conditions. OpenFOAM provides a set of solvers, or numerical algorithms, that can solve these PDEs for different types of fluid flow problems. Each solver uses a specific algorithm that is optimised for a particular type of problem. To use OpenFOAM, the user must first set up a simulation by defining the geometry of the fluid domain, the physical properties of the fluid, and the boundary conditions that govern the behaviour of the fluid at the boundaries of the domain.

OpenFOAM is a C++ toolbox for numerical solvers and pre/post processing utilities. The code utilises a cell centred polyhedral finite volume method with a collocated grid. The grid type stores fluid dynamic quantities at a single node. Both fluid pressure and velocity are stored at the same point at the cell centres then code applies interpolation schemes to obtain values at the face centres [68]. ParaView is an open-source data visualisation and analysis tool designed to visualise and process large datasets. This is the visualisation tool used in this work for various contour plots.

### 3.2.2 Spatial Discretisation

In order to solve the sets of differential equations, a computer requires them to be in a discretised form. The process of discretisation is referred to as mesh generation and this

involved dividing the continuous fluid domain into discrete points (nodes or vertices) and volumes (cells or elements). There are two types of mesh:

- Structured mesh - These are comprised of hexahedral cells with each mesh point being defined by indices  $i,j,k$ .
- Unstructured mesh - These are created with no point ordering. The elements in this type of mesh can be tetrahedral, hexahedral or any polyhedral shape.

A structured mesh has the advantage over unstructured cells when relating elements to their neighbours and allows data to be more easily transferred. However when introducing a complex geometry, a mesh may need to be dividing irregularly. This may be done in several methods (multiblock, overset mesh) but generally for a complex geometry, an unstructured mesh is used. Unstructured meshes commonly use tetrahedral elements in order to be easily generated around a complex geometry although hexahedral elements are often used in the boundary layer of a geometry, this layer is referred to as an inflation layer in many meshing tools. Unstructured meshes, however, require more mesh data (connectivity, face normals) and this leads to a larger memory requirement on the computer [70].

Discretisation of the domain means that the partial differential equations must also be discretised. This may be done via numerous processes, the main methods being: the finite difference method, the finite volume method and the finite element method. In this work the finite volume method will be utilised to solve the fluid flow.

### 3.2.3 Finite Volume Method for Unsteady Flows

The conservation laws are applied to each cell of a spatially discretised domain to obtain a set of discrete equations. The fluxes are computed using an approximation of the solution on the cell faces, which can be obtained interpolation or reconstruction. The sources and sinks represent external forces or internal production or consumption of the physical quantity being modelled. The resulting set of equations can then be solved using numerical methods such as linear algebraic techniques or non-linear iterative methods. The solution obtained represents an approximation of the original PDE over the discretised domain. One advantage of the FVM is that it is inherently conservative, meaning that the sum of the values of the physical quantity over all cells is conserved over time.

The discretisation process involves the integration of the partial differential equations into the balance equations over the elements in the mesh. Gauss theorem is applied to the volume integrals of the convection and diffusions terms into surface integrals. The conservation equation for the general scalar variable  $\phi$  can be expressed as

$$\frac{\partial(\rho\phi)}{\partial t} + \nabla \cdot (\rho\mathbf{u}\phi) = \nabla \cdot (\Gamma^\phi \nabla \phi) + Q^\phi. \quad (3.27)$$

The following is then obtained by integrating equation (3.27) over the cell volume  $V_c$ ,

$$\int_{V_c} \frac{\partial(\rho\phi)}{\partial t} dV + \int_{V_c} \nabla \cdot (\rho\mathbf{u}\phi) dV = \int_{V_c} \nabla \cdot (\Gamma^\phi \nabla \phi) dV + \int_{V_c} Q^\phi dV. \quad (3.28)$$

We now replace the volume integrals of convection and diffusion by surface integrals through the use of the divergence theorem. The constant source term and the transient term do not vary in space for a given time so can be written as follows

$$\frac{\partial(\rho\phi)}{\partial t} \Delta V + \oint_{\partial V_c} (\rho\mathbf{u}\phi) \cdot d\mathbf{S} = \oint_{\partial V_c} (\Gamma^\phi \nabla \phi) \cdot d\mathbf{S} + Q^\phi \Delta V, \quad (3.29)$$

where  $\mathbf{S}$  is a surface vector,  $\mathbf{u}$  is the velocity vector and  $\phi$  is the conserved quantity and  $V_c$  is the element volume. The time discretisation for these terms must also be taken into consideration in an unsteady flow. Therefore an integration in time is carried out as follows

$$\int_t^{t+\Delta t} \frac{\partial(\rho\phi)}{\partial t} \Delta V dt + \int_t^{t+\Delta t} \oint_{\partial V_c} (\rho\mathbf{u}\phi) \cdot d\mathbf{S} dt = \int_t^{t+\Delta t} \oint_{\partial V_c} (\Gamma^\phi \nabla \phi) \cdot d\mathbf{S} dt + \int_t^{t+\Delta t} Q^\phi \Delta V dt. \quad (3.30)$$

There are many methods in which the time integration and spatial integration can be carried out.

### 3.2.4 Numerical Schemes

Numerical discretisation schemes are fundamental techniques used in computational fluid dynamics (CFD) to approximate and solve the governing equations of fluid flow. These schemes play a crucial role in converting continuous equations into discrete equations that can be solved numerically on a computer [71].

Time integration schemes, i.e.  $\frac{\partial}{\partial t}$ , are used to discretize the time domain in CFD simulations. They determine how the flow variables evolve over time. Gradient schemes, i.e.  $\nabla\phi$ , are employed to discretise the gradient term in the governing equations, which represents the spatial variation of a quantity. These schemes approximate the gradients of flow variables, such as velocity and pressure, at various locations in the computational domain. Divergence schemes, i.e.  $\nabla \cdot (\rho\mathbf{u})\phi$ , are employed to discretize the divergence term in the governing equations, such as the continuity equation and the conservation of momentum equations. They calculate the rate of change of a quantity with respect to space.

Scheme Type	Scheme Choice	Description
Time Scheme	Forward Euler	First order, bounded, implicit.
Gradient Scheme	Gauss Linear	Second order, Gaussian integration with a linear interpolation scheme.
Divergence Scheme ( $\nabla \cdot (\phi\mathbf{u})$ )	Bounded Gauss Linear Upwind	Second order, bounded with limited linear interpolation scheme.
Divergence Scheme (other)	Bounded Gauss limited Linear	Second order, bounded with linear upwind interpolation scheme.

Table 3.2: Selected discretisation methods utilised in the fluid simulations conducted in this study.

In the context of numerical methods, "First order" refers to the level of accuracy or precision in approximating a solution or calculating a derivative. It means that the method achieves accuracy up to the first order of magnitude or error. "Gauss" refers to the Gauss theorem, which is used to calculate the gradients at the cell faces. The scheme calculates the gradients by taking into account the values at neighbouring cell centres, following the Gauss theorem-based approach. The term "bounded" implies that the scheme incorporates a limiting mechanism to prevent excessive steep gradients or abrupt changes in the solution. This is important to avoid numerical instabilities that can arise when dealing with highly non-linear or discontinuous flows. The term "limited" indicates that the scheme applies a limiting function to restrict the calculated gradients. This limiting function helps to maintain a smooth and well-behaved solution by preventing sharp changes or excessive amplification of gradients. An "implicit" scheme refers to a type of time integration scheme where the solution at a future time step is obtained by solving a system of equations that includes both the current and future values. In an implicit scheme, the equations are typically non-linear, and an iterative method is used to solve them. Unlike explicit schemes, where the future solution is calculated explicitly in terms of the current solution, implicit schemes involve solving a set of equations that cannot be

directly solved for the future values. Instead, the equations are usually solved iteratively until convergence is achieved. In an "upwind" scheme, the values at the cell faces are computed by considering the direction of the flow. It uses a weighted average of neighbouring cell values, giving more weight to the values that are upstream or upwind of the flow. This approach ensures that the information flows in the correct direction and minimizes numerical oscillations or spurious solutions that may occur when using central differencing schemes [72].

### 3.2.5 Indicators of Discretisation Quality

In this work numerous methods and software were used in order to mesh the complex geometries present. Open-source options were explored using OpenFOAM's snappyHexMesh utility as well as Salome's NETGEN mesh utility. It was found that snappyHexMesh could not accurately construct the geometry as hexahedral meshes were used and the geometry was too complex for the 'snap' method. The 'snap' involved having a background structured mesh then cutting the cells around a geometry until the mesh creates the geometry.

The NETGEN algorithm worked better in this aspect of meshing due to the fact that tetrahedral cells were used. However, many of the mesh quality parameters did not meet a sufficient standard to obtain an accurate solution for the fluid simulation. Orthogonality was one of these parameters that the NETGEN algorithm failed to optimise. Further mesh parameters are described in a later subsection.

A meshing technique was needed to address the issues discussed above, therefore the meshing of the 3D problem was carried out via a software called ANSYS. ANSYS is a widely used software for engineering simulation and analysis providing tools for simulating the behaviour of various physical phenomena. ANSYS DesignModeler meshing will be used for the meshing of all 3D simulations in this project. The mesh will then be converted to a mesh readable for OpenFOAM. There are several important mesh parameters to getting accurate CFD results. ANSYS has a powerful meshing tool and was able to produce high quality mesh that fit the geometry of the domain accurately.

#### Near Wall Meshing

Due to the no slip condition there is a steep velocity gradient close the wall. Therefore, to accurately resolve this gradient a fine mesh is required.  $y^+$  is a non-dimensionalised normal distance from the nearest boundary to the cell centroid. Velocity on the viscous sublayer is



not greatly affected by the bulk flow velocity so the velocity in this layer must be alternatively calculated [68]. In OpenFOAM the  $y^+$  value is calculated in the  $k-\omega$  SST turbulence model as follows

$$y^+ = \rho y \frac{\sqrt{C_\mu^{1/2} k}}{\mu}. \quad (3.31)$$

The parameter,  $y^+$ , is important in CFD simulations because it affects the accuracy of the near-wall flow predictions, which are crucial in many engineering applications, such as aerodynamics, heat transfer, and combustion. If the first computational cell is too far from the wall (i.e.,  $y^+$  is too large), the flow behaviour near the wall will not be accurately captured, and the simulation results may be unreliable. On the other hand, if the first computational cell is too close to the wall (i.e.,  $y^+$  is too small), the computation may become unstable, and the solution may be affected by numerical errors.

To determine an appropriate  $y^+$  value for a given simulation, various criteria are used, depending on the turbulence model and the specific application. In general, it is desirable to have  $y^+$  values that are in the range of 1-5 for non-wall-function-based turbulence models and 30- 200 for wall-function-based turbulence models [69, 73].

To achieve a desired  $y^+$  value, the near-wall mesh is typically refined or stretched in the direction perpendicular to the wall. This can be done manually or automatically using specialised mesh-generation tools. Careful consideration of  $y^+$  values is necessary to ensure accurate and reliable CFD simulations, especially in regions with complex flow patterns and high turbulence intensity.

### Non-orthogonality

In CFD, "orthogonality" refers to the angle between two intersecting faces of a computational cell. A perfectly orthogonal face has a 90 degree angle with its neighbour, while a non-orthogonal face has an angle that deviates from 90 degrees. Non-orthogonality angle is defined as the angle between the cell centroid vector and the unit normal vector as defined in Figure 3.1a. However, it can be seen in 3.1b, this angle can appear to be smaller for some orientations so the angle is taken between the vector connecting the face centre to cell centre and the face normal vector. Both values are then taken and substituted into (3.32) and the maximum angle is used for non-orthogonality.

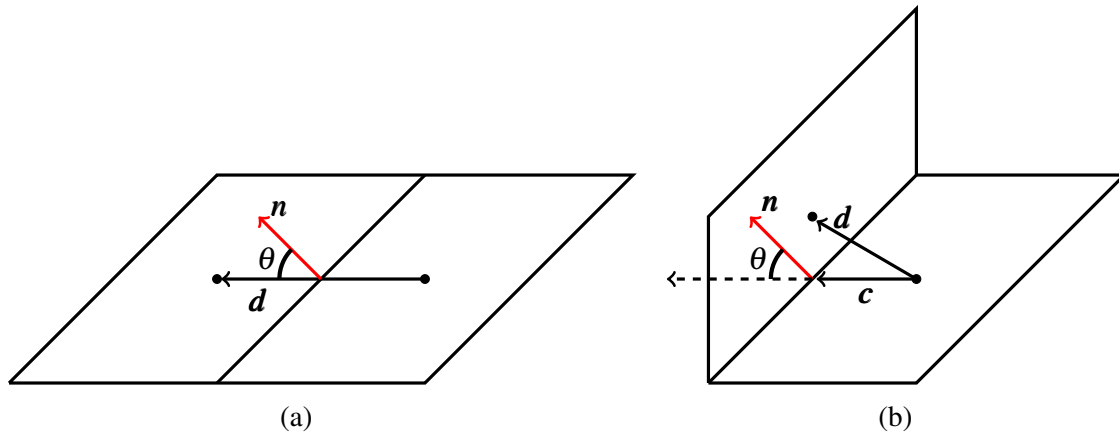


Figure 3.1: (a) Diagram to aid the descriptive definition of non orthogonality using surface normal at the common face centre and the vector connecting cell centroids. (b) Diagram to aid non orthogonality definition using surface normal at the common face centre and the vector connecting cell centroid to face centre.

The method of calculating non-orthogonality is as follows,

$$\theta = \max \left[ \cos^{-1} \left( \frac{\mathbf{d} \cdot \mathbf{n}}{|\mathbf{d}| |\mathbf{n}|} \right), \cos^{-1} \left( \frac{\mathbf{c} \cdot \mathbf{n}}{|\mathbf{c}| |\mathbf{n}|} \right) \right]. \quad (3.32)$$

The non-orthogonality of a face in CFD can lead to numerical errors in the simulation, particularly in regions of high gradient or near walls. This is because the discretised equations that are used to model fluid flow are based on approximations of the fluxes and gradients of the flow variables across the cell faces, and these approximations become less accurate as the angle between the faces deviates from 90 degrees.

Various methods are used to improve the orthogonality of the computational mesh, including mesh smoothing, mesh adaptation, and the use of special numerical schemes that can handle non-orthogonal grids. This project includes to use of non-orthogonal correctors to overcome some cells with may be highly non-orthogonal.

### Skewness

Skewness is one of the primary quality measures for a mesh. Skewness determines how close to ideal (i.e., equilateral or equiangular) a cell is. The skewness for each face is calculated as the distance from the face centre to the cell centroid to the centre of the face intersection point normalised by the distance from the cell centroid to the adjacent cell.

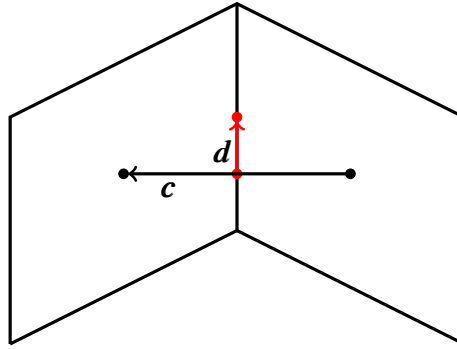


Figure 3.2: Diagram to aid non orthogonality definition using surface normal at the common face centre and the vector connecting cell centroid to face centre.

The skewness is defined as

$$\sigma_{Skewness} = \frac{\|\mathbf{d}\|}{\|\mathbf{c}\|}, \quad (3.33)$$

where  $\mathbf{d}$  and  $\mathbf{c}$  are found in 3.2. A skewness below 4 is desirable for faces on the internal element and below 20 for boundary elements. High skewness values can lead to numerical errors in CFD simulations, particularly in regions of high gradient or near walls. Therefore, it is often desirable to have cells with low skewness factors in order to improve the accuracy and stability of the simulation.

### Courant Number (CFL)

In fluid dynamics, the CFL (Courant-Friedrichs-Lewy) number is a dimensionless quantity used to estimate the accuracy and stability of numerical solutions to partial differential equations describing fluid flow. The CFL number is named after Richard Courant, Kurt Friedrichs, and Hans Lewy, who developed the concept in 1928.

The CFL number is defined as the product of the time step and the maximum wave speed in the system, divided by the characteristic length scale of the system. Mathematically, the CFL number is expressed as:

$$C_o = \frac{\Delta t}{2V_c} \sum_f (\mathbf{u}_f \cdot |\mathbf{n}_f|) A_f. \quad (3.34)$$

The CFL number is used to determine the maximum time step that can be used in a numerical simulation to ensure that the solution remains stable and accurate. If the time step is too large, the solution can become unstable and may exhibit numerical oscillations or blow up. Therefore, the CFL number is an important parameter to consider when simulating fluid flow using numerical methods. A CFL number below 1 is required for the stability of the simulation.

Ensuring a suitable CFL number is an iterative process for a given mesh the time step of the simulation can be reduced to achieve a sufficiently small CFL to run a stable simulation.

### 3.3 Conclusions

This chapter has delved into the mathematical description of fluid mechanics, exploring various crucial aspects that form the foundation of this field. The chapter began by examining the key components of fluid mechanics, from conservation laws to constitutive laws, turbulence, physical boundary conditions, relevant parameters, and wall functions. These elements provide the fundamental principles necessary for understanding and analysing fluid behaviour.

Furthermore, the chapter explored computational fluid dynamics (CFD), a powerful tool for simulating and predicting fluid flow phenomena. The exploration of CFD encompassed software tools, discretisation techniques, the finite volume method for unsteady flows, numerical schemes, and meshing strategies, all of which play vital roles in the numerical simulation of fluid behaviour. In conclusion, the groundwork laid in this section serves as a solid foundation for our further exploration of fluid mechanics and its practical applications.

# Chapter 4

## Structural Mechanics Computational Modelling

This chapter focuses on the theory of structural mechanics, describing the conservation laws in strong and weak form, and introducing the finite element method for frequency modal analysis. In this chapter, a mathematical description of structural mechanics, including continuum mechanics, modal frequency analysis, software, finite element analysis, and fluid to solid mapping will be provided.

The chapter begins by introducing the basic concepts of continuum mechanics, including stress, strain, and the equations of motion. The chapter will proceed to discuss modal frequency analysis, which is a technique used to determine the natural frequencies and mode shapes of structures. Next, an overview of software commonly used in solid mechanics, will be presented with a focus on finite element analysis, which is a numerical technique used to solve problems in solid mechanics. The chapter will finish by discussing fluid to solid mapping, which is the process of transferring data from a fluid simulation to a solid simulation. This is an important technique for simulating the interaction between fluids and solid structures.

### 4.1 Aspects of Solid Mechanics

#### 4.1.1 Continuum Mechanics

Let  $\Omega \subset \mathbb{R}^3$  be a domain occupied by a continuum during a time interval of 0 to  $T$  with the boundary  $\partial\Omega$ . The boundary  $\partial\Omega$  consists of Neumann  $\partial\Omega^N$  and Dirichlet  $\partial\Omega^D$  boundary

regions and has an outward normal  $\mathbf{n}$  as shown in Figure 4.1. For small deformations, a

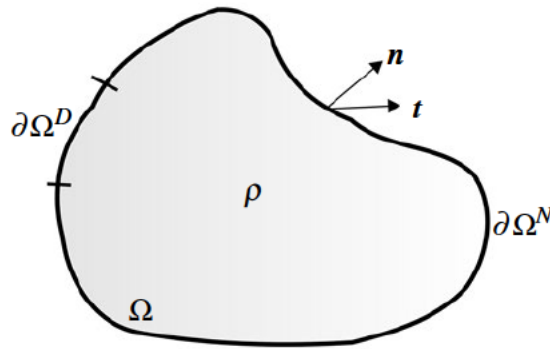


Figure 4.1: 3D set up for flow around a cylinder for a straight cylinder with labelled boundaries.

displacement field can be defined as  $\mathbf{u}(\mathbf{x}, t) : \Omega \times [0, T]$  where  $\mathbf{x} \in \Omega$  represents a point inside the material at a time within the period of simulation. The conservation of linear momentum will be used in order to develop a modal superposition model. Consider the solid domain illustrated in Figure 4.1. Here, the domain ( $\Omega$ ) can be seen with the surfaces tractions ( $\mathbf{t}$ ) are applied to a boundary of the domain ( $\partial\Omega^N$ ). In this case the surface tractions arise from the fluid domain then are mapped onto the solid domain. No body forces can be seen here and they are not considered. The conservation of momentum is used:

$$\int_{\partial\Omega^N} \mathbf{t} dA = \int_{\Omega} \rho \ddot{\mathbf{u}} dV, \quad (4.1)$$

where  $\ddot{\mathbf{u}}$  is acceleration. When (4.1) is solved the solution is a displacement fulfilling Dirichlet and Neumann boundary conditions. Given that  $\mathbf{t} = \boldsymbol{\sigma} \mathbf{n}$  where  $\boldsymbol{\sigma}$  is the Cauchy stress tensor, following can be derived,

$$\int_{\partial\Omega^N} \boldsymbol{\sigma} \mathbf{n} dA - \int_{\Omega} \rho \ddot{\mathbf{u}} dV = \mathbf{0}, \quad (4.2)$$

Applying Gauss' theorem to (4.2), all terms can be grouped into a volume integral and the following can be derived,

$$\int_{\Omega} (\nabla \cdot \boldsymbol{\sigma} - \rho \ddot{\mathbf{u}}) dV = \mathbf{0}. \quad (4.3)$$

The strong form of the problem, that is its physical description, can be described as follows:

$$\nabla \cdot \boldsymbol{\sigma} - \rho \ddot{\mathbf{u}} = \mathbf{0} \quad \text{in } \Omega \times [0, T] \quad (4.4a)$$

$$\boldsymbol{\sigma} \mathbf{n} = \mathbf{t} \quad \text{on } \partial\Omega^N \times [0, T] \quad (4.4b)$$

$$\mathbf{u} = \mathbf{0} \quad \text{on } \partial\Omega^D \times [0, T] \quad (4.4c)$$

$$\mathbf{u} = \mathbf{0} \quad \text{in } \Omega \times 0 \quad (4.4d)$$

$$\dot{\mathbf{u}} = \mathbf{0} \quad \text{in } \Omega \times 0. \quad (4.4e)$$

Equation (4.4a) enforces the conservation of mass of the domain volume, (4.4b) represents a force acting on the Neumann boundary and (4.4c) describes the fixing of the Dirichlet boundary which becomes important when defining a domain as a cantilever. Both (4.4d) and (4.4e) describe the initial conditions of the problem, setting the initial displacement and velocity to zero for the whole domain.

These equations will be solved in this research using the Finite Element method which requires the strong form to be transformed into its weak form counterpart. This is achieved via the principle of virtual work. To apply the principle of virtual work, the potential energy resulting from the residual force and a virtual displacement ( $\delta \mathbf{u}$ ) is integrated throughout the entire domain. The principle dictates that the total value of this integrated potential energy should equal zero.

By ensuring that the integrated potential energy due to the residual force and virtual displacement is balanced, the principle of virtual work ensures that the system remains in a state of equilibrium. It provides a basis for understanding and analysing the relationship between internal forces and external loads within a structure or mechanical system. The weak form can typically be written as

$$\int_{\Omega} (\nabla \delta \mathbf{u} : \boldsymbol{\sigma} + \delta \mathbf{u} \cdot \rho \ddot{\mathbf{u}}) dV = \int_{\partial\Omega^N} \delta \mathbf{u} \cdot \mathbf{t} dA \quad \forall \delta \mathbf{u}. \quad (4.5)$$

It must be noted that  $\delta \mathbf{u} = \mathbf{0}$  at a Dirichlet boundary ( $\partial\Omega^D$ ). The solution to this problem will attempt to capture smaller displacements of a thermowell as larger displacements only arise due to resonance which in turn will lead to failure of the thermowell. A large displacement due to the steady state component of the flow force would be covered insufficiently by the current industry standards. With small displacements and therefore small strains, a linear approach to

strain is sufficient. The following is used:

$$\boldsymbol{\varepsilon} = \frac{1}{2}(\nabla \mathbf{u} + (\nabla \mathbf{u})^\top) \quad \text{in } \Omega \times [0, T]. \quad (4.6)$$

This definition produces a symmetrical strain tensor and moving forward the Voigt notation is adopted where  $\tilde{\boldsymbol{\varepsilon}} = [\varepsilon_{11}, \varepsilon_{22}, \varepsilon_{33}, 2\varepsilon_{12}, 2\varepsilon_{13}, 2\varepsilon_{23}]^\top$ ,  $\tilde{\boldsymbol{\sigma}} = [\sigma_{11}, \sigma_{22}, \sigma_{33}, \sigma_{12}, \sigma_{13}, \sigma_{23}]^\top$  and  $\tilde{\boldsymbol{\delta u}} = [u_{11}, u_{22}, u_{33}, u_{12}, u_{13}, u_{23}]^\top$ . This leads to the constitutive laws written as

$$\tilde{\boldsymbol{\sigma}} = \tilde{\mathbf{D}} \tilde{\boldsymbol{\varepsilon}}, \quad (4.7)$$

in which  $\tilde{\mathbf{D}}$  is the isotropic stiffness matrix and takes the form:

$$\tilde{\mathbf{D}} = \frac{E}{(1+\nu)(1-2\nu)} \begin{bmatrix} 1-\nu & \nu & \nu & 0 & 0 & 0 \\ \nu & 1-\nu & \nu & 0 & 0 & 0 \\ \nu & \nu & 1-\nu & 0 & 0 & 0 \\ 0 & 0 & 0 & 1-2\nu & 0 & 0 \\ 0 & 0 & 0 & 0 & 1-2\nu & 0 \\ 0 & 0 & 0 & 0 & 0 & 1-2\nu \end{bmatrix}, \quad (4.8)$$

where  $E$ , and  $\nu$  are the Young's modulus and Poisson's ratio respectively. The final weak form can be written with Voigt notation as follows

$$0 = \int_{\Omega} (\delta \tilde{\boldsymbol{\varepsilon}} \cdot \tilde{\mathbf{D}} \tilde{\boldsymbol{\varepsilon}} + \delta \mathbf{u} \cdot \rho \ddot{\mathbf{u}}) dV - \int_{\partial \Omega^N} \delta \mathbf{u} \cdot \mathbf{t} dA \quad \forall \delta \mathbf{u}. \quad (4.9)$$

To discretise the equation and solve the problem computationally, the Galerkin method is employed. This method involves two key steps.

Firstly, shape functions are introduced to determine the contribution of each discrete independent variable to any location within an element. These variables are resolved at one of the  $k$  nodes that form the element. The shape functions facilitate the conversion of continuous variables to discrete variables, allowing for their representation within the computational framework.

Secondly, the volume and surface integrals of the (4.5) are transformed to calculate the virtual work done. This is achieved by computing the integral over each element and then



summing the contributions over all elements in the domain or all element faces on the domain surface.

The discretisation process extends to the variables involved in the equation. The displacements, accelerations, and virtual displacements are all discretised. This involves representing these variables as discrete quantities, typically associated with specific nodes or locations within the computational domain.

By discretising the equation and variables, the problem can be solved computationally, enabling numerical simulations and analysis. The Galerkin method, with its introduction of shape functions and conversion of integrals, facilitates the transition from the continuous formulation to a discrete computational framework. The variables are defined as follows

$$\mathbf{u} = \mathbf{N}\mathbf{u} \quad (4.10a)$$

$$\dot{\mathbf{u}} = \mathbf{N}\dot{\mathbf{u}} \quad (4.10b)$$

$$\ddot{\mathbf{u}} = \mathbf{N}\ddot{\mathbf{u}} \quad (4.10c)$$

$$\delta\mathbf{u} = \mathbf{N}\delta\mathbf{u}. \quad (4.10d)$$

The shape function matrix ( $\mathbf{N}$ ) then takes the form:

$$\mathbf{N} = \begin{bmatrix} N_1 & 0 & 0 & N_2 & 0 & 0 & & N_k & 0 & 0 \\ 0 & N_1 & 0 & 0 & N_2 & 0 & \dots & 0 & N_k & 0 \\ 0 & 0 & N_1 & 0 & 0 & N_2 & & 0 & 0 & N_k \end{bmatrix}, \quad (4.11)$$

where  $k$  is the number of nodes in an element. The strain and virtual strains are then discretised by:

$$\tilde{\boldsymbol{\epsilon}} = \mathbf{B}\mathbf{u} \quad (4.12a)$$

$$\delta\tilde{\boldsymbol{\epsilon}} = \mathbf{B}\delta\mathbf{u}, \quad (4.12b)$$

where  $\mathbf{B}$  is the spatial derivative of  $\mathbf{N}$ . There are three contributions to work in (4.9) that must be summed over all elements in the domain. The contributions due to internal work, inertial forces and external forces are seen as

$$0 = \sum_{e=1}^n \int_{\Omega_e} (\delta\mathbf{u}^T \mathbf{N}^T \rho \mathbf{N} \ddot{\mathbf{u}} + \delta\mathbf{u}^T \mathbf{B}^T \tilde{\mathbf{D}} \mathbf{B} \mathbf{u}) dV - \sum_{e=1}^s \int_{\Omega_e^N} \delta\mathbf{u}^T \mathbf{N}^T \mathbf{t} dA. \quad (4.13)$$

Grouping each term in (4.13), the equation can be written as

$$0 = \delta \mathbf{u}^T \left[ \left( \sum_{e=1}^n \int_{\Omega_e} \mathbf{N}^T \rho \mathbf{N} dV \right) \ddot{\mathbf{u}} + \left( \sum_{e=1}^n \int_{\Omega_e} \mathbf{B}^T \tilde{\mathbf{D}} \mathbf{B} dV \right) \mathbf{u} - \left( \sum_{e=1}^s \int_{\Omega_e^N} \mathbf{N}^T \mathbf{t} dA \right) \right]. \quad (4.14)$$

From (4.14), each term can now be grouped into matrices giving the dynamic equation defined as

$$\mathbf{0} = \mathbf{M} \ddot{\mathbf{u}} + \mathbf{K} \mathbf{u} - \mathbf{F}, \quad (4.15)$$

where  $\mathbf{M}$  is the mass matrix,  $\mathbf{K}$  is the stiffness matrix and  $\mathbf{F}$  are the applied external forces. Note that this equation is the undamped dynamic equation. In this project the applied external forces will be generated and mapped from the fluid simulation domain. When a system is damped the following is true:

$$\mathbf{0} = \mathbf{M} \ddot{\mathbf{u}} + \mathbf{C} \dot{\mathbf{u}} + \mathbf{K} \mathbf{u} - \mathbf{F}, \quad (4.16)$$

where  $\mathbf{C}$  is the damping matrix.

In this study, Rayleigh damping, as described by Rayleigh in [74], is employed. Rayleigh damping provides a simplified approach to model damping by assuming that the damping force is proportional to the instantaneous velocities and displacements of the system. The damping matrix in the equations of motion is expressed as a linear combination of the mass matrix and the stiffness matrix as follows:

$$\mathbf{C} = \alpha \mathbf{M} + \beta \mathbf{K}, \quad (4.17)$$

where  $\alpha$  and  $\beta$  are the Rayleigh damping coefficients. These coefficients determine the proportionality between the damping force and the system velocities and displacements. By incorporating damping in this way, the system's characteristics are preserved, and it remains possible to decouple the equations of motion [75].  $\alpha$  is the mass proportional damping coefficient. The term  $\alpha \mathbf{M}$  represents the mass proportional damping in the system. This type of damping is proportional to the mass matrix  $\mathbf{M}$  and is velocity-dependent. The coefficient  $\alpha$  determines the level of mass proportional damping.  $\beta$  is the stiffness proportional damping coefficient. The term  $\beta \mathbf{K}$  represents the stiffness proportional damping in the system. This type of damping is proportional to the stiffness matrix  $\mathbf{K}$  and is displacement-dependent. The coefficient  $\beta$  determines the level of stiffness proportional damping. The values of  $\alpha$  and  $\beta$  are crucial in determining the damping characteristics of the system. The choice of these coefficients influences the rate at which energy is dissipated in the system, impacting the

dynamic response to external forces or excitations. Engineers often tune these coefficients to achieve desired levels of damping in specific modes or frequency ranges though this will not be carried out in this work. The decoupling of the damping matrix as well as the mass and stiffness matrix allows for modal frequency analysis [76].

The adoption of Rayleigh damping ensures that the damped equations of motion can still be solved using modal analysis. This approach allows for the determination of the system's natural frequencies, mode shapes, and response characteristics in the presence of damping. Modal analysis is introduced in the section 4.3.

By incorporating Rayleigh damping and utilising modal analysis, the effects of damping on the system's behaviour can be effectively accounted for. This approach allows for a comprehensive understanding of the system's response to dynamic loads and facilitates the design and optimisation of structures subjected to dynamic conditions.

## 4.2 Boundary Load Transfer

To fulfil the boundary condition shown in (4.4b), the mapping for forces from the fluid domain boundary onto the solid boundary is required.

In this work the mapping method that will be implemented is the Nearest Point Interpolation Mapping (NPIM). NPIM is a type of interpolation method used in numerical analysis to map a given set of points from one coordinate system to another. The principle behind NPIM is to find the nearest point in the target coordinate system for each point in the source coordinate system and assign the value of that point to the source point. As shown in Figure 4.2, the face centres of the solid boundary inherit the traction force from the nearest face centres of the fluid boundary.

In other words, NPIM works by taking a set of discrete data points in one coordinate system and mapping them onto another coordinate system by finding the nearest point in the target system for each point in the source system. Once the nearest point is found, the value of the point in the target system is assigned to the corresponding point in the source system.

NPIM is commonly used in scientific simulations and modelling to interpolate data from a set of discrete measurements to a continuous function, such as in fluid dynamics or heat transfer.

One of the key advantages of NPIM is its simplicity and computational efficiency. The method requires minimal computation, as it only involves finding the nearest point for each source point, which can be done using a search algorithm such as a kd-tree or a binary search. NPIM is also easy to implement and can be used for both 2D and 3D data. However, a major

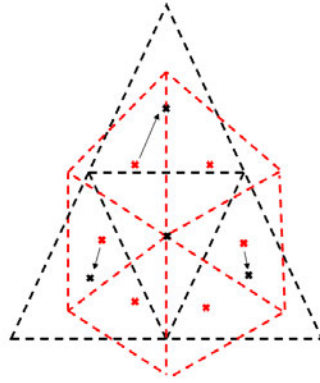


Figure 4.2: Illustration of how NPIM is implemented in 2D. Where the red dashed lines (---) represent the fluid boundary edges and the black dashed lines (---) represent the solid boundary edges. The corresponding crosses represent the face centres.

limitation of NPIM is its susceptibility to aliasing. Because the method only considers the nearest point, it may not accurately capture the underlying continuous function, particularly in regions where steep spatial gradients are encountered. This can lead to errors and artefacts in the interpolated data. To mitigate these issues, other interpolation methods such as bilinear or cubic interpolation can be used, but at the cost of increased computation and complexity. However, it is found that in this case of the flow past a cylinder, steep gradients of this type is not found. In subsection 5.2.2, this is the focus of the convergence study of load transmission to ensure that a simple mapping algorithm can be used without detrimental loss of information.

### 4.2.1 Newmark-beta Time Integration

The Newmark-beta method is a numerical integration scheme used for solving dynamic structural analysis problems. It is commonly employed in the field of structural engineering and finite element analysis to simulate the time-dependent behaviour of structures subjected to dynamic loads [77]. The Newmark-beta method is widely used due to its stability, accuracy, and ability to handle a wide range of dynamic problems. It allows for efficient and reliable analysis of structures subjected to time-varying loads. It is used in this work to benchmark against the reduced order model.

The Newmark-beta method is an implicit time integration scheme that provides a stable and accurate solution for the dynamic response of structures. It is a second-order accurate method, meaning that it approximates the solution with a truncation error that is proportional to the square of the time step size. The method is based on the concept of central difference approximation, where the acceleration is approximated by differencing the velocities at two adjacent time steps. The Newmark-beta method introduces two parameters,  $\beta$  and  $\gamma$ , which control the numerical dissipation and numerical dispersion properties of the scheme. The displacement, velocity, and acceleration at each time step are updated iteratively using the following equation steps:

$$\begin{aligned}\ddot{\mathbf{U}}_{predictor} &= \ddot{\mathbf{U}}(t) \\ \dot{\mathbf{U}}_{predictor} &= \dot{\mathbf{U}}(t) + [(1 - \gamma) \ddot{\mathbf{U}}(t) + \gamma \ddot{\mathbf{U}}_{predictor}] \Delta t \\ \mathbf{U}_{predictor} &= \mathbf{U}(t) + \dot{\mathbf{U}} \Delta t + \left[ \left( \frac{1}{2} - \beta \right) \ddot{\mathbf{U}}(t) + \beta \ddot{\mathbf{U}}_{predictor} \right] \Delta t^2 \\ \hat{\mathbf{M}} &= \mathbf{M} + \mathbf{C} \gamma \Delta t + \mathbf{K} \beta \Delta t^2 \\ \hat{\mathbf{F}} &= \mathbf{F}(t + \Delta t) - (\mathbf{M} \ddot{\mathbf{U}}_{predictor} + \mathbf{C} \dot{\mathbf{U}}_{predictor} + \mathbf{K} \mathbf{U}_{predictor}) \\ \hat{\mathbf{a}} &= \hat{\mathbf{M}}^{-1} \hat{\mathbf{F}} \\ \ddot{\mathbf{U}}(t + \Delta t) &= \ddot{\mathbf{U}}(t) + \hat{\mathbf{a}} \\ \dot{\mathbf{U}}(t + \Delta t) &= \dot{\mathbf{U}}(t) + \hat{\mathbf{a}} \gamma \Delta t \\ \mathbf{U}(t + \Delta t) &= \mathbf{U}(t) + \hat{\mathbf{a}} \beta \Delta t^2.\end{aligned}$$

The parameters  $\beta$  and  $\gamma$  determine the stability and accuracy of the method. Commonly used values are  $\beta = 0.25$  and  $\gamma = 0.5$ , which result in the average acceleration method. This is the method used in this work. Different combinations of  $\beta$  and  $\gamma$  can be selected based on the desired numerical characteristics of the simulation [78].

### 4.3 Reduced Order Model

To model displacement of the cylindrical geometry placed in a flow the force on the surface of the cylinder will be mapped from the fluid mesh to a solid mesh using NPIM. The force will be input into a frequency response modal analysis calculation to find the displacement. Frequency response modal analysis is a technique used in mechanical engineering to study the

dynamic behaviour of structures or mechanical systems under varying frequencies of excitation. Frequency response modal analysis is used to determine the dynamic behaviour of the structure under excitation at set frequencies. The modal parameters of a system are important because they provide insights into the system's behaviour. The model will be used to determine the natural frequencies and mode shapes initially, then the response under dynamic loading. The accuracy of these response estimates depend on several factors, such as the quality of the input load data and will therefore depend on the quality of upstream processes used to determine the load (flow model, load mapping). In general, frequency response modal analysis provides a good approximation of the displacement response over a range of frequencies near the natural frequencies of the system. This is done in this work as it is computationally cheap and in comparison to a time integrator.

A reduced order model is proposed using modal frequency response analysis. The undamped dynamic equation (4.16) with no excitation ( $\mathbf{F} = \mathbf{0}$ ) is used to obtain the mode shapes of the structural system. This is done by rearranging (4.16) to form an eigenvalue problem as follows:

$$(\mathbf{K} - \lambda_I \mathbf{M}) \Phi_I = \mathbf{0}, \tag{4.19}$$

where  $\lambda_I$  are the eigenvalues and  $\Phi_I$  are the modal shape vector for mode  $I$ . It is important to note  $\lambda_I = \omega_I^2$  where  $\omega_I$  is the natural frequency of mode  $I$ . Mode shapes, also known as eigenmodes or eigenvectors, are fundamental patterns of vibration or oscillation exhibited by a dynamic system. They describe the spatial distribution and relative amplitudes of motion of different parts of the system when it vibrates or oscillates at a particular frequency. In the context of structural dynamics, mode shapes represent the different patterns of deformation that a structure can undergo when subjected to vibrational forces. Each mode shape corresponds to a specific natural frequency of the structure, which is the frequency at which it naturally tends to vibrate without any external excitation. Displacement can be decomposed and can be defined as a summation of mode shapes multiplied by modal displacements as follows

$$\mathbf{u}(t) = \Phi \phi(t) = \sum_{I=1}^{modes} \Phi_I q_I(t), \tag{4.20}$$

where  $q_I$  is the modal displacement for that mode. The dynamic equation can then be written as follows with the force matrix unchanged from after mapping and projected onto the mode

shapes,

$$\Phi^T \mathbf{M} \Phi \ddot{\mathbf{q}}(t) + \Phi^T \mathbf{C} \Phi \dot{\mathbf{q}}(t) + \Phi^T \mathbf{K} \Phi \mathbf{q}(t) = \Phi^T \mathbf{F}(t). \quad (4.21)$$

This produces a linear uncoupling of the mass, stiffness and damping matrices due to the orthogonality to the mode shapes. Therefore the modal dynamic equation can then be written as

$$\mathbf{M}_\phi \ddot{\mathbf{q}}(t) + \mathbf{C}_\phi \dot{\mathbf{q}}(t) + \mathbf{K}_\phi \mathbf{q}(t) = \mathbf{T}(t), \quad (4.22)$$

where  $\mathbf{M}_\phi$ ,  $\mathbf{C}_\phi$ ,  $\mathbf{K}_\phi$  are diagonal matrices containing modal masses, damping coefficients and stiffness, respectively. The dimensions of these matrices are  $[\text{modes} \times \text{modes}]$ . In this work the force will be discretised in time due to the sampling of the force vector field at discrete time steps.  $\mathbf{T}$  is the discretised modal force varying with time structured as follows

$$\mathbf{T} = \begin{bmatrix} T_{11} & T_{12} & T_{13} & \dots & T_{1N_t} \\ T_{21} & T_{22} & T_{23} & \dots & T_{2N_t} \\ \vdots & \vdots & \vdots & \ddots & \vdots \\ T_{N_m 1} & T_{N_m 2} & T_{N_m 3} & \dots & T_{N_m N_t} \end{bmatrix} \quad (4.23)$$

where  $N_m$  is the number of modes and  $N_t$  is the number of time steps. As the dynamic equation is now uncoupled, it can be written as follows

$$m_I \ddot{q}_I(t) + c_I \dot{q}_I(t) + k_I q_I(t) = T_I(t) \quad \text{for } I = 1, \dots, N_m. \quad (4.24)$$

To work in the frequency domain the time dependant variables undergo inverse discrete Fourier transforms defined as the following:

$$T_I(t) = \frac{1}{N_t} \sum_{i=1}^{N_t} \xi_I(\omega_i) e^{j\omega_i t} \quad \xi_I \in \mathbb{C} \quad (4.25a)$$

$$q_I(t) = \frac{1}{N_t} \sum_{i=1}^{N_t} X_I(\omega_i) e^{j\omega_i t} \quad X_I \in \mathbb{C} \quad (4.25b)$$

$$\dot{q}_I(t) = \frac{1}{N_t} \sum_{i=1}^{N_t} j\omega_i X_I(\omega_i) e^{j\omega_i t} \quad X_I \in \mathbb{C} \quad (4.25c)$$

$$\ddot{q}_I(t) = \frac{1}{N_t} \sum_{i=1}^{N_t} -\omega_i^2 X_I(\omega_i) e^{j\omega_i t} \quad X_I \in \mathbb{C} \quad (4.25d)$$

, where  $X_I(\omega)$  is the modal displacement dependant of frequency and  $\xi_I(\omega_i)$  is the modal force dependant of frequency. Both of these variables are complex. Since the time dependant modal force is inputted, to obtain the frequency dependent modal force, an FFT is carried out as follows

$$\xi_I(\omega) = \sum_{i=1}^{N_t} T_I(t_i) e^{-j\omega t_i} \quad \text{for } I = 1, \dots, N_m. \quad (4.26)$$

However to reduce computational expense one may reconstruct (4.25a) just using the frequencies deemed important (by amplitude). The importance is determined by the peak height of the FFT. So the modal force  $T_I$  can be defined as

$$T_I(t) = \frac{1}{N_t} \sum_{i=1}^{N_f} \xi_{iI} e^{j\omega_{iI} t} \quad \xi_i \in \mathbb{C}. \quad (4.27)$$

where  $N_f$  is the number of frequencies deemed important for that given mode  $I$ . Substituting relevant variables into (4.24) allows us to derive modal displacement in the frequency domain as

$$X_{Ii} = \frac{\xi_{Ii}}{(k_I + jc_I \omega_{Ii} - m_I \omega_{Ii}^2)}, \quad (4.28)$$

and therefore the nodal displacements can be found using

$$\mathbf{U}(t) = \frac{1}{N_t} \sum_{I=1}^{N_m} \left( \sum_{i=1}^{N_f} \Phi_I X_I(\omega_{iI}) e^{j\omega_{iI}^2 t} \right). \quad (4.29)$$

Note that the accuracy of this method depends on the number of modes solved for and the number of frequencies selected to reconstruct the time varying function. A time integrator, the Newmark-beta scheme, was used as a benchmark to assess the frequency-domain solution proposed above.

### Relevant Parameter - von Mises Stress

Von Mises stress is a critical concept in the field of solid mechanics and structural engineering. It provides a valuable measure of the overall stress experienced by a material or structure, taking into account both the normal and shear stresses that act on it. Von Mises stress is used to simplify this complex stress distribution into a single value that represents the equivalent stress experienced by the material [79]. This equivalent stress is based on the idea that different types of stresses contribute to material failure in a manner that depends on their



magnitudes and the material's properties. By calculating the von Mises stress, one can assess whether a material or structure is likely to fail under a given set of loads. It serves as a critical parameter for designing safe and reliable structures, as it helps in predicting potential failure points and ensuring that the material remains within its elastic limits. Von Mises stress for isotropic materials in 3D is defined by:

$$\boldsymbol{\sigma}' = \boldsymbol{\sigma} - tr(\boldsymbol{\sigma})\mathbf{I} \quad (4.30a)$$

$$\sigma_{vm} = \sqrt{\frac{3}{2} (\boldsymbol{\sigma}' : \boldsymbol{\sigma}')}. \quad (4.30b)$$

This parameter will be used to measure the stress level of the thermowell under the time varying loads of the fluid.

## 4.4 Implementation

The mapping and the reduced order model were built and run using MATLAB. MATLAB is a proprietary software developed and maintained by MathWorks. For this section of the project, the Partial Differential Equation (PDE) toolbox was used to produce the mass and stiffness matrices. The discretised geometries were input into MATLAB and produced on a 3D meshing software called Gmsh. The PDE toolbox was then used to formulate the mass and stiffness matrices. The boundary condition vectors were populated from the MATLAB implementation of the NPIM. MATLAB was used to solve the problem efficiently using equation (4.29) presented in Section 4.3. The Newmark-beta time integration method was also carried out via MATLAB after the mass and stiffness matrices were formulated to benchmark against the frequency solver.

## 4.5 Conclusions

This chapter, delved into the mathematical description of solid mechanics, exploring various aspects that form the foundation of our understanding of the behaviour of materials and structures. The chapter began by discussing the key aspects of solid mechanics, emphasising the importance of continuum mechanics in modelling the continuous nature of materials. The chosen formulation and its implementation are laid out for scrutiny of the boundary conditions.

Mapping, as a crucial concept in solid mechanics, was introduced. This provides a boundary condition by transferring the load data from the fluid to solid and its implementation was laid out. Reduced order models emerged as a powerful tool for simplifying complex systems while retaining essential characteristics. Additionally, the Newmark-beta time integration scheme was presented as proven as a means to benchmarking the frequency domain solver.

In conclusion, this chapter has laid the groundwork for our journey through the world of solid mechanics. The exploration of fundamental mathematical concepts, reduced order modelling techniques, and practical implementation approaches was carried out.

# Chapter 5

## Numerical Results

In this chapter, a comprehensive exploration of numerical results is undertaken. First, the focus lies on benchmarking the fluid model, encompassing both 2D and 3D simulations. Subsequently, the solid solver's benchmarking is discussed. The chapter delves into fluid-structure interaction, considering 3-D fluid model geometries of finite height. Furthermore, an analysis of fluid results and the frequency response of the structures is presented. The chapter leads up to a comprehensive discussion and evaluation of the obtained outputs.

### 5.1 Fluid Model Benchmarking

Within the context of this study, the following sections delve into the critical process of benchmarking the fluid model. This process is instrumental in ensuring the accuracy and reliability of the numerical simulations, allowing for a robust foundation upon which subsequent analyses can be built. The benchmarking effort is divided into two segments: the examination of a 2D fluid model and the evaluation of results obtained from this model. In parallel, a 3D fluid model is also simulated, followed by an assessment of the outcomes derived from it. These benchmarking exercises are pivotal in establishing the credibility and effectiveness of the fluid model employed in this study. In all simulations within this section, the fluid simulations are initially conducted until the drag coefficient stabilises, oscillating around a consistent non-zero value. This ensures that any initial condition effects on the simulation have been eliminated.

### 5.1.1 2D Fluid Model

As seen in literature, a 2D model is suitable for flows of low Reynolds number. Also, a turbulence model is not necessary. A 2D model is used as it is less computationally expensive than running a 3D model and it is seen in the literature that a 2D model captures the flow accurately [18–21].

#### 2D Domain Description and Discretisation

The fluid domain, as depicted in Figure 5.1, encompasses the area in which the fluid flow around the cylinder is simulated. The cylinder itself has a diameter of 0.008 m, with its centre placed on the origin of the coordinate system. To define the boundaries of the fluid domain in a 2D context, a rectangular region is utilised. The rectangle is determined by specifying the coordinates of two opposite corners. In this case, the first point is  $(-0.05, -0.05)$ , denoting the bottom-left corner of the rectangle, while the second point is  $(0.15, 0.05)$ , indicating the top-right corner where the units are in meters. Preliminary simulations were conducted to determine an appropriate domain size where the pressure gradient around the cylinders reached zero at the domain walls. The run maintained a blockage ratio of approximately 8% to ensure that the simulation remained unaffected by blockage effects.

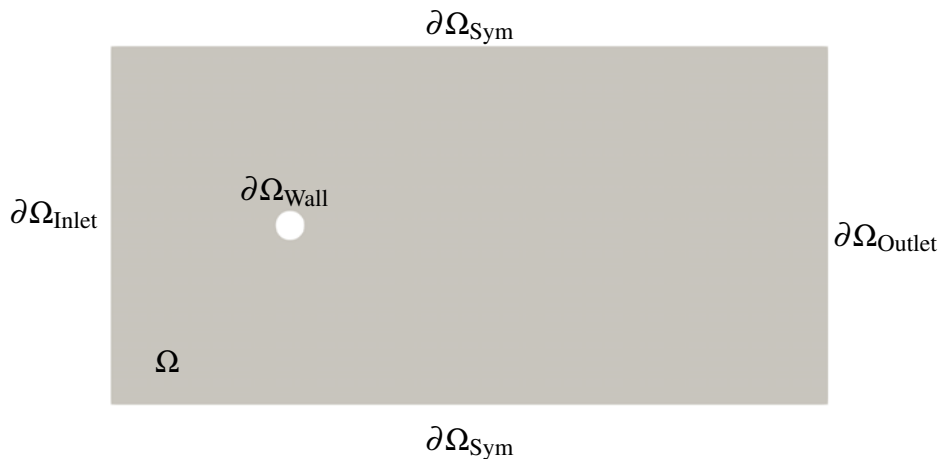


Figure 5.1: Domain of the 2D flow problem with labelled boundaries and dimensions.

The mesh utilised for the simulation was generated using the BlockMesh feature of OpenFOAM. The mesh was specifically designed to accurately capture the flow characteristics around the cylinder. The mesh consisted of hexahedral elements, which are three-dimensional elements with six rectangular faces. However, two of these faces at the maximum and

minimum  $Z$  values are ignored to solve in 2D. Hexahedral meshes are commonly used in CFD simulations due to their ability to provide good accuracy and numerical stability. In order to accurately capture the flow features near the cylinder, the mesh was refined in that region. This means that the mesh elements were smaller and more closely spaced around the cylinder compared to other areas. This refinement allows for a finer resolution of the flow variables, such as velocity and pressure, where large spatial variations are expected. Additionally, the mesh was refined upstream and downstream of the cylinder, although to a lesser extent compared to the immediate vicinity of the cylinder. This refinement helps capture the flow behaviour in these regions, which can be influenced by the wake generated by the cylinder. To reduce computational costs while maintaining accuracy, the mesh was gradually coarsened as the distance from the cylinder increased. Far from the cylinder, where the flow is less influenced by the cylinder, the mesh elements were larger. This coarsening helps speed up the simulation while still providing sufficient resolution to capture the overall flow behaviour accurately. The average cell length in the unrefined areas was specified as 2 mm, indicating the approximate size of the mesh elements in those regions. Downstream of the cylinder, where some refinement was still necessary, the average cell length was further reduced to 1 mm. The most refined region, immediately surrounding the cylinder, had an average cell length of 0.3 mm, ensuring a high level of detail in capturing the flow dynamics near the cylinder. A mesh of approximately 36000 elements can be seen in Figure 5.2.

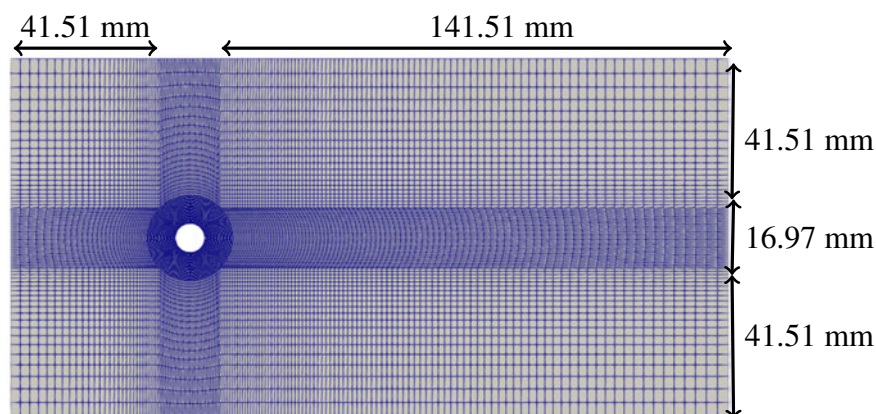


Figure 5.2: Visualisation of the 2D mesh used in benchmarking.

The time steps used for each simulation were adjusted to keep the CFL number at constant for each simulation. The time steps for each Reynolds number can be seen in Table 5.1.

$Re$	Time Step Size [s]
50	0.02
75	0.00133
100	0.001
150	0.00066
195	0.0005

Table 5.1: Time step at each Reynolds number for the 2D case for flow around a cylinder.

### Initial Boundary Value Problem

These initial conditions define the values of the fluid velocity and pressure throughout the entire fluid domain (denoted by  $\Omega$ ) at time zero. These initial conditions provide a starting point for the numerical solution of the governing equations. The fluid simulations for the 2D mesh will be run for both geometries while varying Reynolds number below 200. The initial conditions used for each run are outlined in Table 5.2.

$Re$	$u_x$ [ $\text{m s}^{-1}$ ]	$p$ [Pa]
50	0.00627	0
75	0.00941	0
100	0.0125	0
150	0.0188	0
195	0.0245	0

Table 5.2: Initial conditions for the 2D case for flow around a cylinder.

The boundaries depicted in Figure 5.1 are assigned specific boundary conditions. The boundary condition applied to the boundary  $\partial\Omega_{\text{Inlet}}$  corresponds to the conditions described by (3.16a) and (3.16b). The boundary  $\partial\Omega_{\text{Outlet}}$  is subject to the conditions specified in (3.17a) and (3.17b). Similarly, the boundary  $\partial\Omega_{\text{Sym}}$  is subjected to the conditions outlined in (3.19a) and (3.19b). Lastly, the boundary conditions on  $\partial\Omega_{\text{Wall}}$  represent a solid wall and adhere to (3.20a), (3.20b), (3.20c) and (3.20d).

### Mesh Sensitivity Study

Prior to running the simulations of a geometry of a finite height a mesh sensitivity study was conducted using a Reynolds number of 195. The metrics used were the average drag coefficient and the root mean squared of the lift coefficient as seen in Figure 5.3. This is to account for the steady-state forces and the oscillating forces respectively.

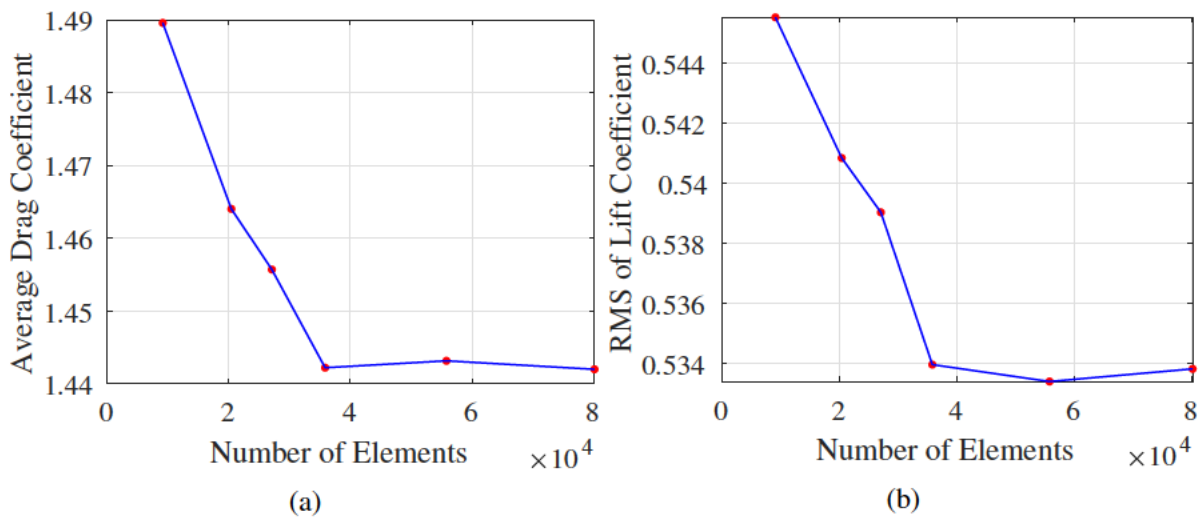


Figure 5.3: Results for a mesh independency test for a 2D cylinder using the number of elements in the mesh vs (a) average drag coefficient (b) Root mean squared of the lift coefficient.

The mesh sensitivity study results show that the solution is mesh independent when the mesh has around  $4 \times 10^4$  elements when meshed in the manner described in this section. The mesh selected for this study was the mesh with approximately 36000 elements.

### 5.1.2 2D Fluid Results

The 2D results are divided into a visualisation exercise and a benchmarking of the Strouhal number. The flow visualisation provides an insight into evolution of the predicted flow patterns as Reynolds number increases. The Strouhal number validation study can be used to determine the range of validation of the 2D models against Reynolds number. The contour plot shown in Figure 5.4a displays a creeping flow behaviour of flow around a 2D cylinder. This flow displays little to no vortex shedding as the Reynolds number is significantly small. The streamline plot shown in Figure 5.4b shows a recirculation region immediately downstream of the cylinder. The far field regions displays a laminar flow with very little to no turbulence present.

### Flow Visualisation

A visual comparison of the 2D simulations at increasing Reynolds number is given in order to display the presence of the Kármán vortex street. A visual comparison in the study provides an effective way of communicating complex information and conveying the essential characteristics of fluid flow behaviour.

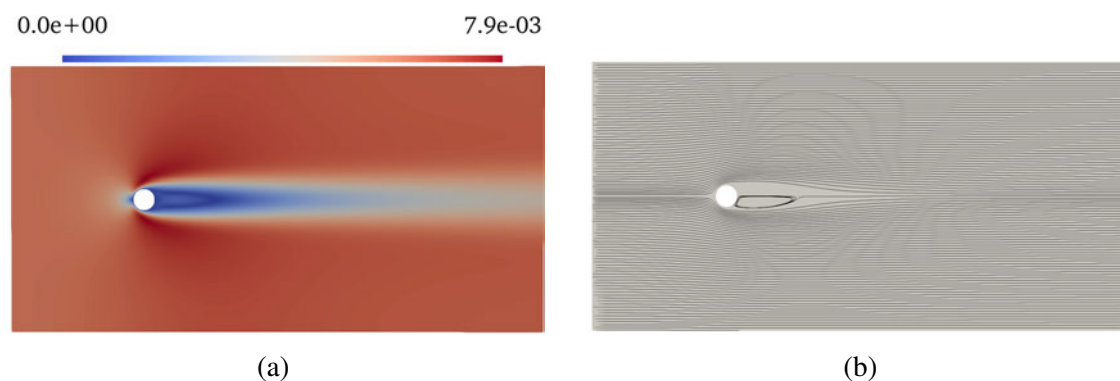


Figure 5.4: (a) Contour plot of velocity magnitude in the surface plane with a normal in the  $z$  direction at  $Re = 50$  with the colour bar and range shown in the units  $\text{m s}^{-1}$ . (b) Streamline plot of velocity flowing around a 2D cylinder for  $Re = 50$ .

When observing the solutions of fluid simulations with higher Reynolds numbers, the contour plots of velocity magnitude display the wavelike behaviour in the wake of the cylinder as shown in Figure 5.5. In the streamline plots, in Figure 5.6, denser regions of streamlines indicate the presence of more pronounced vortex shedding. These denser regions exhibit wavelike patterns, with the density of lines increasing as the Reynolds number rises. This increase in density signifies the amplification of vortex shedding and the formation of more coherent vortices in the wake. The changing line density of the streamline plots provides valuable information about the flow dynamics. It allows for the identification of regions where vortices are being shed, the size and strength of the vortices, and the spatial distribution of the wake region. As the Reynolds number increases, the streamline plots depict a transition from laminar flow to a flow regime characterised by vortex shedding and turbulent wake formation. This transition is evident in the changing line density and the wavelike behaviour displayed in the denser regions.



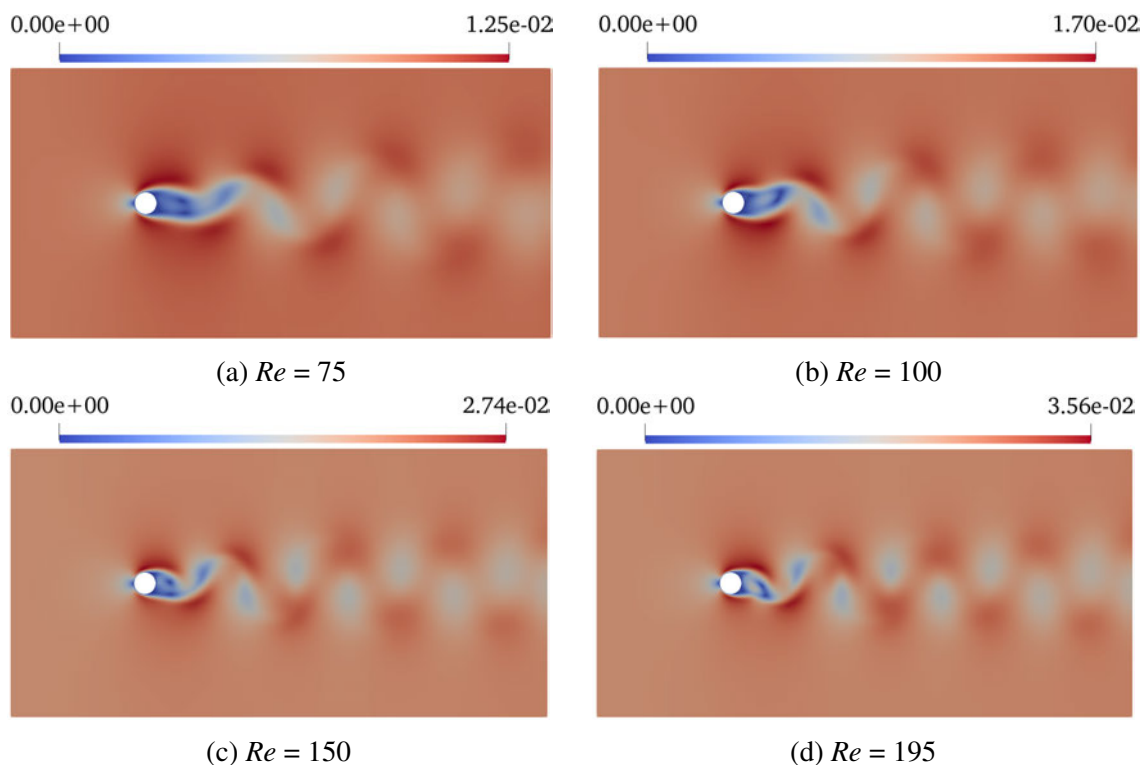


Figure 5.5: Contour plot of velocity magnitude in the surface plane with a normal in the  $z$  direction with relevant colour bars and ranges shown in the units  $\text{ms}^{-1}$ .

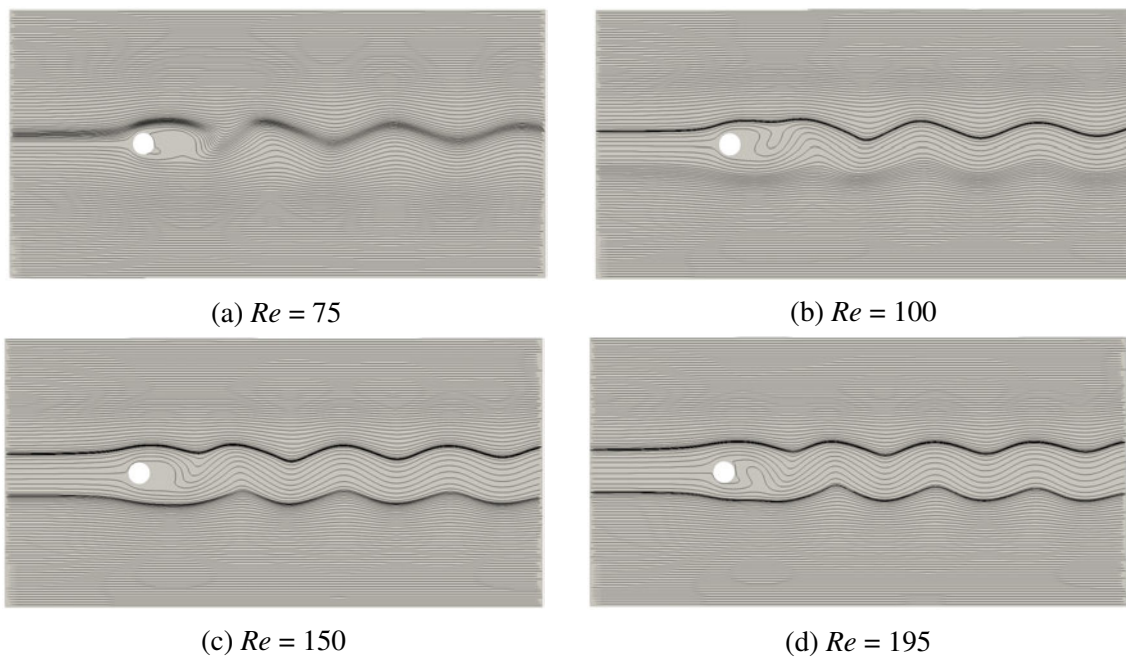


Figure 5.6: Streamline plot of velocity flowing around a 2D cylinder for various input velocities and Reynolds numbers.

### Fluid Flow Metrics for Benchmarking

A discrete fast Fourier transform was employed to analyse the time history of lift coefficient in terms of frequency, thereby identifying the peak frequencies associated with vortex shedding in the simulations. These frequencies were then used to compute the Strouhal number (via equation (3.23)), which is a key parameter characterising vortex shedding. Comparing the Strouhal number obtained in the simulations to existing literature allows for validation of the results. The temporal variations of the lift and drag coefficients are indicative of the vortex shedding phenomenon. The lift and drag coefficient time history plots display oscillatory behaviour with different amplitudes. The drag force exhibits a smaller amplitude in comparison to the lift force, indicating a smaller contribution to the overall forces acting on the cylinder. The lift force, on the other hand, oscillates around zero. Figure 5.7, demonstrates a very small amplitude of oscillation of the lift coefficient only seen when looked closely on Figure 5.7a. Furthermore, the dominant frequency of oscillation is found by taking the fast Fourier transform of the lift coefficient and it can be seen that the amplitude of lift is very small.

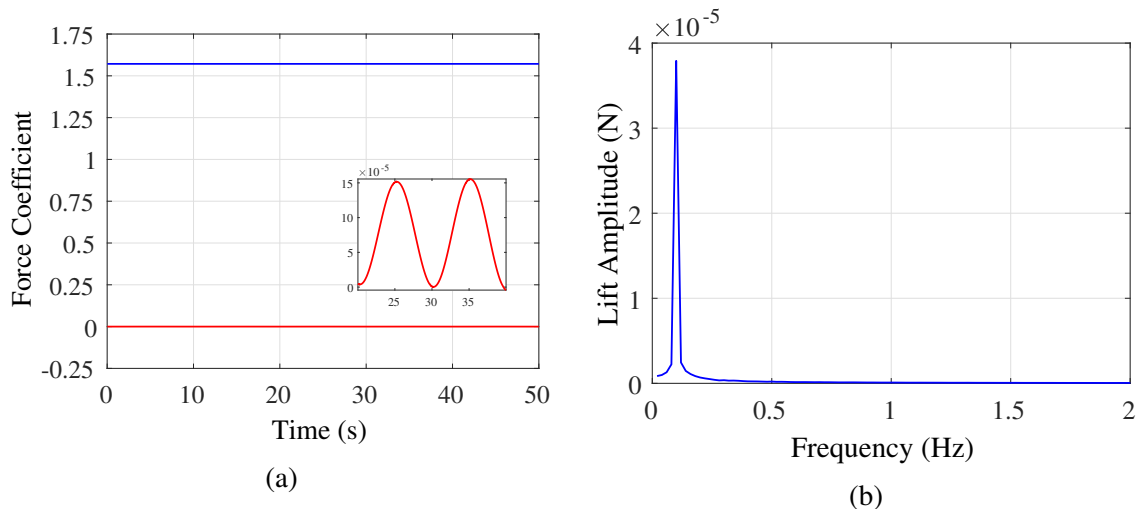


Figure 5.7: Plots to show (a) the time history of the and lift (—) and drag (—) coefficient in the 2D fluid simulations at  $Re = 50$ . Lift and drag are found using (3.21a) and (3.21b). (b) The discrete Fourier transform of the lift coefficient with respect to frequency in order to observe what frequencies of vortex shedding are present in the 2D fluid simulations at  $Re = 50$ .

The Strouhal numbers are then obtained from the peak frequencies in Figure 5.9 and using (3.23) to allow for a benchmarking exercise of the fluid flow. The data is obtained in Table 5.3. The time history of lift and drag coefficients, in Figure 5.8, show a clear increase in the frequency of vortex shedding and the increase in the lift and drag coefficient amplitudes of oscillation. This finding provides further validation of the study's methodology and results,

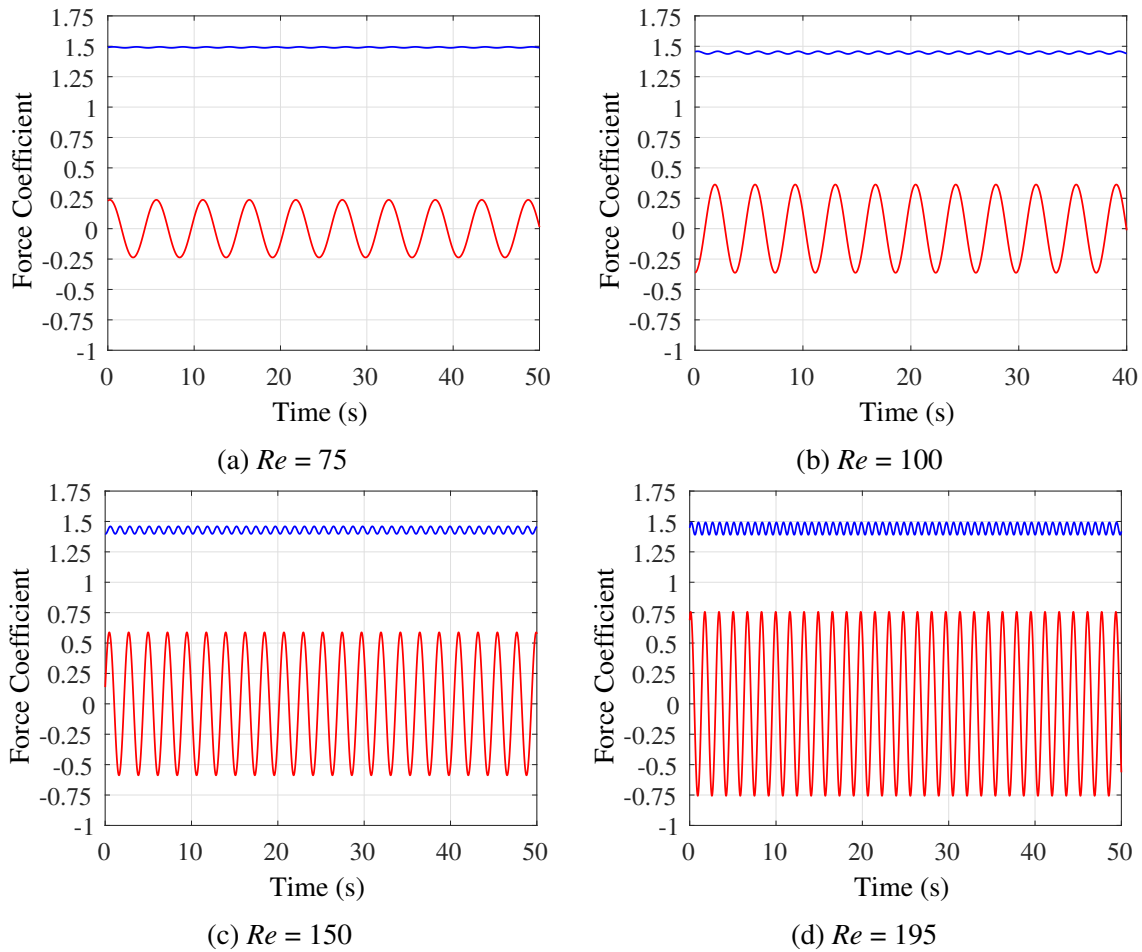


Figure 5.8: Plots to show the time history of the lift (—) and drag (—) coefficient in the 2D fluid simulations. Lift and drag are found using (3.21a) and (3.21b).

indicating that the numerical approach used in the study is accurate and effective in predicting the behaviour of fluid flow around the cylinder. These results also accurately replicate results found in [20, 31, 80] seen in Figure 5.10 and later in Figure 5.19a. Further benchmarking of the Strouhal numbers against literature will be carried out in the following section.

$Re$	Peak Frequency [Hz]	$St$
50	0.100	0.128
75	0.185	0.157
100	0.266	0.171
150	0.441	0.188
195	0.609	0.198

Table 5.3: Peak frequencies and Strouhal numbers found for each 2D simulation at varying Reynolds numbers.

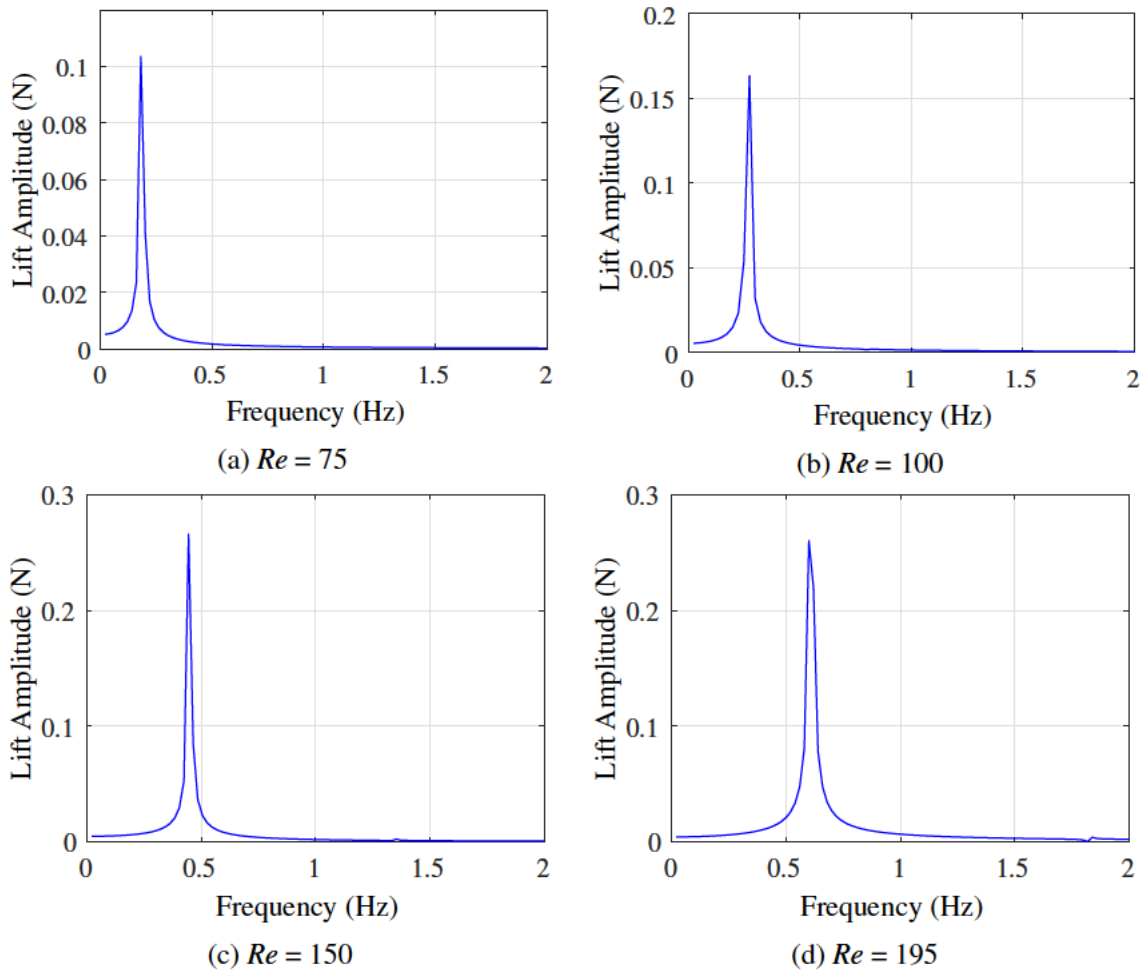


Figure 5.9: Plots to show the discrete Fourier transform of the lift coefficient with respect to frequency in order to observe what frequencies of vortex shedding are present in the 2D fluid simulations.

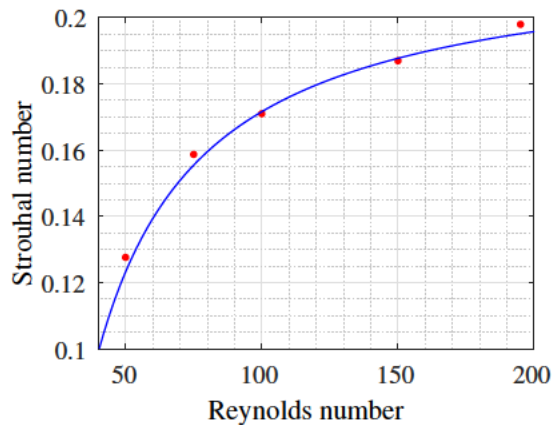


Figure 5.10: Plots to show the obtained Strouhal number of the wake of the fluid (●) for each simulation with respect to the flows Reynolds number compared with the expected Strouhal number trend line (—) defined in [3].

### Outcomes of 2D modelling

In conclusion, the study employed visual comparisons, contour plots, and streamline analyses to illustrate the flow characteristics around a 2D cylinder at varying Reynolds numbers. The transition from laminar flow to vortex shedding and turbulent wake formation was clearly observed as Reynolds number increased. The investigation also utilised a discrete fast Fourier transform to identify peak frequencies associated with vortex shedding, which were used to compute the Strouhal number, a critical parameter characterising vortex shedding. The Strouhal numbers obtained in the simulations were found to align with the analytical solutions in the industry standards, providing validation for the study's methodology and results. These findings contribute to a comprehensive understanding of fluid flow behaviour around cylinders and further validate the study's outcomes.

### 5.1.3 3D Fluid Model

The 3D model is run at several Reynolds numbers in order to benchmark the fluid model for flow around a cylinder. Several metrics, such as Strouhal number and average drag coefficient, will be used in benchmarking. Benchmarking a 3D infinitely long cylinder before considering finite height simulations can be beneficial for several reasons. This setup is simpler to model, allowing for the gain of insights into the fundamental fluid dynamics involved such as the vortex shedding and how vortices vary in the axial direction of the cylinder. It also allows for the validation of the turbulence model used. Understanding the behaviour of an idealised case can serve as a foundation for comprehending the nuances introduced by finite heights and other geometric variations.

#### 3D Domain Description and Spatial Discretisation

3D fluid simulations will be run for the following input velocities and Reynolds numbers. For cylinders with a diameter of 0.03 m. With a cuboid domain defined by the points  $(-0.15, -0.18, 0.00)$  and  $(0.45, 0.18, 0.30)$  with units of meters. The domain is shown in Figure 5.11. Initial runs were carried out to find a domain size for these simulations where the gradient for pressure around the cylinders had become zero at the walls of the domain. The blockage ratio of the run was around 8% in order to make sure the blockage effect did not affect the simulation.

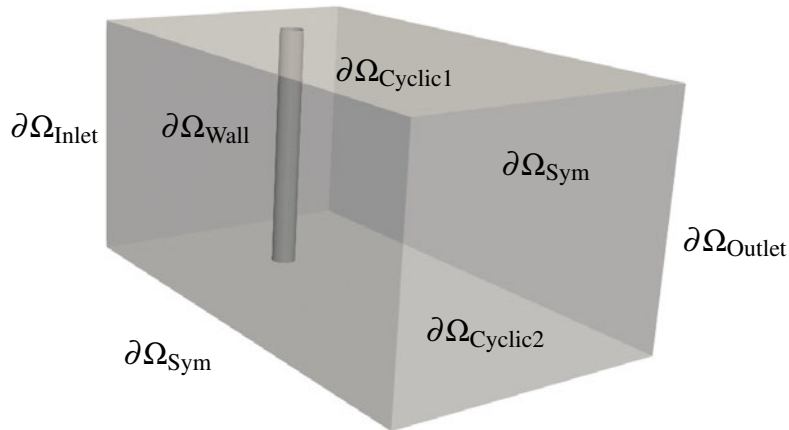


Figure 5.11: 3D set up for flow around a cylinder for a straight cylinder with labelled boundaries.

The mesh was created via OpenFoam's BlockMesh utility. The mesh is a structured hexahedral mesh with added inflation layers added by OpenFoam snappyHexMesh utility. The mesh was specifically designed to capture the flow characteristics around the cylinder as accurately as possible. As is the same in the 2D cases, in order to accurately capture the flow features near the cylinder, the mesh was refined in that region around the cylinder. This means that the mesh elements were smaller and more closely spaced around the cylinder compared to other areas. This refinement allows for a finer resolution of the flow variables, such as velocity and pressure, where large spatial variations are expected. In this 3D case, the mesh is split in the  $z$  direction into 150 'layers'. The average mesh element size varies with the the sub-volume of the overall mesh. The volumes can be labelled as downstream, upstream, sides, far field downstream and far field upstream. The average mesh sizes are seen in the following Table 5.4

Sub-volume	Average dimension size [mm]
Upstream	1.08
Downstream	1.06
Sides	1.22
Far Field Upstream	2.51
Far Field Downstream	2.46

Table 5.4: The average mesh sizes for each sub-volume found in the 3D simulations with an infinitely long cylinder.

Further visual description of the 3D mesh can be seen in Figure 5.12b as an image of the surfaces of the mesh and also in Figure 5.12a as a slice of the mesh with a normal direction in the  $z$  direction.

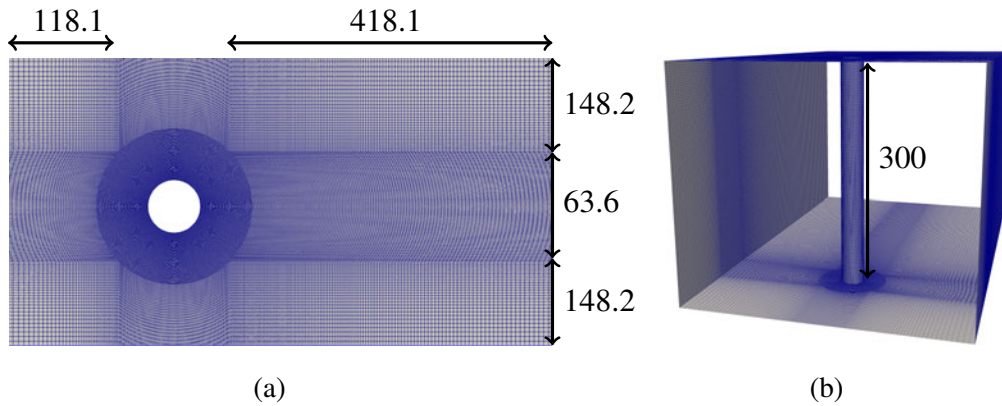


Figure 5.12: (a) Planar surface cut of the mesh displaying the different regions of refinement. (b) 3D mesh surface for the flow around a long cylinder with the inlet and outlet surfaces missing. The units of measurement are in mm.

The time steps used for each simulation were adjusted to keep the CFL number at constant for each simulation. The time steps for each Reynolds number can be seen in Table 5.5.

$Re$	Time Step Size [s]
$1 \times 10^3$	0.002
$1 \times 10^4$	0.0002
$1 \times 10^5$	0.00002
$1 \times 10^6$	0.000002

Table 5.5: Time step at each Reynolds number for the 3D case for flow around a cylinder.

### Mesh Sensitivity Study

Prior to running the simulations of a geometry of a finite height a mesh sensitivity study was conducted using a Reynolds number of  $1 \times 10^6$ . The metrics used were the average drag coefficient and the root mean squared of the lift coefficient as seen in Figure 5.13. This is to account for the steady-state forces and the oscillating forces respectively.

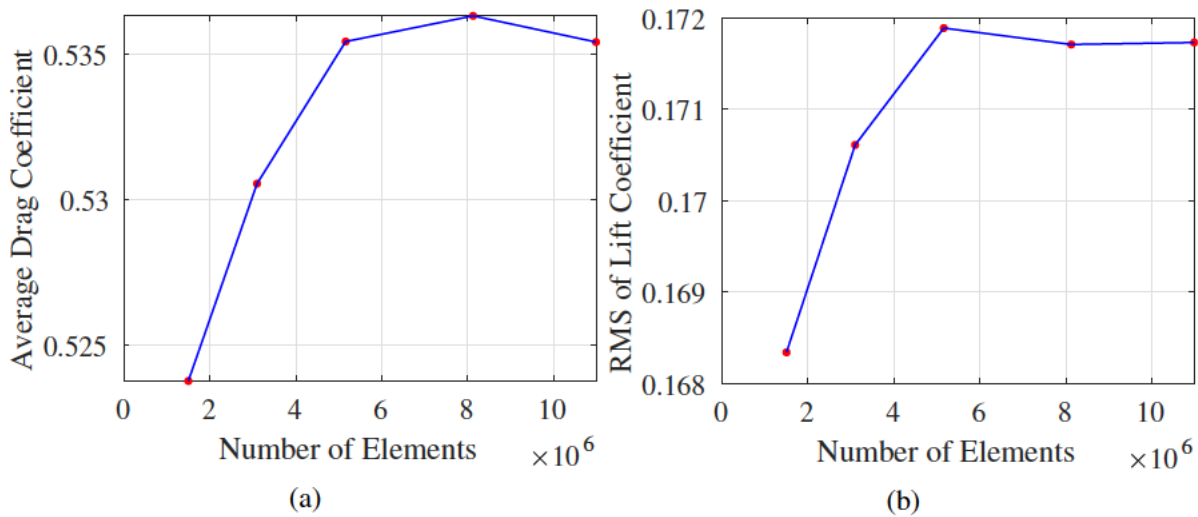


Figure 5.13: Results for a mesh independency test for a cylinder of infinite height using the number of elements in the mesh vs (a) average drag coefficient (b) Root mean squared of the lift coefficient.

The mesh sensitivity study results show that the solution is mesh independent when the mesh has over  $5 \times 10^6$  elements when meshed in the manner described in this section. The mesh selected for this study was the mesh with around 8 million elements. During the running of the simulations the average and maximum  $y^+$  values were monitored and were always below 100 to ensure the boundary layer was captured sufficiently by the wall functions used in this study.

### Initial Boundary Value Problem

These initial conditions define the values of the fluid velocity, pressure, turbulent kinetic energy ( $k$ ), specific dissipation rate ( $\omega$ ), and eddy viscosity ( $\nu_t$ ) throughout the entire fluid domain (denoted by  $\Omega$ ) at time zero. These initial conditions provide a starting point for the numerical solution of the governing equations using the  $k - \omega$  SST turbulence model. The flow is turbulent so the turbulent kinetic energy and the turbulent dissipation rate are set which provides closure for the Reynolds-averaged Navier-Stokes equations by modelling the effects of turbulence. The fluid simulations will be run for both geometries while varying Reynolds number. The following initial conditions were used for each run. The initial conditions shown in Table 5.6 were used to simulate the fluid in the domain.



$Re$	$u_x$ [ms <sup>-1</sup> ]	$p$ [Pa]	$k$ [m <sup>2</sup> s <sup>-2</sup> ]	$\omega$ [s <sup>-1</sup> ]
$1 \times 10^3$	0.0335	0	$7.66 \times 10^6$	2.41
$1 \times 10^4$	0.335	0	$4.31 \times 10^4$	18.04
$1 \times 10^5$	3.35	0	$2.42 \times 10^2$	135.29
$1 \times 10^6$	33.5	0	1.36	1014.54

Table 5.6: Initial conditions for the 3D case for flow around a cylindrical geometry.

The input velocity was increased to proportionally increase the Reynolds number of the problem. All initial conditions are also set on the boundaries. The initial values of the subsequent variables used by the  $k - \omega$  SST were also varied in order to provide a better guess for these values. The boundaries depicted in Figure 5.11 are assigned specific boundary conditions. The boundary condition applied to the boundary  $\partial\Omega_{\text{Inlet}}$  corresponds to the conditions described by (3.16). The boundary  $\partial\Omega_{\text{Outlet}}$  is subject to the conditions specified in (3.17). The boundaries  $\partial\Omega_{\text{Cyclic1}}$  and  $\partial\Omega_{\text{Cyclic2}}$  is subject to the conditions specified in (3.20). Similarly, the boundary conditions on  $\partial\Omega_{\text{Wall}}$  represent a solid wall and adhere to (3.18). Lastly, the boundary  $\partial\Omega_{\text{Sym}}$  is subjected to the conditions outlined in (3.19).

### 5.1.4 3D Fluid Results

The 3D results are presented in the same manner as the 2D previous. Firstly with a visualisation of the results and then an exploration of several flow metrics.

#### Visualisation of Results

The planar surface contour plots of velocity magnitude were obtained in order to visualise the results. In the above planar plots a clear vortex shedding pattern can be seen from the velocity magnitude and the clarity of these vortices reduces with Reynolds number due to the normalised difference in maximum and minimum values in the wake reducing with Reynolds number. A change in the length of each vortex is observed from Figure 5.14 as the Reynolds number is increased. To investigate this another planar cut in the XZ plane is taken for each case. It appears that at higher Reynolds numbers the turbulent effects in 3D become more prominent. This is seen by the presence of these spatial mode shapes at larger Reynolds numbers in Figure 5.15.

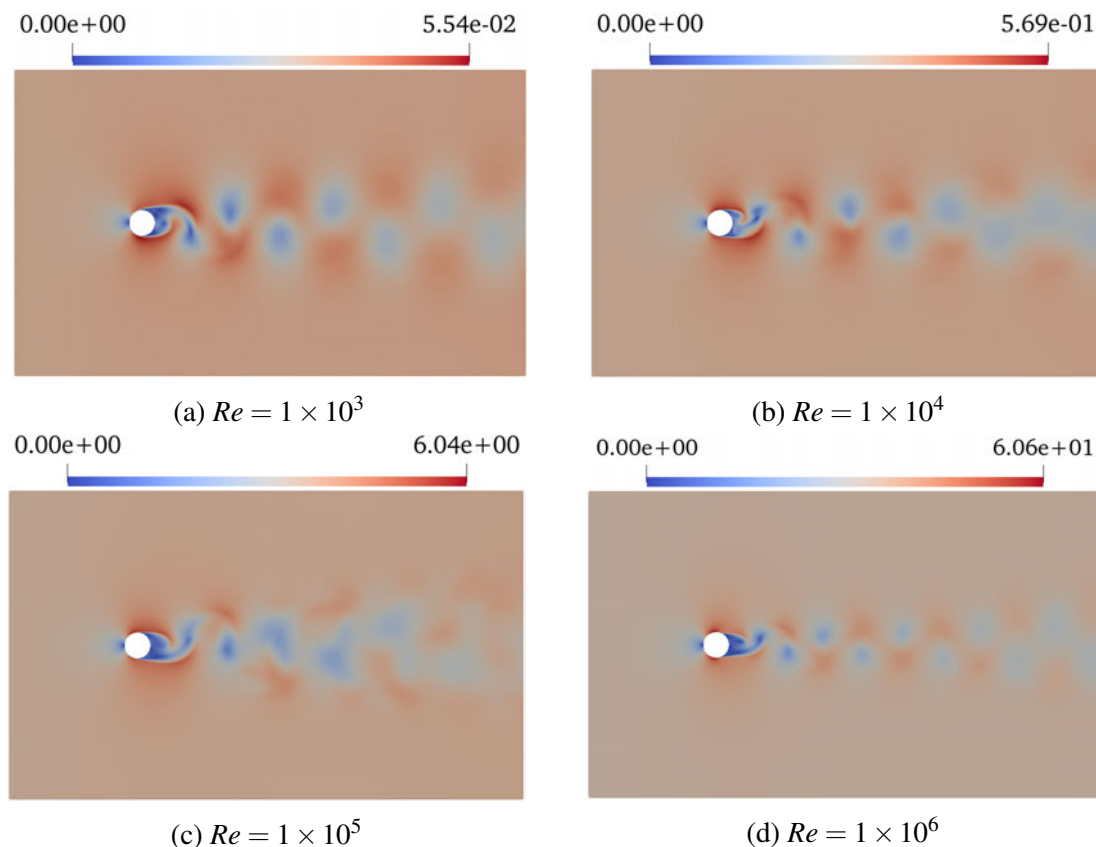


Figure 5.14: Above view of the 2D planar contour plots representing the scalar velocity magnitude. Each plane was in passed through the centre height of the cylinder. The colour bars and ranges are displayed separately for each case with the ranges in units  $\text{ms}^{-1}$ .

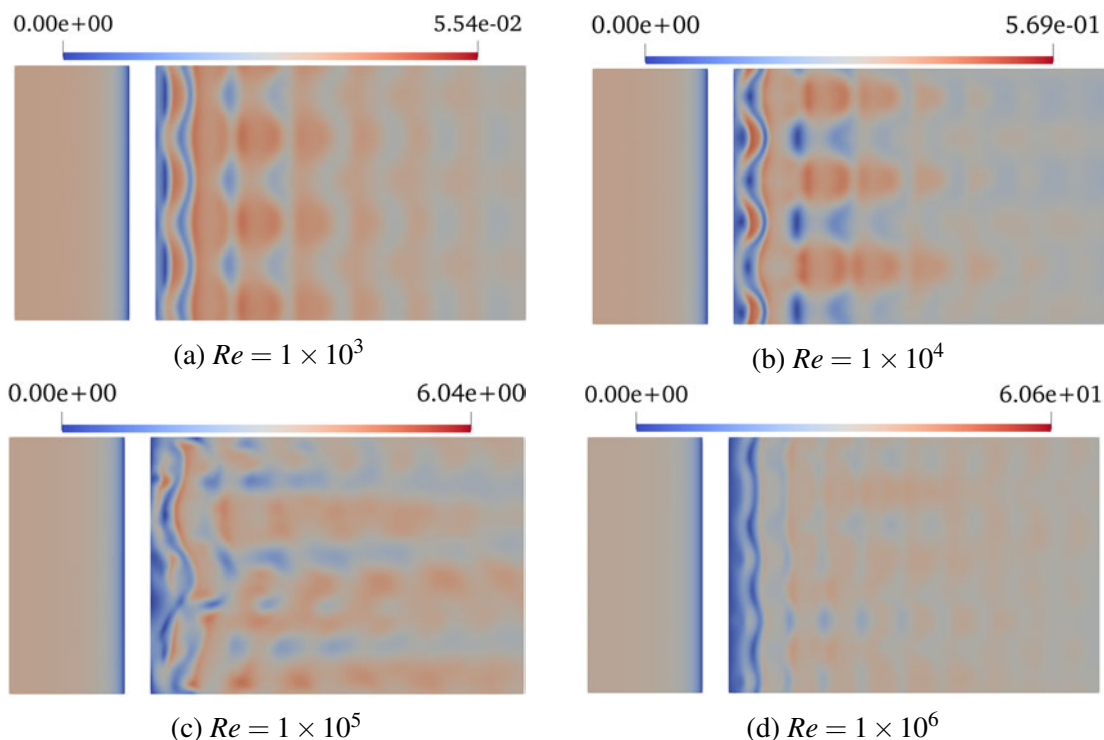


Figure 5.15: Side view of the 2D planar contour plots representing the scalar velocity magnitude. The colour bars and ranges are displayed separately for each case with the ranges in units  $\text{ms}^{-1}$ .

A clear display of the 3D effects of the turbulence can be seen in Figure 5.16. The figure shows several layers of alternating shedding in the  $z$  direction when looking at the turbulent viscosity.

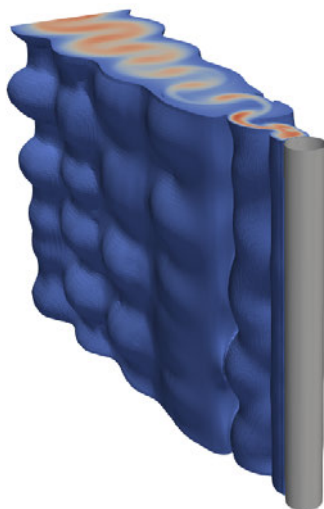


Figure 5.16: Plot of isovolumes of the turbulent viscosity  $\nu_t$  at a Reynolds number of  $1 \times 10^5$ .

### Fluid Flow Metrics for Benchmarking

For the 3D results, the time histories for the lift and drag coefficient were obtained in order to gain an insight into the aerodynamic behaviour of the cylinders in the flow environment. The lift and drag coefficients give an insight into the fluctuations in force so it is helpful to consider the fast Fourier transform of these values in order to view the frequency spectra of the forces. This can provide a good opportunity to benchmark the Strouhal number of these simulations against the Reynolds number. The results seen in Figure 5.17 display lift coefficient fluctuations of a constant amplitude for all Reynolds numbers except for a Reynolds number of  $1 \times 10^5$  (Figure 5.17c) which displays a time-varying amplitude. It can also be seen in Figure 5.18 that for all Reynolds numbers except for  $1 \times 10^5$  (Figure 5.18c) a single mode of vortex shedding is present. This is due to the change in turbulence regime at the boundary layer of the cylinder from a laminar to a turbulent boundary layer.

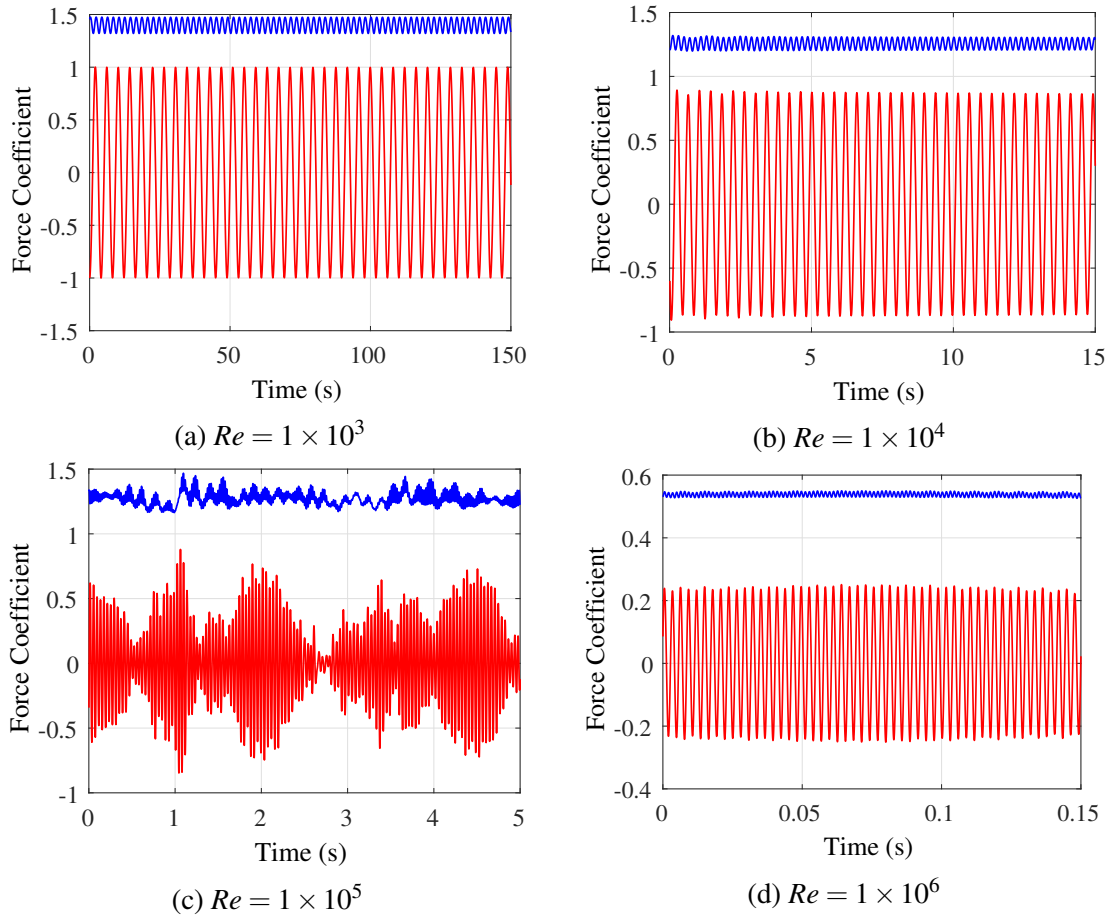


Figure 5.17: Plots to show the time history of the lift (—) and drag (—) coefficient in the 3D fluid simulations at various Reynolds numbers. Lift and drag are found using (3.21a) and (3.21b).

The Fourier transform of lift coefficient is then taken in order to obtain the Strouhal number used in benchmarking these simulations against Strouhal numbers found in the literature through experimentation or numerics. The Strouhal number is found using (3.23) and shown below in Table 5.7.

$Re$	Peak Frequency [Hz]	$St$	Average $C_d$
$1 \times 10^3$	0.2468	0.222	1.40
$1 \times 10^4$	2.533	0.226	1.25
$1 \times 10^5$	24.51	0.219	1.27
$1 \times 10^6$	345.3	0.311	0.50

Table 5.7: Peak frequencies, Strouhal numbers and average drag coefficients found for each 3D simulation at varying Reynolds numbers.

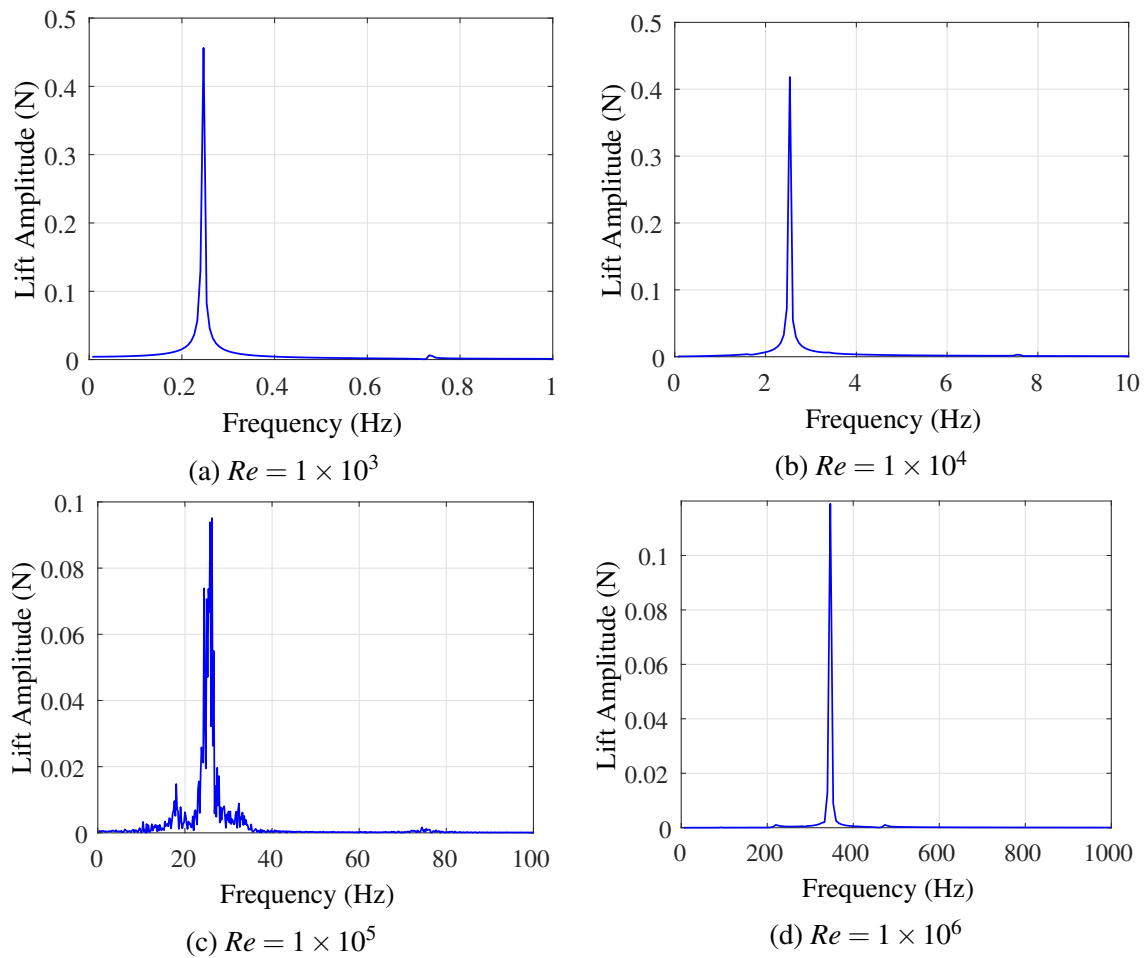


Figure 5.18: Plots to show the discrete Fourier transform of the lift coefficient with respect to frequency of vortex shedding are present in the 3D fluid simulations.

After collecting the results for the Strouhal number for each run while varying Reynolds number, the relationship between these two parameters could be plotted for this problem. The following results are plotted over experimental results of flow over a cylinder [57,58] with good agreement. The average drag coefficient was also taken for each run while varying Reynolds number. The results were also plotted over experimental results in [64] with good agreement.

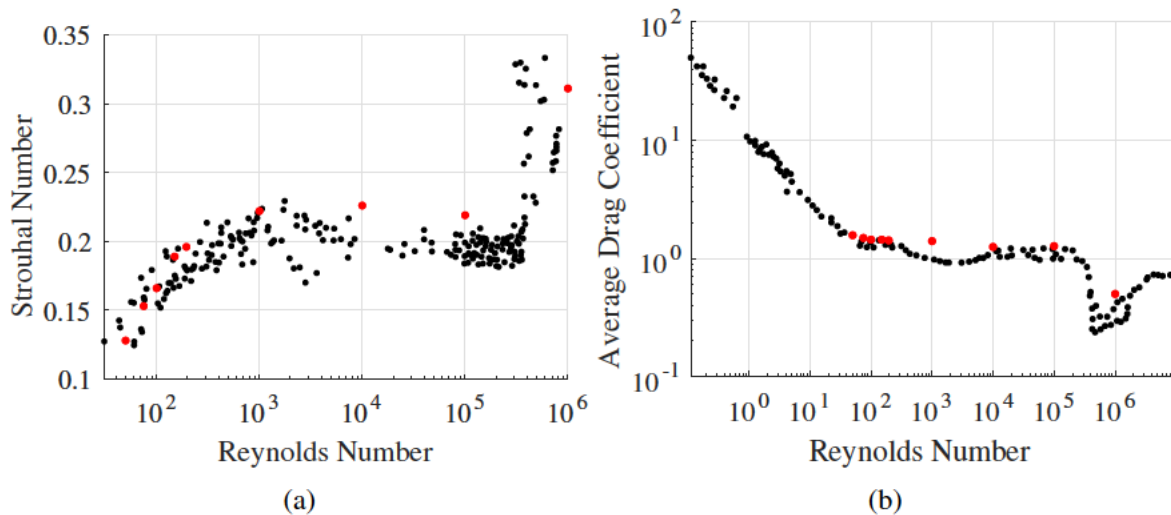


Figure 5.19: (a) Strouhal number vs Reynolds number for a range of Reynolds numbers up to  $1 \times 10^6$ . The black markers (●) represent the experimental findings from various studies reported in [57, 58]. The results from all the simulations are displayed as (●). (b) Average Drag Coefficient vs Reynolds number for a range of Reynolds numbers up to  $1 \times 10^7$ . The black markers (●) represent the experimental findings from various studies reported in [64]. The results from the 3D simulation are displayed as (●).

### Outcomes of 3D Modelling of Cylinders of Infinite Height

The 3D simulations of flow around the cylinder have been presented and analysed. These visualizations demonstrate a transition from laminar flow to turbulent flow with increasing Reynolds numbers, as evidenced by changes in vortex shedding behaviour and spatial mode shapes.

Fluid flow metrics, specifically the lift and drag coefficients, were examined to gain insights into the aerodynamic behaviour of the cylinder in the flow environment. The Strouhal numbers and average drag coefficients obtained from these simulations were compared with experimental data and showed good agreement, indicating the accuracy and effectiveness of the numerical approach.

## 5.2 Fluid Structure Interaction for Finite Height Geometries

This section will delve into the domain of fluid mechanics and focus on the setup and running of simulations, as well as the sampling of fluid forces acting on the fluid mesh and the transfer of these forces onto a surface of the solid mesh. The goal is to simulate fluid structure interaction, specifically the interaction between a fluid and a solid cylinder. The

section will display a one-way coupling approach to fluid structure interaction using a reduced order method. This section will compare structural response to fluid flow around a straight hollow cylinder and a hollow cylinder with helical strakes. The purpose of this comparison is to test the effectiveness of the helical strakes in reducing vortex-induced vibration. In order to achieve this goal, the section will describe the fluid behaviour and solid behaviour in detail. This will include an explanation of the forces acting on the fluid and solid objects and how they interact with each other. The section will also address any shortcomings of the model and provide suggestions for further improvements.

The workflow of this fluid-structure interaction tool is visually depicted in Figure 5.20. It commences with the creation of the structural geometry, which is generated by the user's software of choice and saved as a STEP file. This geometry serves a dual purpose: as the solid domain for meshing and as the outer surface of the fluid domain for subsequent boolean operations during the fluid domain geometry creation. The fluid mesh generation takes place using ANSYS Fluent and it is converted to an OpenFOAM mesh. The fluid is then simulated on OpenFOAM and the force field files are outputted.

The meshing of the solid domain is accomplished through Gmsh and exported in MATLAB file format. However, an important consideration arises as MATLAB mesh files lack the capability to label face groups accurately. To address this limitation, an OpenFOAM mesh is also created to facilitate the precise labelling of nodes situated within the faces.

A custom MATLAB script is employed to read both mesh files and the OpenFOAM reference file, along with the force field files. The nearest point interpolation method (NPIM) is executed, leading to the application of a force vector to every node on the surface of the solid mesh. This allows for the implementation of the reduced-order model, as elaborated in Section 4.3, which results in the generation of a displacement vector field for each time step. Further clarity on this workflow and the code can be found on <https://github.com/CallumLloydJones/Tool-Predicting-Thermowell-Structural-Response>.

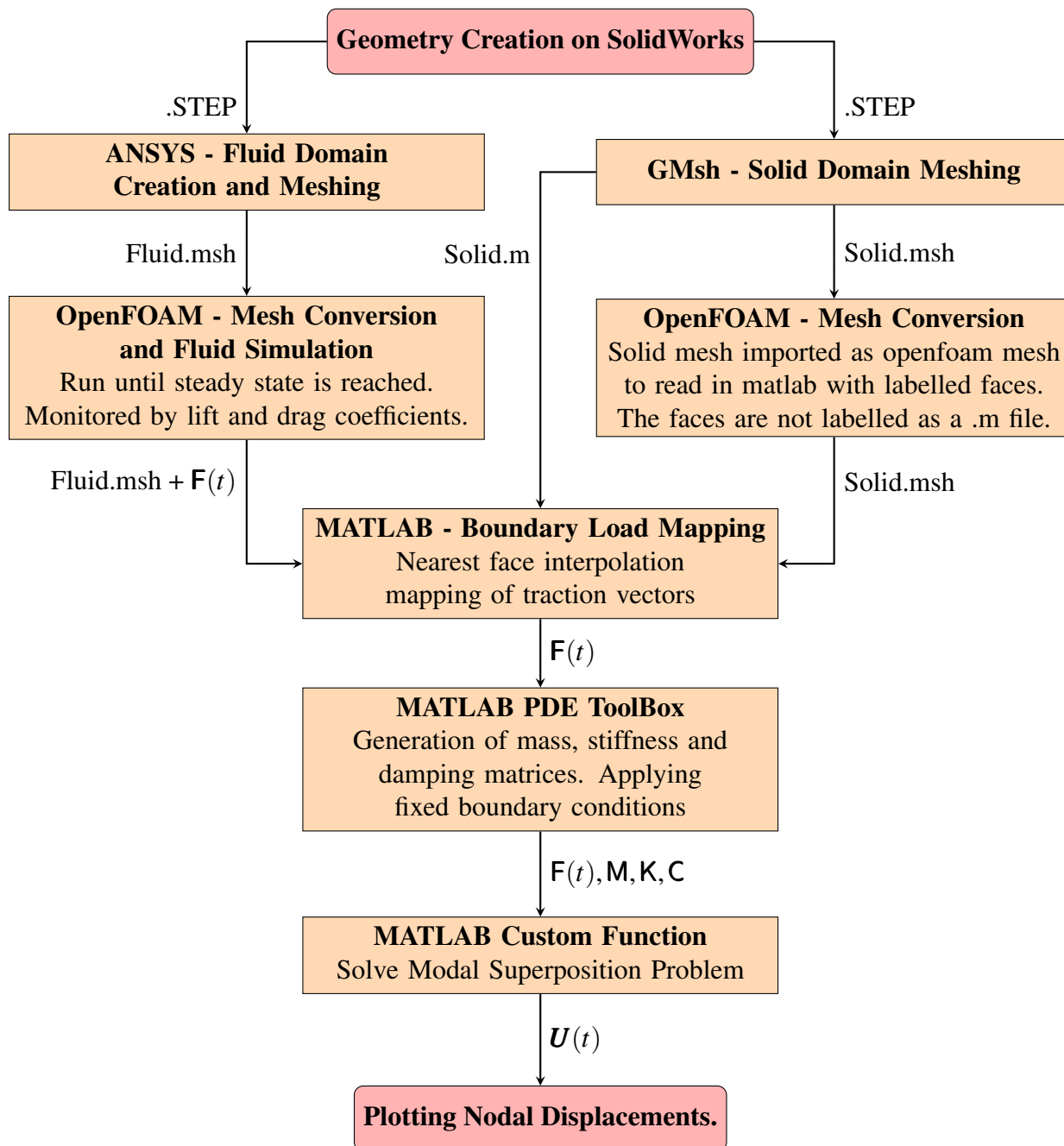


Figure 5.20: Workflow of the fluid-structure interaction tool from the geometry creation to the time varying displacement vector field.



### Fluid Domain Description and Spatial Discretisation

3D fluid simulations will be run for the following input velocities and Reynolds numbers for cylinders with a diameter of 0.03 m and a height of 0.3 m. With a cuboid domain defined by the points (-0.15, -0.18, 0.00) and (0.45, 0.18, 0.40) with the units of meters. The fin height for the cylinder with strake is 1.5 mm with a helical pitch of 0.03 m. The mesh was created via the

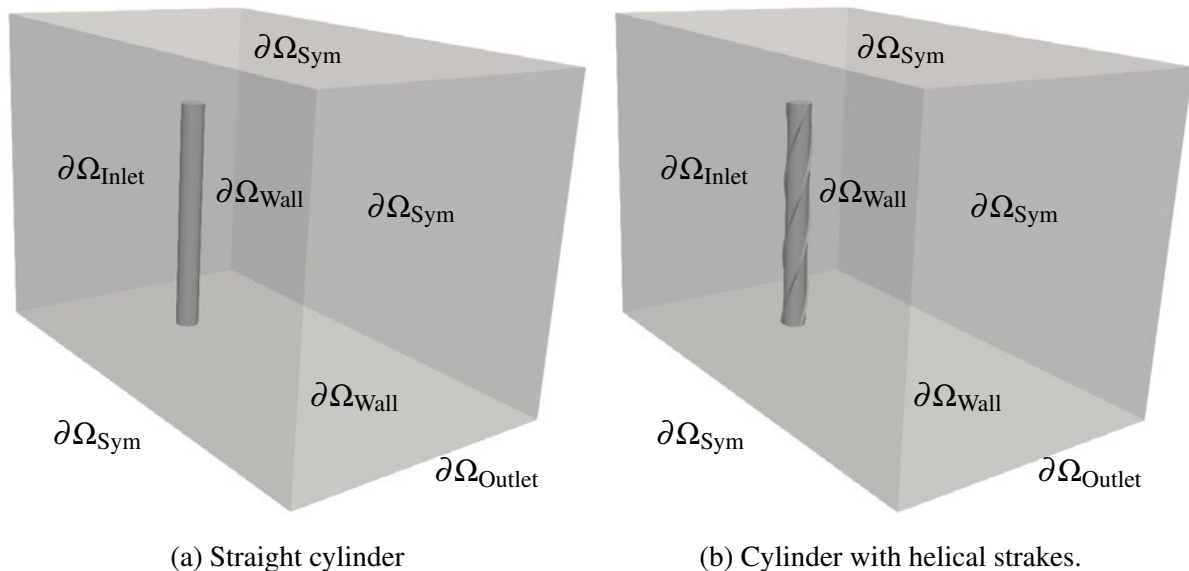


Figure 5.21: Sketch of the fluid domain with labelled boundaries for each case of finite height geometry.

same method as the previous example of a 3D simulation using ANSYS DesignerModeler with imported geometries for the cylinders from SolidWorks then exported as a FLUENT mesh and converted to an OpenFOAM mesh. The mesh is an unstructured tetrahedral mesh. This was necessary due to the complexity of the cylindrical design with the helical strakes attached and the difficulty to fit a structured mesh to the geometry. Also with the sharp helical strakes it is difficult to fit hexahedral elements to the outside of this geometry and maintain a high quality mesh. The quality of the mesh is compromised by the design of the helical strake and therefore non-orthogonal correctors are used to counteract tets which may have highly non orthogonal faces. The general element size in the mesh is 10 mm in areas where the flow is not expected to have large spatial gradients in its variables. Downstream of the geometry under investigation the element size is 4 mm while in a refinement cylindrical volume surrounding the geometry the element size is 1.5 mm. To capture the boundary layer, a precomputed inflation layer is added to the bottom wall and the wall of the geometry. There were 5 layers added to each wall. The first inflation layer surrounding the cylindrical geometry was a height of 0.17 mm

for  $Re = 1 \times 10^5 - 2 \times 10^5$  then then decreased to 0.02 mm for higher Reynolds numbers when the maximum  $y^+$  was observed to be larger than 100 for the larger height. This was done to ensure a reasonable  $y^+$  value of below 200. The first inflation layer covering the bottom wall was a height of 1.7 mm for all Reynolds numbers simulated. A very fine mesh was used in order to obtain an accurate results. A total of 13 million elements were used in each case. The surface mesh, as displayed in Figure 5.22, is appropriately refined in volumes where the spatial changes in the flow are of greater interest i.e. surrounding and downstream of the cylinder. This refinement is performed in order to capture larger gradients in the variables calculated without excessively increasing the computational expense.

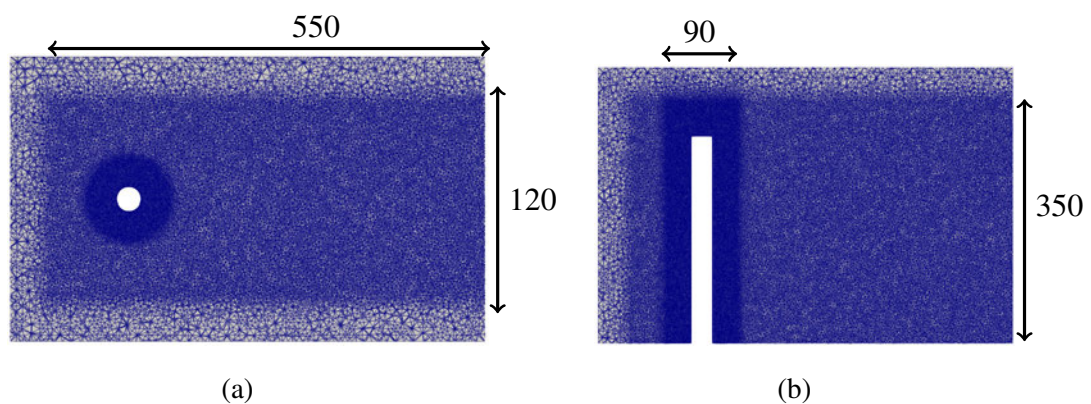


Figure 5.22: (a) Above view of the planar surface cut displaying the mesh for straight cylinder. (b) Side view of the Planar surface cut displaying the mesh for straight cylinder. All measurements are in the units mm.

Inflation layers are used in order to accurately capture the boundary layer surrounding the geometries. These inflation layers are important to produce suitable  $y^+$  values. These inflation layers can be difficult to produced as they often have to surround complex geometries as seen in Figure 5.23.

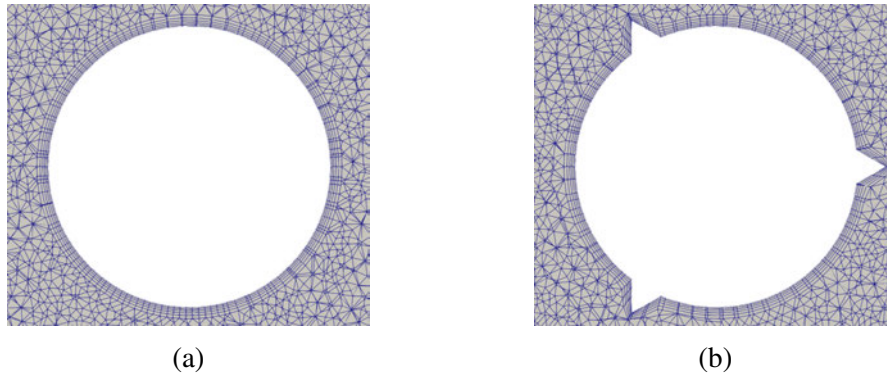


Figure 5.23: Planar surface cuts of the inflation layers for (a) Straight cylinder (b) Helical Cylinder.

### Governing Equations

The current problem is governed by the same set of equations as those employed for the 3D long cylinder problem. Specifically, the incompressible Navier-Stokes equations are solved with the aid of the  $k - \omega$  SST turbulence model. These equations are seen in (3.4), (3.8), (3.14b) and (3.14c).

In all simulations within this section, the fluid simulations are initially conducted until the drag coefficient stabilises, oscillating around a consistent non-zero value. This ensures that any initial condition effects on the simulation have been eliminated.

### Initial Boundary Value Problem

These initial conditions define the values of the fluid velocity, pressure, turbulent kinetic energy ( $k$ ), specific dissipation rate ( $\omega$ ), and eddy viscosity ( $\nu_t$ ) throughout the entire fluid domain (denoted by  $\Omega$ ) at time zero. However there are several differences to the boundary conditions places on the surrounding patches. The bottom boundary and the cylindrical geometry faces are treated as walls. Therefore, the same conditions given to the long cylinder in the 3D in the previous set of runs are now given to the cylindrical geometries and the bottom wall.

The fluid simulations will be run for both geometries while varying Reynolds number by the variance on input velocity. The initial conditions used for each run are displayed in Table 5.8.

The boundaries depicted in Figure 5.21 are assigned specific boundary conditions for both the straight cylinder and the cylinder with helical strakes. The boundary condition applied to

the boundary  $\partial\Omega_{\text{Inlet}}$  corresponds to the conditions described by (3.16). The boundary  $\partial\Omega_{\text{Outlet}}$  is subject to the conditions specified in (3.17). Similarly, the boundary  $\partial\Omega_{\text{Sym}}$  is subjected to the conditions outlined in (3.19). Lastly, the boundary conditions on  $\partial\Omega_{\text{Wall}}$  represent a solid wall and adhere to the (3.18).

$Re$	$u_x$ [ $\text{m s}^{-1}$ ]	$p$	$k$ [ $\text{m}^2 \text{s}^{-2}$ ]	$\omega$ [ $\text{s}^{-1}$ ]
$1 \times 10^3$	3.35	0	0.024	135.3
$2 \times 10^4$	6.70	0	0.081	248.1
$5 \times 10^5$	16.7	0	0.40	551.7
$1 \times 10^6$	33.5	0	1.36	1014

Table 5.8: The initial conditions for the 3D simulation of the flow around a cylinder of finite height provided for both cases, with and without strakes.

### Mesh Sensitivity Study

Prior to running the simulations of a geometry of a finite height a mesh sensitivity study was conducted using a Reynolds number of  $1 \times 10^5$ . The metrics used were the average drag coefficient and the root mean squared of the lift coefficient as seen in Figure 5.24.

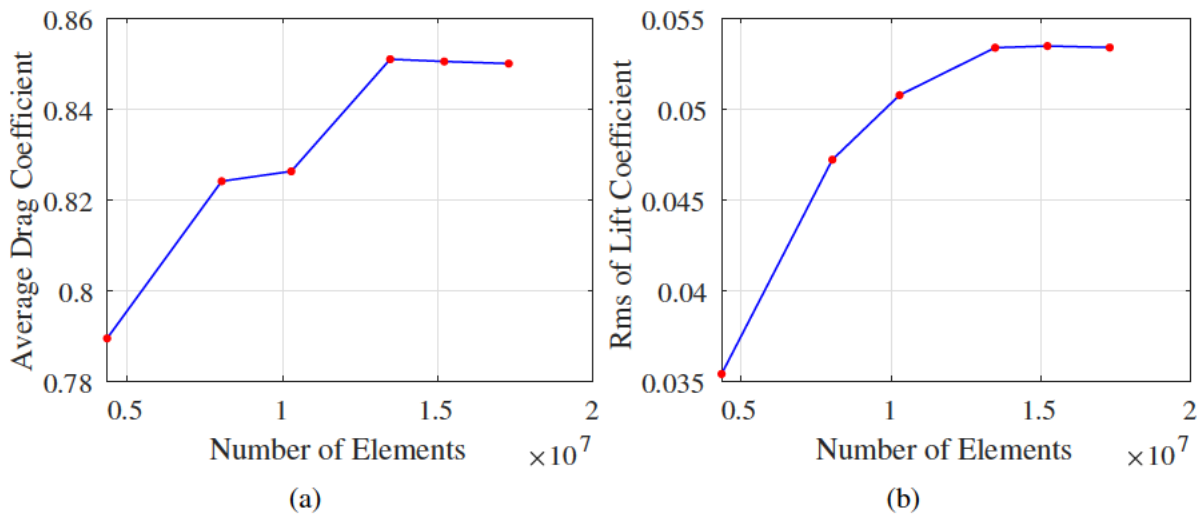


Figure 5.24: Results for a mesh independency test for a straight cylinder of finite height using the number of elements in the mesh vs (a) average drag coefficient (b) Root mean squared of the lift coefficient.

The mesh sensitivity study results show that the solution is mesh independent when the mesh has over  $1.3 \times 10^7$  elements when meshed in the manner described in this section. The mesh selected for this study was the mesh with around 15 million elements. During the

running of the simulations the average and maximum  $y^+$  values were monitored and were always below 100 to ensure the boundary layer was captured sufficiently by the wall functions used in this study. The upper limit on the CFL number was monitored to assure that it did not exceed a value of 1, however in practice it never exceeded 0.6.

### 5.2.1 Flow Modelling Results

The following sections compare the relevant flow metrics and the structural response of the two geometries. The first section will give the reader a visual guide of the flow around the cylinders to gain a understanding of the flow structures around the geometries, then the next one investigates the metrics of the flow and the structural response as well as checking the mapping has taken place with a high level of accuracy. Note that all of the following time varying plots are run until a steady state oscillatory solution is reached.

#### Visual Comparison

The visualisation of isosurface plots for turbulent viscosity at a Reynolds number of  $1 \times 10^5$ , shown in Figure 5.25, reveals distinct dissimilarities in the flow patterns downstream of the cylindrical geometries. An isosurface plot of turbulent viscosity shows a three-dimensional representation of the turbulent eddies and vortices present in the fluid flow. In general, high values of turbulent viscosity are associated with regions of high turbulence intensity, where energy is being dissipated by the turbulent eddies. By plotting an isosurface of a certain value of turbulent viscosity, we can visualise the regions of the flow where this value is exceeded, and therefore where the turbulence is strongest. This can provide valuable information about the structure of the flow, such as the presence of vortices, the location of separation and reattachment points, and the size and shape of turbulent structures. Notably, the geometry featuring helical strakes demonstrates no discernible large vortices, and there is an absence of any apparent alternating patterns. Conversely, downstream of the smooth cylinder geometry, a clear and organised Kármán Vortex street is evident, characterised by oscillating vortices. The presence of helical strakes can significantly alter the overall flow behaviour around the cylinder. The disturbed flow patterns, and changes in flow separation and vortex shedding induced by the strakes can result in a more complex and three-dimensional flow structure compared to a straight cylinder, leading to distinct differences in the planar surface streamlines of the fluid velocity. The Kármán vortex street can again be seen in the case of the straight cylinder but a far

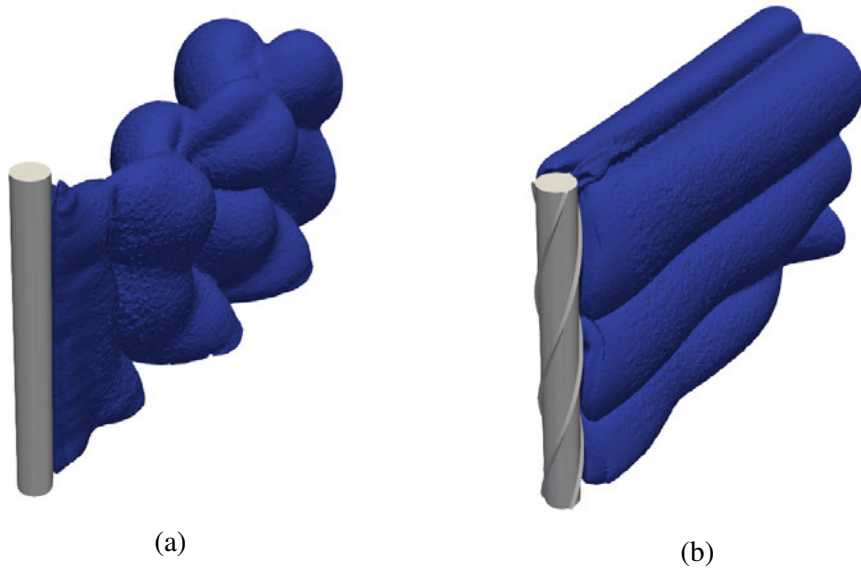


Figure 5.25: Comparison for the isovolumes of the turbulent viscosity  $\nu_t$  at a Reynolds number of  $1 \times 10^5$ . (a) Flow around a straight cylinder. (b) Flow around a cylinder with sharp finned helical strakes.

more complex structure has formed behind the structure with strakes then there is a transition to a smoother flow. The streamline plot, in Figure 5.26, shows a clear region of vortex disruption for the helical case compared to the straight case. The helical strakes guide the flow into the region of separation causing the break up of regular vortex creation.

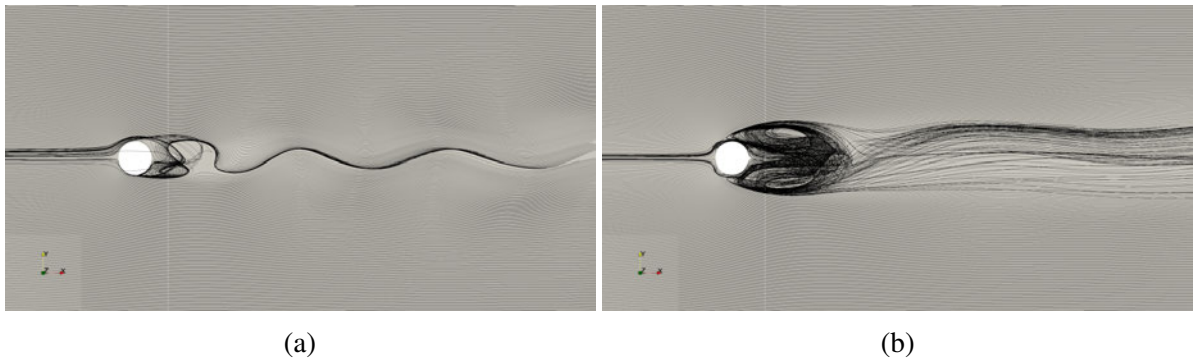


Figure 5.26: Comparison for the planar surface streamlines of the fluid velocity at a Reynolds number of  $1 \times 10^5$  for a straight cylinder vs a cylinder with helical strakes. (a) Straight cylinder (b) Helical cylinder.

When observing the differences between straight and helical cylinders, in Figure 5.27, one can notice clear suppression of vortices close to the tip of the cylinder in the straight case and less so in the helical cylinder. To disturbance of vortices formation can be seen clearly in the helical case compared to the straight case.

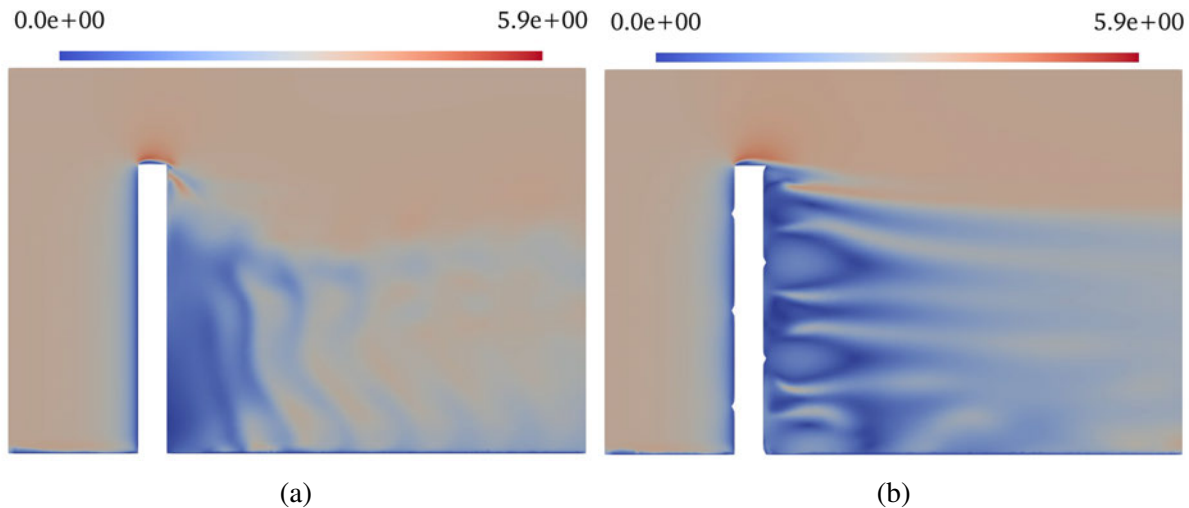


Figure 5.27: Comparison for the planar contour plots of the fluid velocity magnitude at a Reynolds number of  $1 \times 10^5$  for (a) a straight cylinder vs (b) a cylinder with helical strakes. Separate colour bars and ranges are displayed with the units of  $\text{m s}^{-1}$ .

### Fluid Flow Metrics - Cylinder

The time history of lift coefficients of the cylindrical geometry, seen in Figure 5.28, were taken in order to observe the lateral forces acting on the cylinder and how they change with time. This was done in order to observe what frequencies the driving force is acting at and to determine whether these frequencies are likely to coincide with the modal frequencies of the structure. In the observations, a non-zero component of the drag coefficient is evident, accompanied by an oscillating component with a smaller amplitude compared to the oscillation of the lift coefficient, in all cases studied. The lift coefficient oscillates around zero when averaged over a sufficiently long time period. Notably, the drag coefficient exhibits a reduction in its steady component at a Reynolds number of  $5 \times 10^5$ , a phenomenon referred to as the drag crisis in the literature [25, 26, 30]. This phenomenon is well-documented in studies involving long cylinders, and it signifies the transition from a laminar to turbulent boundary layer. This reduction in drag is attributed to the turbulence in the boundary layer, which disrupts the formation of a stable and coherent wake behind the body. The turbulent fluctuations in the wake help to delay the separation of the boundary layer, resulting in a reduced drag on the body.

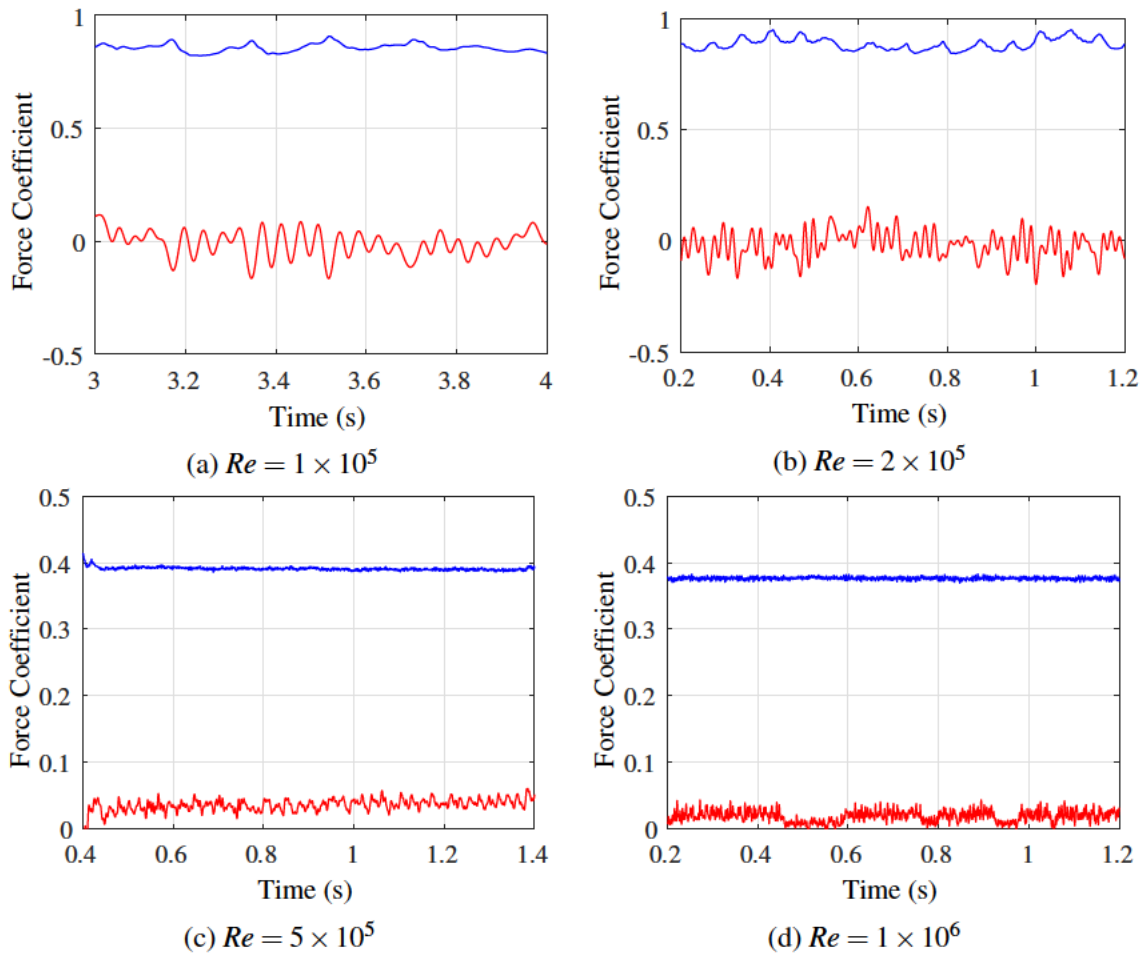


Figure 5.28: Plots of the lift (—) and drag (—) coefficients of the forces acting on the cylinder for various Reynolds numbers. Lift and drag are found using (3.21a) and (3.21b).

The phenomenon of vortex shedding is characterised by peak frequencies, which tend to shift towards higher frequencies as the Reynolds number increases as seen in Figure 5.29. Additionally, the amplitudes of all captured frequencies generally exhibit an upward trend. This shift towards higher frequencies holds significance in the calculation of the response of a solid thermowell, as it increases the likelihood of overlapping between exciting frequencies and the first modal frequency of the structure. Such overlap can result in substantial displacements in the structure, posing a risk of failure.



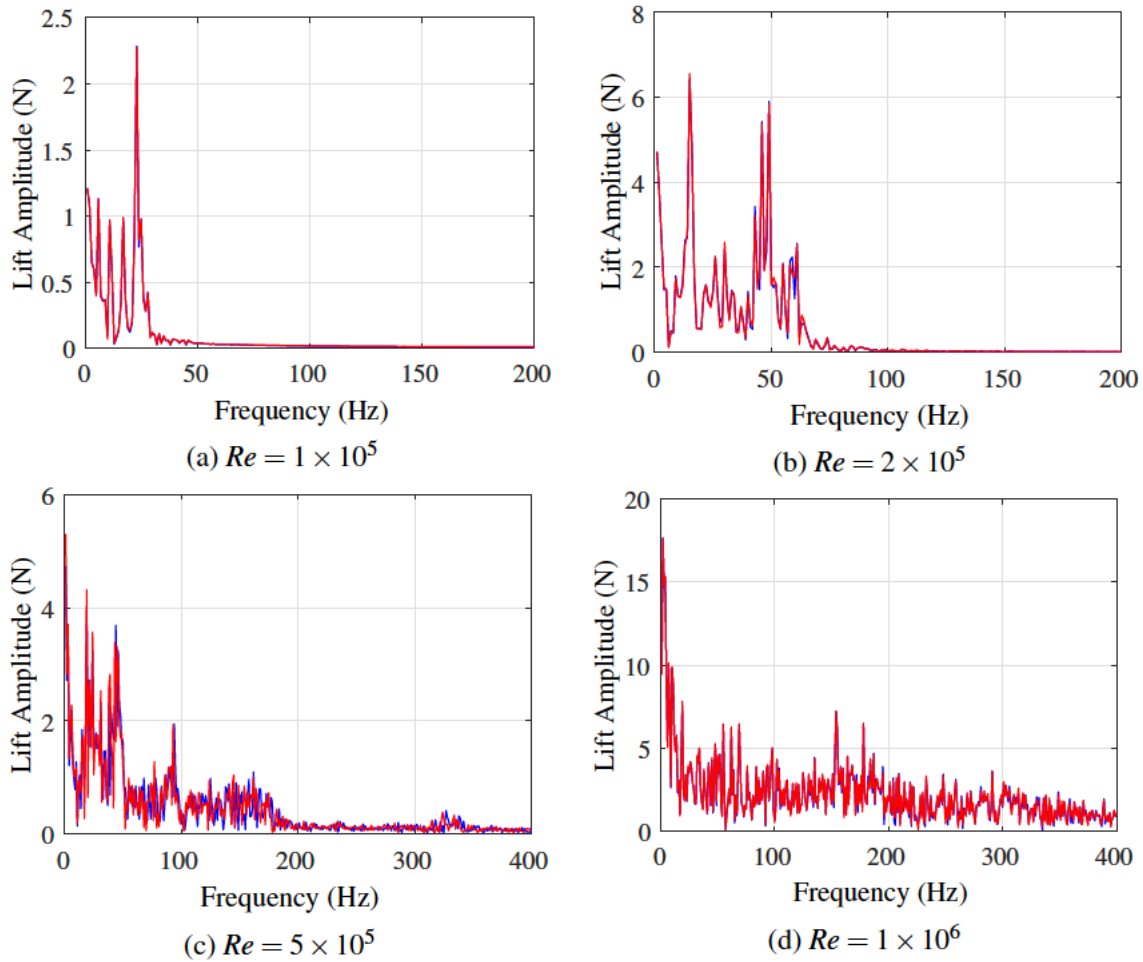


Figure 5.29: Plots of the discrete Fourier transform of the lift coefficient of the force acting on the cylinder before (—) and after interpolation (—) for various Reynolds numbers.

### Fluid Flow Metrics - Cylinder with Helical Strakes

The helical case was run at identical conditions to the straight cases and the lift, drag and total force were also observed before the displacement calculations were carried out. In the case of geometries with helical strakes, as seen in Figure 5.30, it is observed that the oscillations of lift and drag are significantly reduced compared to other cases. However, the average drag coefficient is increased, and it remains relatively constant with increasing Reynolds number as seen in [36]. The lift coefficient, on the other hand, oscillates around a non-zero value. The reduction in the oscillations of lift and drag can be attributed to the presence of helical strakes, which disrupt the formation of vortices and turbulence in the wake of the body. This results in a smoother flow around the body, leading to reduced oscillations in the lift and drag coefficients.

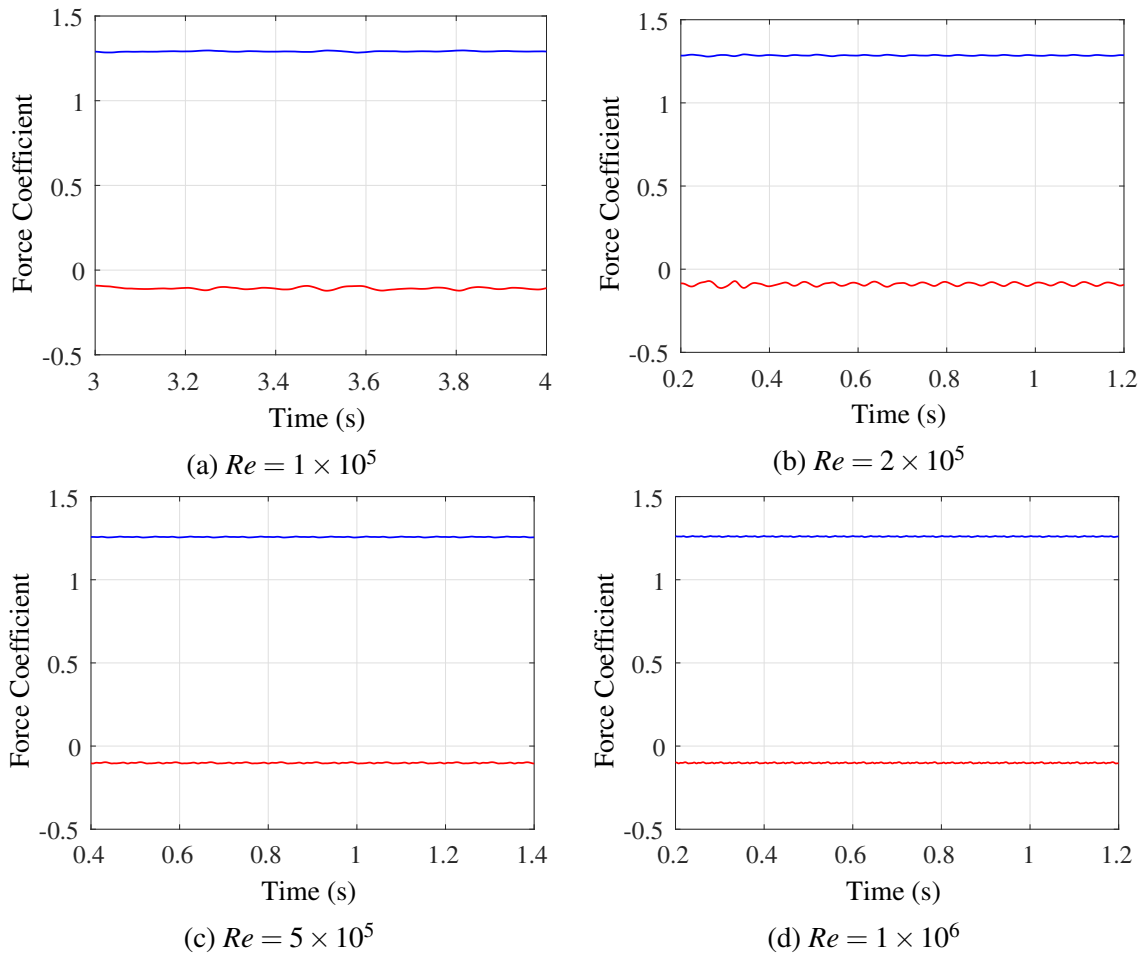


Figure 5.30: Plots of the lift (—) and drag (—) coefficients of the forces acting on the cylinder with helical strakes for various Reynolds numbers. Lift and drag are found using (3.21a) and (3.21b).

Despite the reduction in oscillations, the average drag coefficient is increased in the presence of helical strakes. This can be attributed to the additional drag generated by the presence of the helical strakes themselves, which disrupt the flow and create additional resistance. However, the average drag coefficient remains relatively constant with increasing Reynolds number, suggesting that the effect of the helical strakes on the drag is not significantly influenced by the flow regime. It is also noteworthy that the lift coefficient oscillates around a non-zero value, indicating that the presence of helical strakes introduces lift forces on the body even in the absence of large lift fluctuations. This suggests that the helical strakes have an effect on the lift generation of the body, possibly due to their shape and orientation in the flow. These observations highlight the complex aerodynamic behaviour of geometries with helical strakes, where the reduction in oscillations of lift and drag needs to be balanced against the increased average drag coefficient and the presence of lift forces.

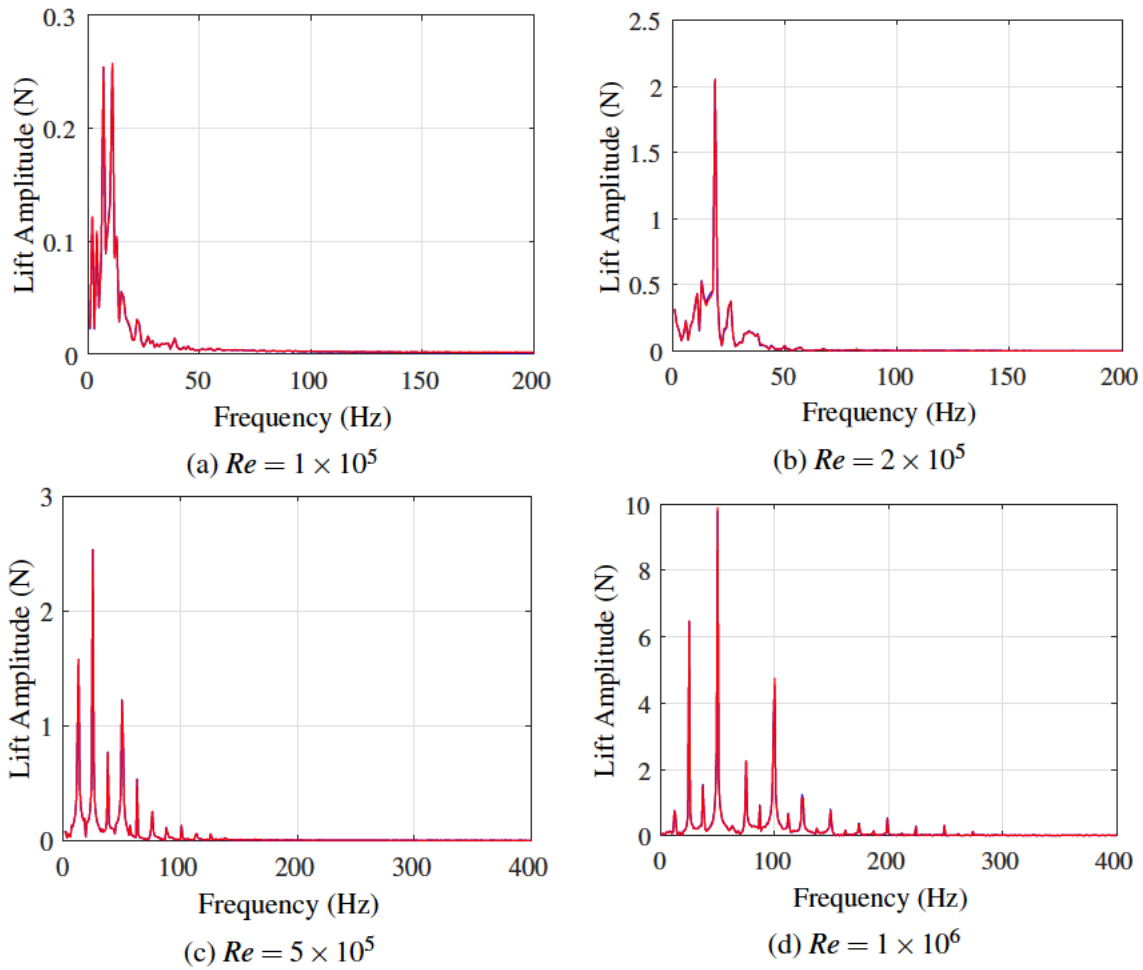


Figure 5.31: Plots of the discrete Fourier transform of the lift coefficient of the force acting on the cylinder before (—) and after interpolation (—) for various Reynolds numbers. Steady state term at 0 Hz is ignored for scaling.

The Fourier transform of the lift coefficient for geometries with helical strakes reveals peaks at lower frequencies and with smaller amplitudes compared to the plots obtained for the straight cylinder configuration. This can be observed in Figure 5.31. This observation suggests that the helical strakes have a dampening effect on the oscillations of the lift coefficient, resulting in lower frequency peaks and reduced amplitude compared to the case of a straight cylinder. The presence of helical strakes introduces additional flow disturbances and vortical structures in the wake of the body, which can alter the frequency and amplitude of the lift coefficient fluctuations. The lower frequency peaks in the Fourier transform of the lift coefficient indicate that the helical strakes affect the dominant frequency components of the flow-induced vibrations. The smaller amplitudes suggest that the helical strakes contribute to the reduction of lift fluctuations, potentially resulting in smoother and more stable aerodynamic behaviour compared to a straight cylinder.

## 5.2.2 Frequency Response of the Structure

In the case of the two geometries suggested, it is important to investigate the resonance response of the structure under the influence of the lower wake frequencies most likely to be excited. The structural response will be computed using the method outlined in Section 4.3. The application of the loading force on the boundary of the thermowells will be sampled from the fluid model and mapped using the NPIM.

## 5.2.3 Solid Solver Benchmarking

The solid solver will be benchmarked against the Newmark-beta method. In order to compare and benchmark the two solid solver methodologies the set up in Figure 5.32 was adopted. The discretisation of the structure is (20, 4, 2) elements and the dimensions of the structure is (1.0, 0.1, 0.05) with the units of meters. The Young's modulus, Poisson ratio and density used for these structures is 200 GPa, 0.3 and  $7850 \text{ kg m}^{-3}$  respectively as the study will replicate the material commonly used in thermowell manufacturing; stainless steel.

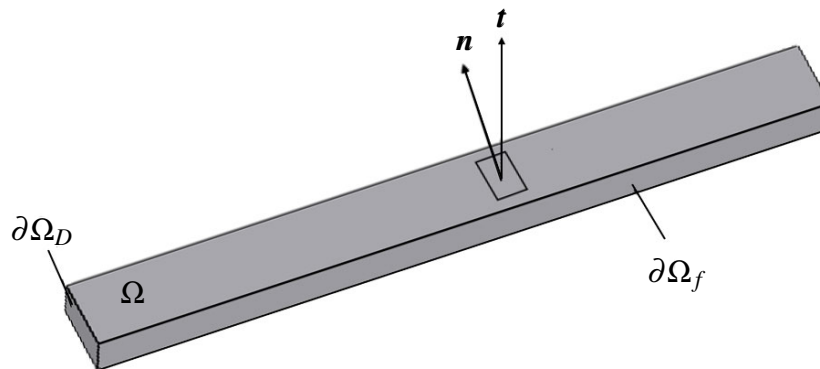


Figure 5.32: Solid domain  $\Omega$  used for the benchmarking for the reduced order solid solver. Displaying the Dirichlet boundary,  $\partial\Omega_D$ , with a fixed face and the face,  $\partial\Omega_f$ , receiving the known trial time varying force vectors.

The mode shapes of this structure, seen in Figure 5.33, were produced on SolidWorks as well as the values for the natural frequencies. In this case, damping is directly proportional to the stiffness matrix. This configuration essentially means that the damping in the system is solely based on the structural stiffness, and there is no contribution from the mass. It's worth noting that this damping model does not account for the mass-related damping, which is often present in physical systems. This choice might be suitable for certain applications, but it

may not represent realistic damping behaviour in many structural and mechanical systems and experimental tests would help configure a more realistic  $\alpha$  and  $\beta$ . Different combinations of  $\alpha$  and  $\beta$  in the Rayleigh damping matrix allow engineers to tailor the damping characteristics based on the specific requirements and characteristics of the structure under consideration. The damping seen in this example will be that of Rayleigh damping and more specifically proportional damping. This is where the coefficient  $\alpha = 0$  and  $\beta = 1$  in (4.17).

The accuracy of the proposed solution is demonstrated in Figure 5.34 where it is compared to a time integrator.

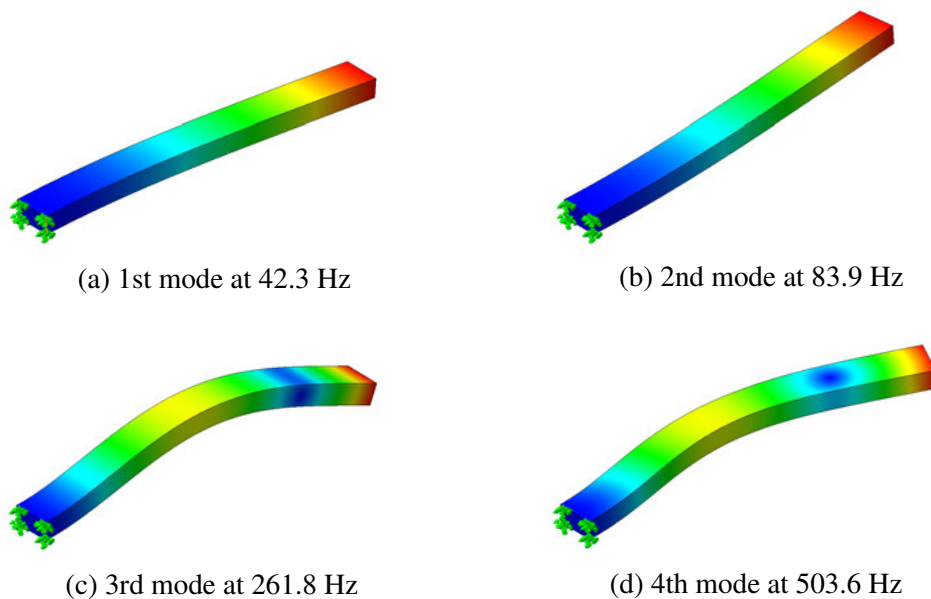


Figure 5.33: Mode shapes of the simple solid structure and the corresponding modal frequency with the displacement scaled by an arbitrary value.

It can be clearly observed that reducing the number of solved modes does not have a significant impact on the structural displacement until reaching a single mode. However, when solving for fewer than two modal frequencies and shapes, the error in displacements increases dramatically. This can be attributed to the fact that the exciting force oscillates at frequencies lower than the modal frequencies beyond the third shape, resulting in a lack of excitation for higher modes. As a result, these higher modes become less important to solve for. This can be observed in Figure 5.34.

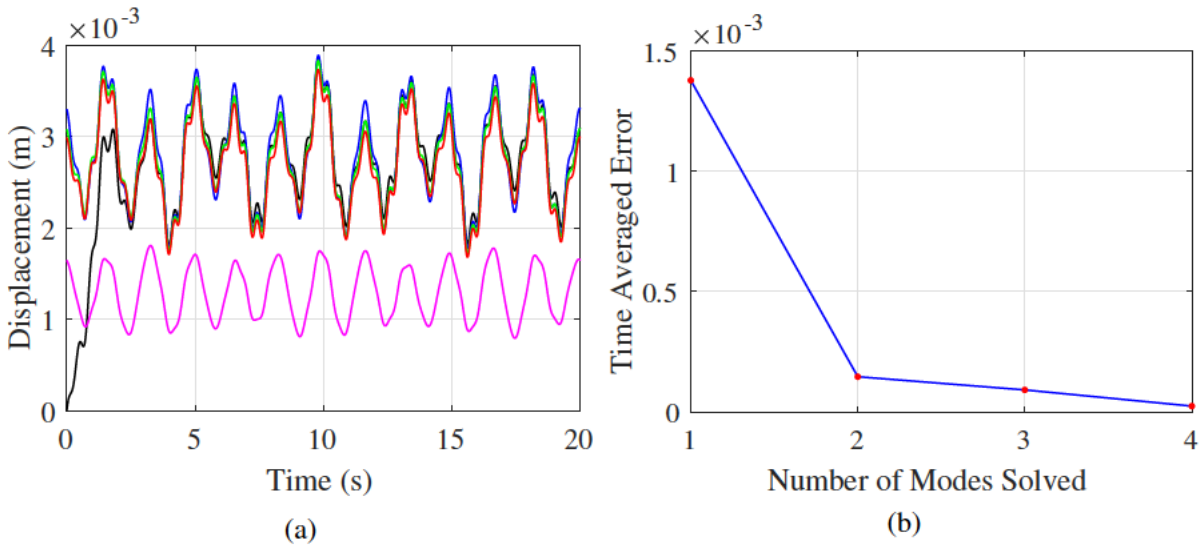


Figure 5.34: (a) Time history of a displacement of a solid structure while applying time varying arbitrary load. Solved using Newmark time integration (—) and then comparing by solving the FFT method for 4 modes (—), 3 modes (—), 2 modes (—), 1 modes (—) (b) The time averaged absolute error of the displacement of the selected node against how many modes are solved for.

### Mode shapes of the Thermowell Geometries

As seen in Figure 5.35 and Figure 5.36, only the first two modes are likely to be excited by the flow while the other modes are excited at far larger frequencies that are too large to capture with our current sampling. Therefore, an accurate solution for the structural response should be obtained while solving for just two modal contributions.

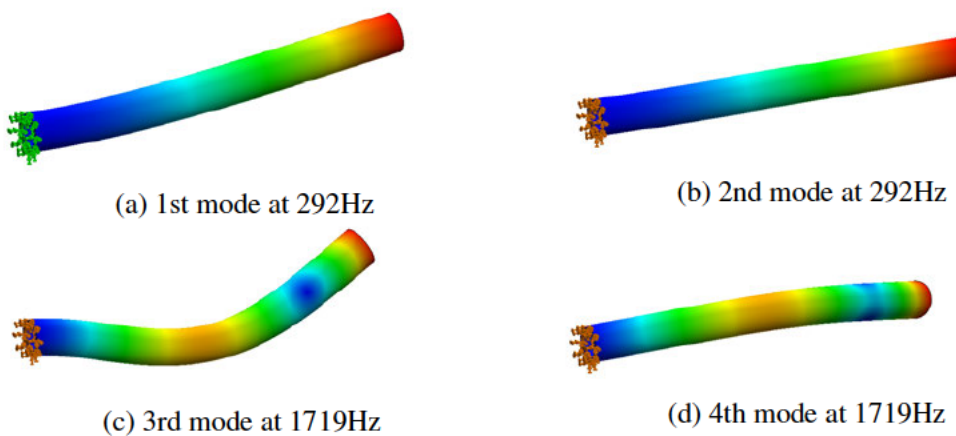


Figure 5.35: The first 4 mode shapes of the straight cylinder and the corresponding modal frequency with the displacement scaled by an arbitrary value.

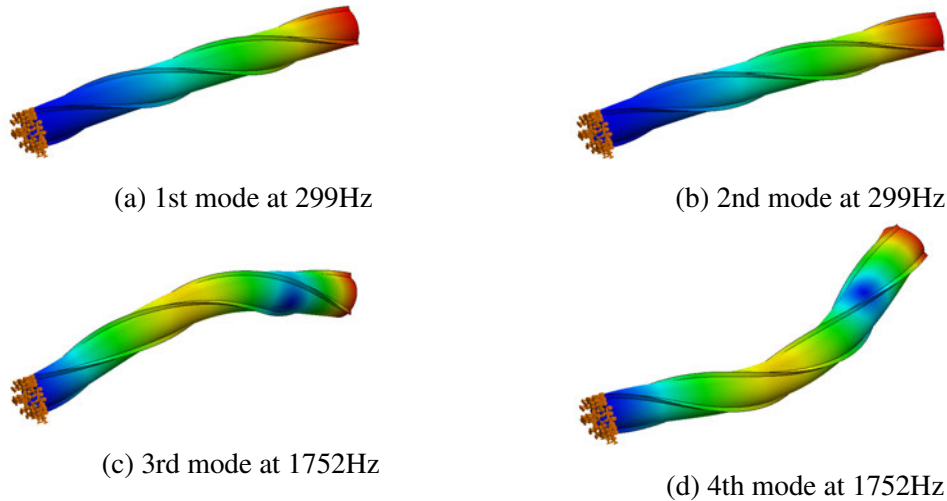


Figure 5.36: The first 4 mode shapes of the cylinder with helical strakes and the corresponding modal frequency with the displacement scaled by an arbitrary value.

Each of these natural frequencies were found on SolidWorks and were found using the eigenvalue problem described in (4.3). The natural frequencies are the square root of these eigenvalues.

### Solid Mesh Dependency Study when Mapping

A grid sizing study was conducted to gain confidence that the reduction in data has not greatly increased the error in the computation process due to the coarse discretisation. A selection of the force field applied to the thermowell wall at the time step at 2 seconds in the fluid simulation at Reynolds number  $1 \times 10^5$  was used to carry out this grid size study. The mesh study was conducted using the  $L^2$  of the force field, seen in (5.1),

$$\begin{aligned}
 L^2(f) &= \sqrt{\int_{\partial\Omega_f} f^2 d\Omega} \\
 &\approx \sqrt{\sum_{n=1}^N f_n^2 A_n},
 \end{aligned}
 \tag{5.1}$$

in the which  $N$  is the number of faces in the solid mesh interface and  $f$  is the force field. The interface has been characterised by the number of axial and angular division. These are uniformly spaced along one line of the axial length at a given angle and are not uniformly spaced for all angles around the cylinder. This is due to the fact that the divisions are defined by one axial line in the geometry and the Gmsh algorithm takes this transfinite curve and meshes test subject to this constraint. The metric used to compare the selection grids was the

L2-norm of the magnitude of force acting on each face. The results of the study are presented in Figure 5.37. Figure 5.37a demonstrates the convergence of the L2 norm relative to the number of axial divisions, showing a second-order convergence. In comparison, Figure 5.37b indicates a steeper gradient, suggesting that the L2 norm is more sensitive to angular divisions. Based on the results in Figure 5.37a, a suitable number of axial divisions was determined to be 120, which was then utilised in the subsequent test shown in Figure 5.37b. The L2 norm converges towards a constant value at 40 divisions, indicating that this value is appropriate for further analysis. In the simulation of fluid-structure interaction, the total force exerted on the cylinder by the fluid is a crucial quantity to analyse. It provides valuable insights into the effect of the fluid flow on the solid structure. For the straight cylinder, the total force is calculated separately for both the fluid and solid meshes, and the time history results are then plotted.

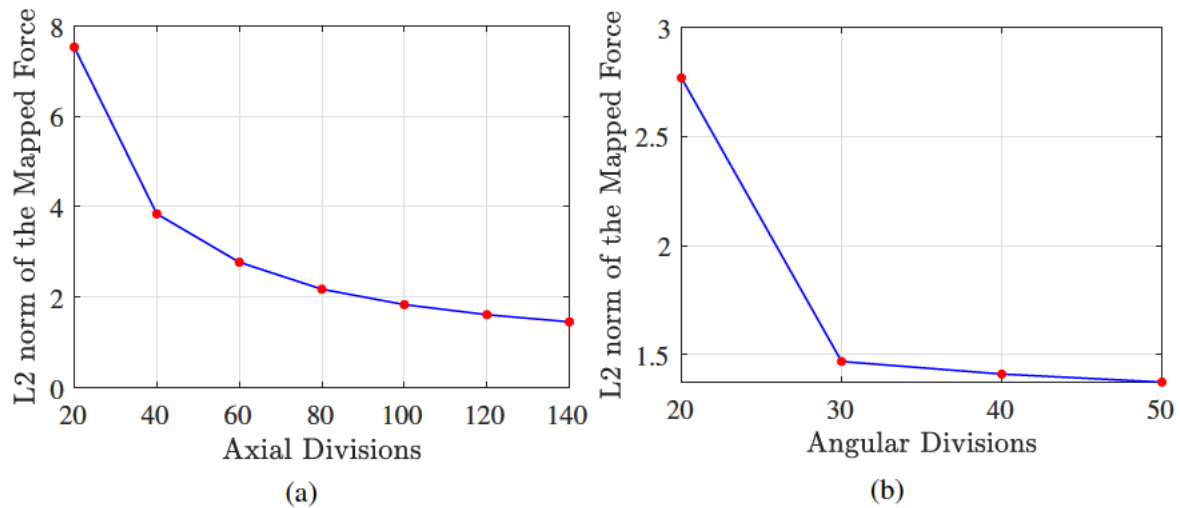


Figure 5.37: Plots of the results of a grid refinement study on the mapping process of fluid forces. (a) shows L2 vs axial divisions. (b) shows L2 vs circumferential divisions.

### Force Surface Field Sampling

The problem is set up as shown in Figure 5.38, with both a straight cylinder and a cylinder with helical strakes being under investigation.



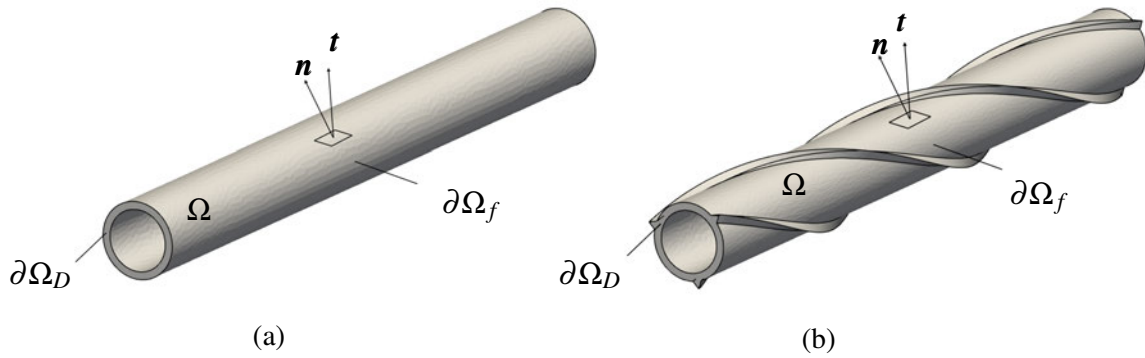


Figure 5.38: Solid domain displaying the hollow nature of the (a) straight cylinder (b) helical cylinder displaying Dirichlet boundary with a fixed condition  $\partial\Omega_D$  and the face at which the traction force is applied  $\partial\Omega_f$ .

For both cases of the straight cylinder and the cylinder with helical strakes the following settings are used for force sampling. In Table 5.9, it is observed that all cases have a frequency granularity of 1 Hz, which is a result of being sampled over a one-second period. The Nyquist frequency<sup>1</sup>, defined as the maximum frequency that a Fourier transform can accurately capture [79], is set to 200 Hz for the lower Reynolds numbers. The sampling time step was the amount of time between each force field sample to be applied to the solid. The corresponding sample frequency is given. These sample frequencies were chosen based to create a Nyquist frequency large enough to capture an estimated frequency of vortex shedding base of the corresponding Strouhal number for a straight cylinder (found in Figure 5.19a). Once the Strouhal number has been estimated for a given Reynolds number the estimated frequency of vortex shedding can be found using (2.2).

$Re$	$1 \times 10^5$	$2 \times 10^5$	$5 \times 10^5$	$1 \times 10^6$
Sampling time step	0.0025 s	0.0025 s	0.0005 s	0.0005 s
Sampling Frequency	400 Hz	400 Hz	2000 Hz	2000 Hz
Sampling time period	1 s	1 s	1 s	1 s
Step in frequency	1 Hz	1 Hz	1 Hz	1 Hz
Nyquist Frequency	200 Hz	200 Hz	1000Hz	1000 Hz

Table 5.9: Sampling settings of the force field acting on the thermowell surface for both geometrical variants.

<sup>1</sup>The minimum sampling rate must be at least twice that of the highest frequency component that one wishes to capture. Therefore Nyquist Frequency is the maximum frequency one can capture at a given sampling rate.

This frequency is sufficient to capture the desired information in those cases. However, for the larger Reynolds numbers, the sampling frequency is increased to achieve a Nyquist frequency of 1000 Hz. This higher Nyquist frequency ensures that any potential spikes in the frequency of vortex shedding are accurately captured and included in the analysis. The force field is sampled at the face centre of each element within the fluid mesh, followed by division by the element face area to obtain a traction vector. Subsequently, using the NPIM, these traction vectors are interpolated to the nearest face centres of the solid mesh and transformed into force vectors by multiplying them by the solid element's face area. These force vectors are then interpolated onto the nodes of the solid mesh, enabling the response to be solved.

The steady state component of the total force acting on the cylinder exhibits an increasing trend with Reynolds number, along with an increase in the amplitude of oscillation. Moreover, there is good agreement observed in the total force acting on the cylinder, indicating that the mapping technique used is conservative, i.e., it conserves the total force. The time history for the total force acting on the straight cylinder for the two extremes of Reynolds number are seen in Figure 5.39.

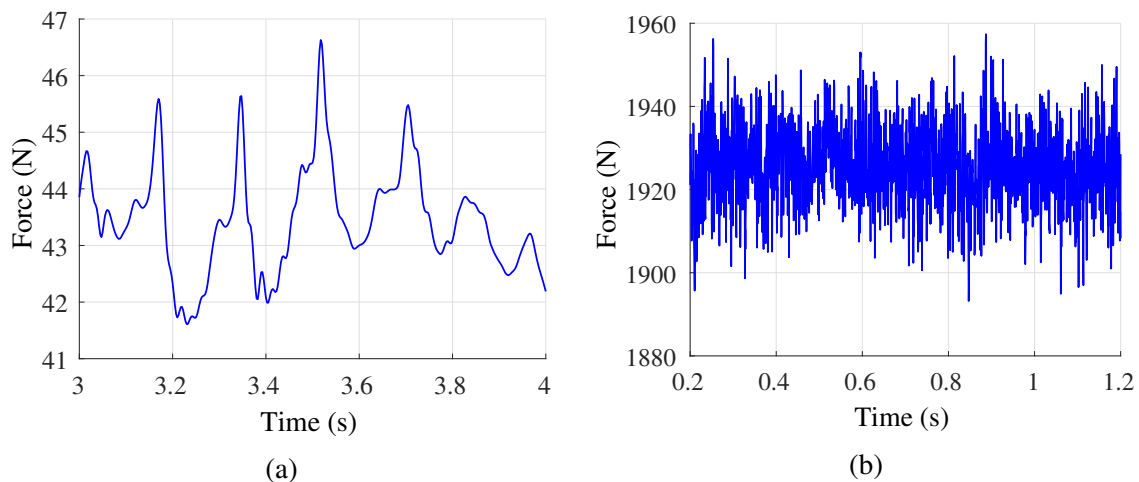


Figure 5.39: Plots of the total force acting on the cylinder after interpolation for Reynolds numbers (a)  $Re = 1 \times 10^5$  (b)  $Re = 1 \times 10^6$ .

Furthermore, it is observed that the error in the mapping can be reduced by coarsening the solid mesh, and in some cases, completely eliminated with the use of a conforming surface mesh on the outer surface of the geometry. This suggests that the mapping technique used for transferring the forces from the fluid domain to the solid domain is accurate and reliable, as it conserves the total force and can be further improved by adjusting the mesh properties. Coarsening of the solid mesh can be employed to reduce computational costs while maintaining

acceptable accuracy in the force calculations. Alternatively, using a conforming surface mesh on the exterior of the geometry can also help eliminate errors in the mapping, ensuring more accurate force predictions on the solid body.

In all cases studied, the magnitude of the relative error is observed to be consistently low as seen in Figure 5.40. This indicates that the mapping technique used for transferring forces from the fluid domain to the solid domain is highly accurate and reliable. The small absolute error signifies a close agreement between the predicted forces and the actual forces experienced by the solid body. The low magnitude of the relative error is a positive indication of the robustness and accuracy of the numerical simulation.

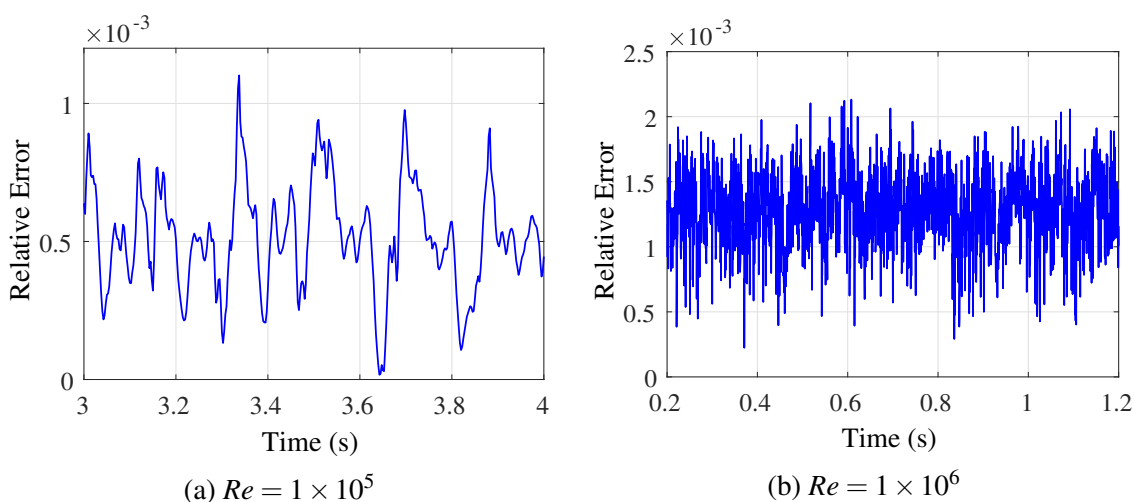


Figure 5.40: Plots of the absolute error of the total force generated by the nearest face mapping interpolation.

For the cylinder with helical strakes, the total force applied to the cylinder from the fluid is calculated for the solid mesh and the results are plotted in Figure 5.41. The mapping method is again displayed to be accurate and reliable in all cases studied indicated by the very low values of absolute error between the total force acting on the fluid mesh and the solid mesh seen in Figure 5.42.

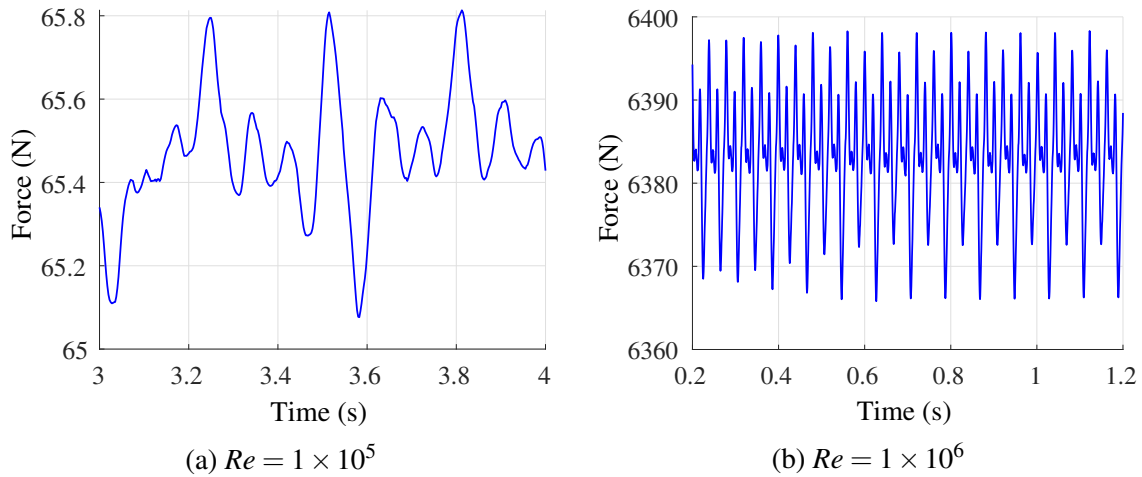


Figure 5.41: Plots of the total force acting on the cylinder with strake after interpolation for Reynolds numbers (a)  $Re = 1 \times 10^5$  (b)  $Re = 1 \times 10^6$ .

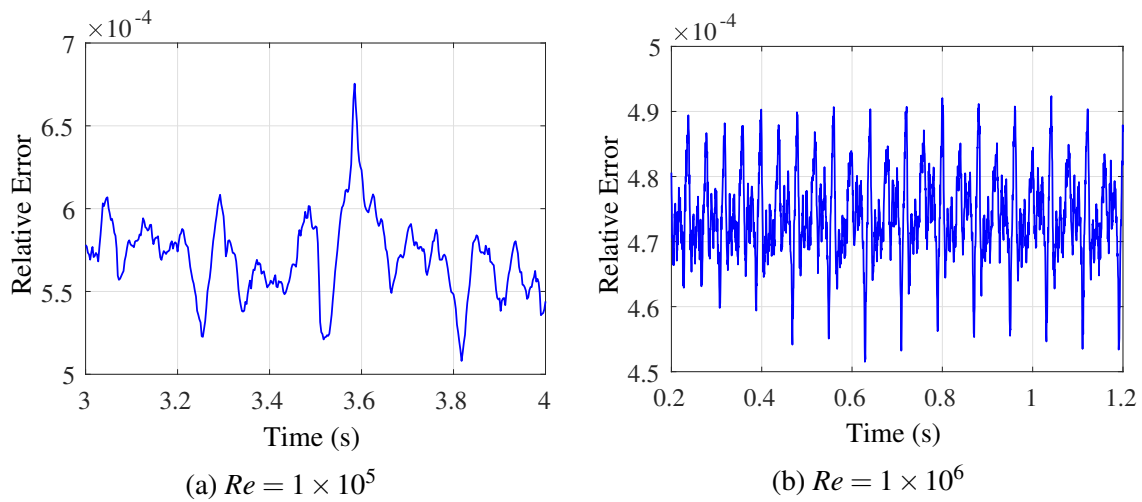


Figure 5.42: Plots of the residual error of the total force generated by the nearest face mapping interpolation for various Reynolds numbers.

## 5.2.4 Results of the Solid Solver

In Figure 5.43, it is evident that the steady-state displacement in helical cases surpasses that in straight cases, while the oscillation amplitudes are smaller in the helical instances. As shown in Figure 5.43, the steady-state displacement rises with Reynolds number for both straight and helical cylinders. However, oscillation amplitude increases only for helical cases with Reynolds number. Notably, in straight cases, there appears to be a dip in oscillation amplitude around a Reynolds number of  $5 \times 10^5$ . This may be attributed to the change in flow regime within and beyond this Reynolds number in the cylinder's boundary layer. The same trends can be seen in maximum von Mises stress of the cylinders in Figure 5.44. The maximum von Mises stress

of the structure was found using (4.30) after finding the stress tensor for each element from the displacement.

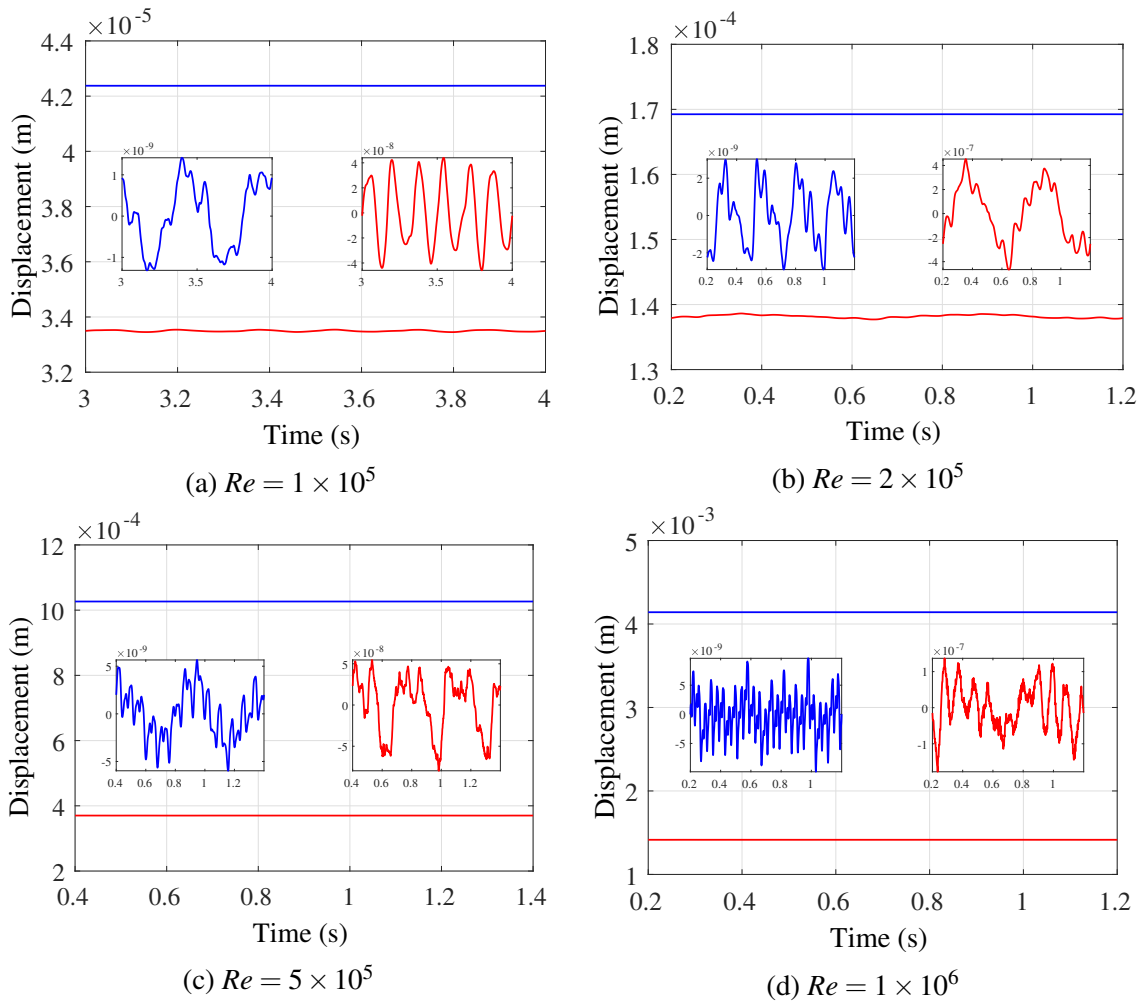


Figure 5.43: Plots of the displacement for a node at the tip of the straight (—) and helical (—) thermowells at the location (-0.15, 0, 300) for various Reynolds numbers. For each of these plots in the smaller windows had the constant component removed so they only display the oscillating component.

As seen in Figure 5.45 and Figure 5.46, the maximum von Mises stresses are seen at the base of the thermowell which can be of large complication when fixing a thermowell into a pipeline especially when welding. The weld may cause a weak point in the structure and be more susceptible to fatigue failure. Both of these snapshots are taken at the last time step of the simulations.

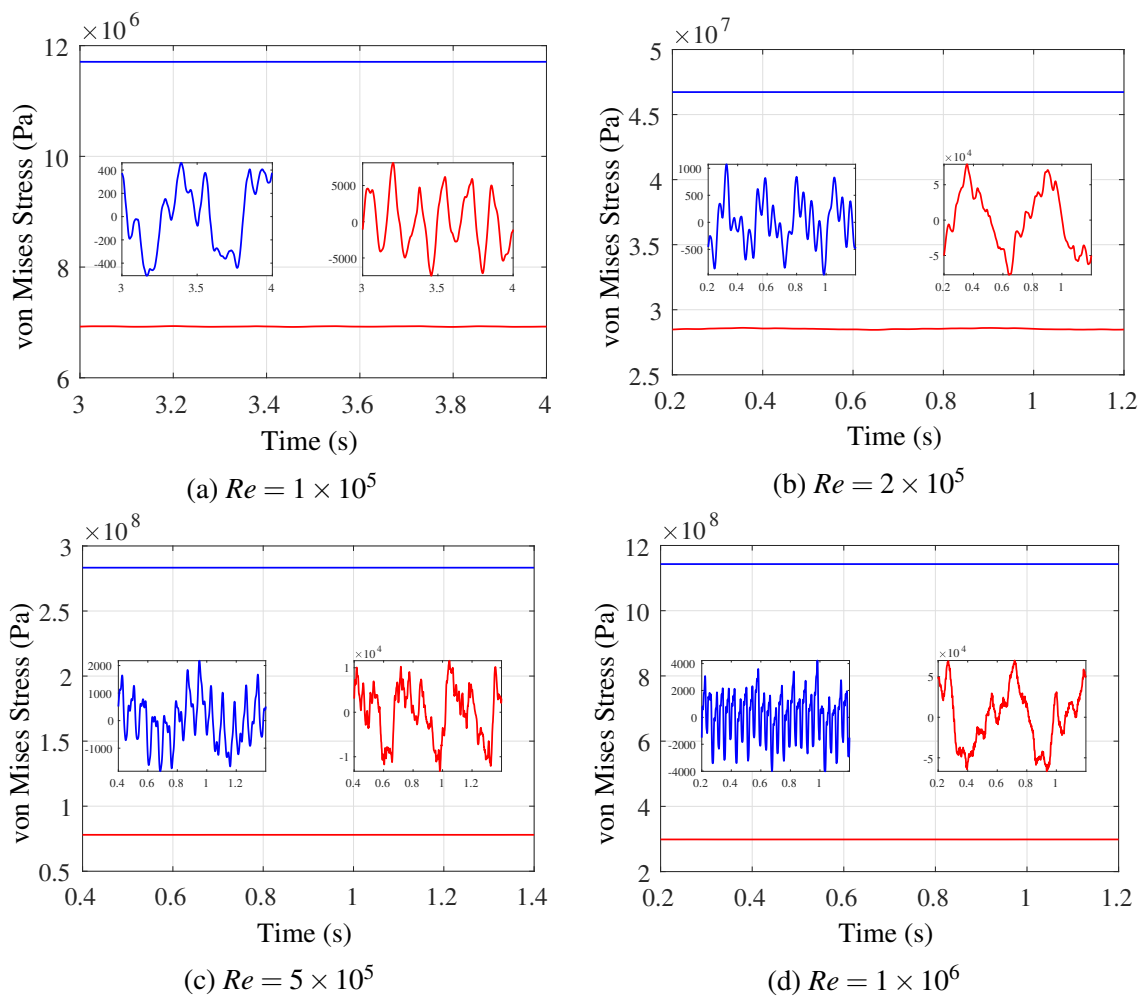


Figure 5.44: Plots of the von Mises stress at the base of the straight (—) and helical (—) thermowells at the location  $(-0.15, 0, 300)$  for various Reynolds numbers. For each of these plots in the smaller windows had the constant component removed so they only display the oscillating component.

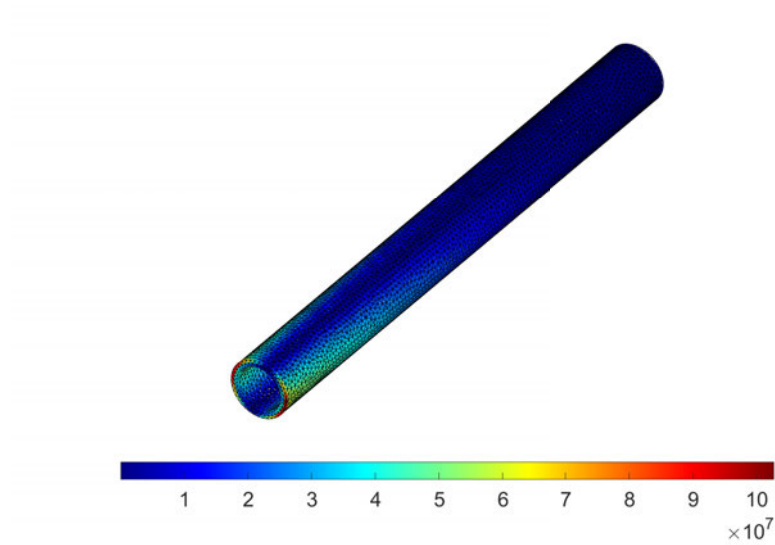


Figure 5.45: Plot of the contour plots of the von Mises stress of each element for a straight cylinder for a Reynolds number of  $5 \times 10^5$ . The units are in Pa

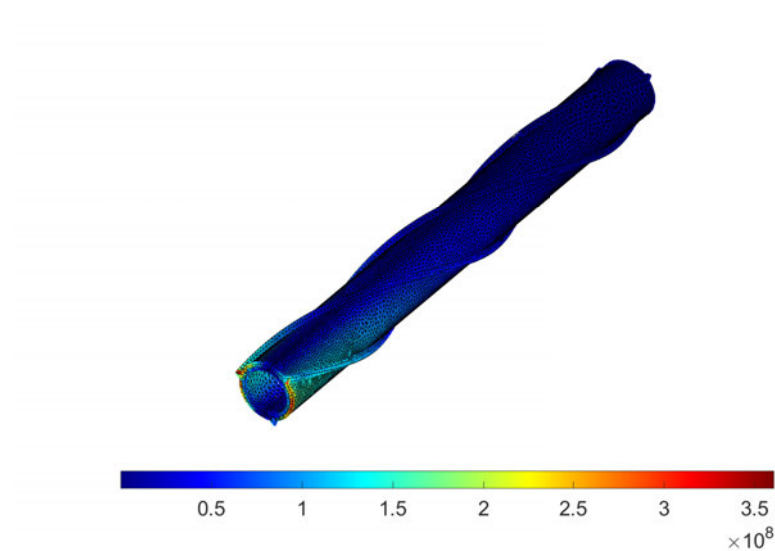


Figure 5.46: Plot of the contour plots of von Mises stress of each element for the cylinder with strakes for a Reynolds number of  $5 \times 10^5$ . The units are in Pa.

## 5.3 Discussion and Outputs

### 5.3.1 Significance of the Results

The 2D fluid results for Strouhal number vs Reynolds number shows an agreement between the Strouhal numbers obtained in the research and the analytical solution presented in ASME PTC 19.3 TW-2016, as determined by (2.2). Figure 5.10 presents the results of the 2D simulations, demonstrating a sufficient level of agreement between the obtained Strouhal numbers and the analytical solution. The findings not only align with the analytical solution but also replicate the results reported in previous works such as [31, 80], further substantiating the reliability and consistency of the obtained results. The benchmarking of the Strouhal number versus Reynolds number, as shown in Figure 5.19a, demonstrates sufficiently accurate results. However, when observing the lift and drag time history in the 3D results (seen in Figure 5.17), the change in regime that occurs between a Reynolds number of  $1 \times 10^5$  and  $1 \times 10^6$ , the convergence of oscillation is not as apparent as it is for lower Reynolds numbers. This could be due to the transitional nature of the flow changing between two regimes. Furthermore, Figure 5.19b illustrates a notable drop in average drag coefficient after a Reynolds number of  $1 \times 10^5$  indicating the occurrence of a drag crisis [26, 27, 81]. This serves as another indicator of the reliability of these simulations.

For straight cylinders of finite height, it is observed that there is no single dominant frequency for vortex shedding in the wake. Instead, the formation of vortices at the cylinder's tip and the horseshoe vortices at the bottom interfere with the overall turbulence around the structure, leading to a wide range of excited frequency values on the cylinder face. These other sources of vortex formations are further discussed in [33]. With higher Reynolds numbers, larger amplitudes of exciting forces are shifted towards higher frequencies.

When examining configurations involving helical strakes, it becomes evident that the fluctuations in lift and drag are notably diminished compared to other scenarios. Nonetheless, the average drag coefficient experiences an increase, and it maintains a relatively stable value as the Reynolds number rises, as documented in [36]. Conversely, the lift coefficient displays oscillations around a non-zero value. The decrease in lift and drag oscillations can be ascribed to the presence of helical strakes, which disrupt the formation of vortices and turbulence in the wake region behind the object. This disruption leads to a smoother flow pattern around the object, resulting in reduced oscillations in the lift and drag coefficients.



In the solid displacement analysis, displacements were calculated for all cases and Reynolds numbers. The steady-state displacement at the top of the helical thermowell was larger compared to the straight cylinder. However, the magnitude of oscillation in displacement was consistently larger for all Reynolds numbers meaning a steady state stress check is more likely to be the reason for failure in the helical thermowell than the dynamic stress check. Von Mises stresses were also evaluated based on the displacement data, with the maximum von Mises stress observed at the base of the structure in both cases. This finding holds particular significance for welded thermowells, highlighting the critical stress concentration points. The steady-state maximum von Mises stress was larger for the helical structure for all Reynolds numbers, while the oscillatory component of the maximum von Mises stress was larger for the straight thermowells across all Reynolds numbers.

# Chapter 6

## Conclusions

The concluding chapter of this thesis serves as a comprehensive summary of the research findings and aims to draw insightful conclusions that contribute to a better understanding of the overall outcome of the study. It encapsulates the key discoveries, analyses, and results obtained throughout the research process, providing an overview of the significant contributions made in the field.

### 6.1 Completion of Research Objectives

In this section, conclusions are made on this work in the fields of computational analysis, fluid dynamics, and experimental validation. The following points highlight key contributions and methodologies from this work.

#### Assessment of Industry Standards

This thesis offers an overview of current industry standards governing the prediction of thermowell structural responses in flow processes. It delineates the calculations included in thermowell sizing according to ASME PTC 19.3 TW-2016 standards. A review of the assumptions underpinning industry standards was conducted to discern potential approximations and errors introduced in the calculations. These assumptions involve neglecting the effects of flow over the thermowell tip and utilising fixed lift and drag coefficients, thereby disregarding changes in the turbulent regime. Such assumptions may result in inaccuracies when predicting thermowell behaviour in real-world applications. Furthermore, variations in the Strouhal number beyond  $5 \times 10^5$ , noted in certain literature sources, are overlooked

and instead assumed to remain constant. The thesis achieves the first objective set in 1.5.1. Limitations exist that hinder the effective adoption of innovative designs, as industry standards strictly adhere to the assumption that thermowell designs feature either a straight, tapered, or stepped stem.

### **A Novel Time Efficient Workflow**

This workflow is carried out by the use of open-source software, making it cost-effective. The utilisation of a frequency-based modal superposition method offers substantial improvements in efficiency compared to traditional time-based structural solvers. The one-way nature of the FSI coupling also reduces the computational cost compared to strong coupling. This achieves the second objective set in 1.5.1.

### **Mapping Technique for Boundary Force Loads**

This technique has been developed and validated using a nearest point interpolation method. This method proves to be computationally inexpensive and time-efficient.

### **Validation of the Flow Simulation Methods**

In this case, the validation process involves benchmarking against experimental data from the literature using key metrics such as the average drag coefficient and the Strouhal number. This ensures the accuracy and reliability of the flow simulation methods employed. Furthermore, this validation is particularly relevant to the study of vortex shedding phenomena around straight cylinders and the analysis of Kármán vortex streets.

### **Capability to Predict the Effect of Surface Flow Disrupter**

This has been carried out by the use of numerical simulation via a one-way FSI study although the effect of the flow disrupter can be seen by only looking at the flow metrics as the oscillations of lift and drag are significantly reduced with the introduction of a surface flow disrupter in the form of three helical strakes. Solid displacement analysis revealed larger steady-state displacements at the top of helical thermowells in comparison to straight thermowells over the range of Reynolds numbers investigated. However, straight thermowells displayed consistently larger oscillation amplitudes across all Reynolds numbers. Von Mises stresses, calculated from these displacements, showed the highest stress at the base for both

types. Notably, the steady-state maximum von Mises stress was larger for helical structures over all Reynolds numbers with oscillatory amplitudes in the stresses.

### **Experimental Method for New Geometries**

The presentation of an experimental method to supplement the assessment of new geometries. The development of dedicated apparatus and consideration of flow conditions ensure the creation of a reliable testing framework for evaluating thermowell use. This approach allows researchers to experimentally validate the performance and behaviour of novel geometries. The combination of numerical simulations and experimental testing enhances the overall understanding and validation of new engineering solutions. The thesis achieves the final objective set in 1.5.1.

The reduced order model estimates smaller steady state von Mises and oscillatory stress than that of the industry standards at the higher Reynolds number which could allow thermowells that currently fail the criteria to now pass. This could be a concern when considering the safety risk. Further validation would be needed experimentally in order to gain confidence.

## **6.2 Closure of the Work**

The significance of this work extends beyond factual observations as it addresses limitations in existing standards that stifle innovation by prescribing fixed-form cylindrical thermowell designs. Through numerical analysis, our study demonstrates the feasibility of developing an efficient framework to characterise thermowell responses, facilitating optimisation of structural properties under dynamic fluid excitation and enabling the exploration of novel design possibilities.

## **6.3 Future Work**

This section will explore potential avenues for future research and studies that can enhance the methodology for predicting the behaviour of thermowells placed in flowing fluids were explored. Furthermore, the opportunities to further benchmark and validate the findings

presented in this current work were discussed. Throughout this work, numerous new research opportunities have been identified. These are:

1. Construction of an experimental setup for testing helical thermowells vs straight thermowells in extreme conditions and turbulence: In this step, the experimental rig and apparatus outlined in Section 2.2 to simulate extreme conditions and turbulence could be constructed. The objective is to compare the performance of helical thermowells with straight thermowells under these conditions. You would install both types of thermowells, collect data on structural response.
2. Exploring additional simulations to analyse the impact of different turbulence models and wall functions on flow parameters. Consideration of alternative models like LES at higher Reynolds numbers. Expanding the benchmarking efforts for this specific turbulence regime. The use of a different turbulence model may need to be utilised in order to capture this region accurately. The use of LES for flow around a bare cylinder is often used in literature where large Reynolds numbers in this regime are found [25–27].
3. Development of a two-way FSI problem to model the 'lock-in' region of frequencies close to the natural frequency of the thermowell: Fluid-Structure Interaction refers to the interaction between a fluid flow and the thermowell. The 'lock-in' phenomenon occurs when the frequency of the flow-induced vibrations matches the natural frequency of the thermowell, leading to significant vibrations and potential failure. To gain a deeper understanding of this phenomenon, you would develop a computational model that incorporates the fluid flow and structural dynamics of the thermowell. By varying the flow parameters, analysing the response of the thermowell, and studying the 'lock-in' region, you can gain insights into the physics behind this phenomenon and potentially develop strategies to mitigate its effects.
4. Testing further designs of the thermowell surfaces to break up turbulence at the boundary layer: By modifying the surface design of the thermowell, such as introducing specific features or textures, it may be possible to disrupt or break up the turbulent flow within the boundary layer. This step involves designing alternative thermowell surface configurations, which can include grooves, roughness elements, or other geometrical modifications. Experimental or computational tests would then be conducted to assess the effectiveness of these designs in reducing turbulence and enhancing the overall

performance of the thermowell. The goal is to find surface designs that effectively break up the turbulence at the boundary layer and improve the accuracy and reliability of temperature measurements.

5. Gain a further insight into how the surface layer may affect temperature measurement lags. One may perform experiments or simulations to analyse the behaviour of different surface configurations and their impact on temperature measurement accuracy and response time.

# References

- [1] A. I. Karayan, Y. Pratesa, A. Ashari, and D. Ferdian, “Fatigue failure of flanged thermowell,” *Journal of failure analysis and prevention*, vol. 11, pp. 487–492, 2011.
- [2] Science and Technology Agency, Tokyo (Japan). Nuclear Safety Bureau, “A report on investigation into the sodium leakage accident at prototype fast breeder reactor is issued,” *Science and Technology in Japan*, vol. 14, no. 56, pp. 42–51, 1996.
- [3] T. A. S. of Mechanical Engineers, “ASME PTC 19.3 TW-2016. Thermowells - Performance Test Codes,” 2016.
- [4] T. A. S. of Mechanical Engineers, “ASME PTC 19.3 TW-2010. Thermowells - Performance Test Codes,” 2010.
- [5] D. Bauschke, D. Wiklund, A. Kitzman, and D. Zulic, “Thermowell calculations,” *Emerson Process Management, White Paper*, vol. 840, pp. 0200–2654, 2014.
- [6] R. Leino, “When and when not to use thermowells in process temperature measurement,” *Processing*, 2018.
- [7] V. Sharma, “Tempsens - Thermowells.” <https://tempsens.com/blog/thermowells>, Mar 2021. Accessed: 2021-03-30.
- [8] S. Rajagopalan and R. A. Antonia, “Flow around a circular cylinder—structure of the near wake shear layer,” *Experiments in fluids*, vol. 38, pp. 393–402, 2005.
- [9] J. H. Gerrard, “The mechanics of the formation region of vortices behind bluff bodies,” *Journal of Fluid Mechanics*, vol. 25, no. 2, p. 401–413, 1966.
- [10] T. Von Kármán, *Aerodynamics*. McGraw-Hill paperbacks : Science, mathematics and engineering, McGraw-Hill, 1963.

- [11] R. Skop and O. Griffin, "A model for the vortex-excited resonant response of bluff cylinders," *Journal of Sound and Vibration*, vol. 27, no. 2, pp. 225–233, 1973.
- [12] J. K. Vandiver, S. B. Swithenbank, V. Jaiswal, and V. Jhingran, "Fatigue damage from high mode number vortex-induced vibration," in *International Conference on Offshore Mechanics and Arctic Engineering*, vol. 47497, pp. 803–811, 2006.
- [13] G. S. Baarholm, C. M. Larsen, and H. Lie, "On fatigue damage accumulation from in-line and cross-flow vortex-induced vibrations on risers," *Journal of Fluids and Structures*, vol. 22, no. 1, pp. 109–127, 2006.
- [14] S. Kim, M. M. Alam, H. Sakamoto, and Y. Zhou, "Flow-induced vibration of two circular cylinders in tandem arrangement. part 2: Suppression of vibrations," *Journal of wind engineering and industrial aerodynamics*, vol. 97, no. 5-6, pp. 312–319, 2009.
- [15] S. Dai, B. A. Younis, H. Zhang, and C. Guo, "Prediction of vortex shedding suppression from circular cylinders at high Reynolds number using base splitter plates," *Journal of Wind Engineering and Industrial Aerodynamics*, vol. 182, pp. 115–127, 2018.
- [16] F.-B. Tian, H. Dai, H. Luo, J. F. Doyle, and B. Rousseau, "Fluid–structure interaction involving large deformations: 3d simulations and applications to biological systems," *Journal of computational physics*, vol. 258, pp. 451–469, 2014.
- [17] S. Behara and S. Mittal, "Transition of the boundary layer on a circular cylinder in the presence of a trip," *Journal of Fluids and Structures*, vol. 27, no. 5-6, pp. 702–715, 2011.
- [18] C. H. Williamson, "Vortex dynamics in the cylinder wake," *Annual review of fluid mechanics*, vol. 28, no. 1, pp. 477–539, 1996.
- [19] T. Sato, Masami, Kobayashi, "A fundamental study of the flow past a circular cylinder using Abaqus/CFD," *2012 SIMULIA Community Conference*, pp. 1–15, 2012.
- [20] A. Placzek, J. F. Sigrist, and A. Hamdouni, "Numerical simulation of an oscillating cylinder in a cross-flow at low Reynolds number: Forced and free oscillations," *Computers and Fluids*, vol. 38, no. 1, pp. 80–100, 2009.



- [21] E. Guilmineau and P. Queutey, "A numerical simulation of vortex shedding from an oscillating circular cylinder," *Journal of Fluids and Structures*, vol. 16, no. 6, pp. 773–794, 2002.
- [22] P. Mathupriya, L. Chan, H. Hasini, and A. Ooi, "Numerical study of flow characteristics around confined cylinder using openFOAM," *International Journal of Engineering and Technology(UAE)*, vol. 7, no. 4, pp. 617–623, 2018.
- [23] H. Blackburn and R. Henderson, "Lock-in behavior in simulated vortex-induced vibration," *Experimental Thermal and Fluid Science*, vol. 12, no. 2, pp. 184–189, 1996.
- [24] R. T. Hartlen and I. G. Currie, "Lift-oscillator model of vortex-induced vibration," *Journal of the Engineering Mechanics Division*, vol. 96, no. 5, pp. 577–591, 1970.
- [25] O. Lehmkuhl, I. Rodríguez, R. Borrell, J. Chiva, and A. Oliva, "Unsteady forces on a circular cylinder at critical Reynolds numbers," *Physics of Fluids*, vol. 26, no. 12, 2014.
- [26] H. Ye and D. Wan, "Benchmark computations for flows around a stationary cylinder with high reynolds numbers by RANS-overset grid approach," *Applied Ocean Research*, vol. 65, pp. 315–326, 2017.
- [27] P. Catalano, M. Wang, G. Iaccarino, and P. Moin, "Numerical simulation of the flow around a circular cylinder at high Reynolds numbers," *International journal of heat and fluid flow*, vol. 24, no. 4, pp. 463–469, 2003.
- [28] I. Rodríguez, O. Lehmkuhl, J. Chiva, R. Borrell, and A. Oliva, "On the flow past a circular cylinder from critical to super-critical Reynolds numbers: Wake topology and vortex shedding," *International Journal of Heat and Fluid Flow*, vol. 55, pp. 91–103, 2015.
- [29] C. Moussaed, M. V. Salvetti, S. Wornom, B. Koobus, and A. Dervieux, "Simulation of the flow past a circular cylinder in the supercritical regime by blending RANS and variational-multiscale LES models," *Journal of Fluids and Structures*, vol. 47, pp. 114–123, 2014.
- [30] P. W. Bearman, "On vortex shedding from a circular cylinder in the critical Reynolds number régime," *Journal of Fluid Mechanics*, vol. 37, no. 3, pp. 577–585, 1969.

- [31] M. Thompson, K. Hourigan, and J. Sheridan, “Three-dimensional instabilities in the wake of a circular cylinder,” *Experimental Thermal and Fluid Science*, vol. 12, no. 2, pp. 190–196, 1996.
- [32] H. B. Chan, T. H. Yong, P. Kumar, S. K. Wee, and S. S. Dol, “The numerical investigation on the effects of aspect ratio and cross-sectional shape on the wake structure behind a cantilever,” *ARPJ Journal of Engineering and Applied Sciences*, vol. 11, no. 16, pp. 9922–9932, 2016.
- [33] G. Palau-Salvador, T. Stoesser, J. Fröhlich, M. Kappler, and W. Rodi, *Large eddy simulations and experiments of flow around finite-height cylinders*, vol. 84. 2010.
- [34] S. Kornet, D. Sławiński, P. Ziółkowski, and J. Badur, “Analysis of unsteady flow forces on the thermowell of steam temperature sensor,” *Transactions of the Institute of Fluid-Flow Machinery*, vol. nr 129, no. 129, pp. 25–49, 2015.
- [35] E. Ranjith, A. Sunil, and L. Pauly, “Analysis of Flow over a Circular Cylinder Fitted with Helical Strakes,” *Procedia Technology*, vol. 24, pp. 452–460, 2016.
- [36] Y. Constantinides and O. H. Oakley, “Numerical prediction of bare and straked cylinder VIV,” *Proceedings of the International Conference on Offshore Mechanics and Arctic Engineering - OMAE*, vol. 2006, pp. 1–9, 2006.
- [37] H. Baek and G. E. Karniadakis, “Suppressing vortex-induced vibrations via passive means,” *Journal of Fluids and Structures*, vol. 25, no. 5, pp. 848–866, 2009.
- [38] Imperial College London and University of Utah, “Nektar++.”
- [39] A. Pinto, R. Brogna, E. Ciappi, A. Di Mascio, E. F. Campana, and P. Rocco, “Vortex suppression efficiency of discontinuous helicoidal fins,” *Proceedings of the International Conference on Offshore Mechanics and Arctic Engineering - OMAE*, vol. 3, pp. 813–820, 2007.
- [40] R. Brogna and A. Di Mascio, “Unsteady RANS calculations of the flow around a moving ship hull,” in *Proc. 8th Int. Conf. on Num. Ship Hydro., Busan, Korea, 2003*.
- [41] OpenCFD Ltd, “Openfoam.”

- [42] B. S. Carmo, G. R. Assi, and J. R. Meneghini, “Computational simulation of the flow-induced vibration of a circular cylinder subjected to wake interference,” *Journal of Fluids and Structures*, vol. 41, pp. 99–108, 2013.
- [43] M. S. Zakaria, H. Abdullah, and K. A. Ahmad, “Fluid structure interaction simulation of large deformation and added-mass effect using openfoam,” *Proceedings of Mechanical Engineering Research Day 2018*, vol. 2018, pp. 79–80, 2018.
- [44] C. Stefanini, F. Giorgetti, A. Mercuri, A. Facci, and P. Fanelli, “Cylinder-lamina system fluid–structure interaction problem solved with an original openfoam code,” *Journal of Computational Science*, vol. 54, p. 101420, 2021.
- [45] M. Zhang, G. Hu, and J. Wang, “Bluff body with built-in piezoelectric cantilever for flow-induced energy harvesting,” *International Journal of Energy Research*, vol. 44, no. 5, pp. 3762–3777, 2020.
- [46] J. Lorentzon, “Fluid-structure interaction (FSI) case study of a cantilever using openFOAM and DEAL. II with application to VIV,” 2009.
- [47] E. Ferhatoglu, E. Cigeroglu, and H. N. Özgüven, “A new modal superposition method for nonlinear vibration analysis of structures using hybrid mode shapes,” *Mechanical Systems and Signal Processing*, vol. 107, pp. 317–342, 2018.
- [48] K. Wijesooriya, D. Mohotti, A. Amin, and K. Chauhan, “Comparison between an uncoupled one-way and two-way fluid structure interaction simulation on a super-tall slender structure,” *Engineering Structures*, vol. 229, p. 111636, 2021.
- [49] T. Nishihara, S. Kaneko, and T. Watanabe, “Characteristics of fluid dynamic forces acting on a circular cylinder oscillated in the streamwise direction and its wake patterns,” *Journal of Fluids and Structures*, vol. 20, no. 4 SPEC. ISS., pp. 505–518, 2005.
- [50] D. Sumner, J. L. Heseltine, and O. J. P. Dansereau, “Wake structure of a finite circular cylinder of small aspect ratio,” *Experiments in Fluids*, vol. 37, no. 5, pp. 720–730, 2004.
- [51] A. Okajima, A. Nakamura, T. Kosugi, H. Uchida, and R. Tamaki, “Flow-induced in-line oscillation of a circular cylinder,” *European Journal of Mechanics, B/Fluids*, vol. 23, no. 1, pp. 115–125, 2004.

- [52] J. Sui, J. Wang, S. Liang, and Q. Tian, "VIV suppression for a large mass-damping cylinder attached with helical strakes," *Journal of Fluids and Structures*, vol. 62, pp. 125–146, 2016.
- [53] T. Zhou, S. F. Razali, Z. Hao, and L. Cheng, "On the study of vortex-induced vibration of a cylinder with helical strakes," *Journal of Fluids and Structures*, vol. 27, no. 7, pp. 903–917, 2011.
- [54] T. Knight, "Revised final test report: Tests of orbital/daily ve helical strake thermowells," pp. 1–37, 2017.
- [55] W. K. Lee, "Evaluation Report : Theromwell Validation Tests VortexWell," no. December, 2012.
- [56] R. D. Blevins, "Models for vortex-induced vibration of cylinders based on measured forces," *Journal of Fluids Engineering, Transactions of the ASME*, vol. 131, no. 10, pp. 1012031–1012039, 2009.
- [57] N. D. Katopodes, *Free-Surface Flow:: Shallow Water Dynamics*. Butterworth-Heinemann, 2018.
- [58] A. Roshko, "Experiments on the flow past a circular cylinder at very high Reynolds number," *Journal of fluid mechanics*, vol. 10, no. 3, pp. 345–356, 1961.
- [59] S. Zhou, Y. Zou, X. Hua, F. Xue, and X. Lu, "Investigation of the scruton number effects of wind-induced unsteady galloping responses of bridge suspenders," *Shock and Vibration*, vol. 2021, pp. 1–11, 2021.
- [60] T. Knight, A. Wimpenny, and Z. He, "Elimination of vortex induced vibration in sample probes and thermowells using helical strakes ; a report on the development , testing and proving of a helical design,"
- [61] A. H. Lee, R. L. Campbell, and S. A. Hambric, "Coupled delayed-detached-eddy simulation and structural vibration of a self-oscillating cylinder due to vortex-shedding," *Journal of Fluids and Structures*, vol. 48, pp. 216–234, 2014.

- [62] J. H. Lienhard *et al.*, *Synopsis of lift, drag, and vortex frequency data for rigid circular cylinders*, vol. 300. Technical Extension Service, Washington State University Pullman, WA, 1966.
- [63] M. Alziadeh, *Flow-sound Interaction Mechanism of a Single Spirally Finned Cylinder in Cross-Flow*. PhD thesis, 08 2017.
- [64] R. Panton, *Incompressible Flow*. Developmental clinical psychology and psychiatry, Wiley, 1996.
- [65] J. Anderson, *Computational Fluid Dynamics: The Basics with Applications*. McGraw-Hill International Editions: Mechanical Engineering, McGraw-Hill, 1995.
- [66] C. Hirsch, *Numerical computation of internal and external flows: The fundamentals of computational fluid dynamics*. Elsevier, 2007.
- [67] F. R. Menter, M. Kuntz, and R. Langtry, “Ten years of industrial experience with the sst turbulence model,” *Turbulence, heat and mass transfer*, vol. 4, no. 1, pp. 625–632, 2003.
- [68] H. G. Weller, G. Tabor, H. Jasak, and C. Fureby, “A tensorial approach to computational continuum mechanics using object-oriented techniques,” *Computers in physics*, vol. 12, no. 6, pp. 620–631, 1998.
- [69] F. Liu, “A thorough description of how wall functions are implemented in openfoam,” *Proceedings of CFD with OpenSource Software*, vol. 34, 2016.
- [70] B. M. C. Johnson, *Computational Fluid Dynamics (CFD) modelling of renewable energy turbine wake interactions*. PhD thesis, University of Central Lancashire, 2015.
- [71] F. Moukalled, L. Mangani, M. Darwish, F. Moukalled, L. Mangani, and M. Darwish, *The finite volume method*. Springer, 2016.
- [72] C. Hirsch, “Numerical computation of internal and external flows. vol. 2-computational methods for inviscid and viscous flows,” *Chichester*, 1990.
- [73] D. A. Jones, M. Chapuis, M. Liefvendahl, D. Norrison, and R. Widjaja, “RANS simulations using openFOAM software,” tech. rep., Defence Science and Technology Group Fishermans Bend Victoria Australia, 2016.

- [74] J. W. S. B. Rayleigh, *The Theory of Sound*, vol. 1 of *Cambridge Library Collection - Physical Sciences*. Cambridge University Press, 2011.
- [75] T. Caughey and M. E. O’Kelly, “Classical normal modes in damped linear dynamic systems,” *Journal of applied mechanics*, vol. 32, no. 3, pp. 583–588, 1965.
- [76] D. Inman, *Engineering Vibration*. Pearson Education, 2009.
- [77] N. M. Newmark, “A method of computation for structural dynamics,” *Journal of the engineering mechanics division*, vol. 85, no. 3, pp. 67–94, 1959.
- [78] G. Lindfield and J. Penny, *Numerical methods: using MATLAB*. Academic Press, 2018.
- [79] J. Leis, *Digital Signal Processing Using MATLAB for Students and Researchers*. Wiley, 2011.
- [80] O. Posdziech and R. Grundmann, “Numerical simulation of the flow around an infinitely long circular cylinder in the transition regime,” *Theoretical and Computational Fluid Dynamics*, vol. 15, no. 2, pp. 121–141, 2001.
- [81] E. Achenbach, “Distribution of local pressure and skin friction around a circular cylinder in cross-flow up to  $Re=5 \times 10^6$ ,” *Journal of Fluid Mechanics*, vol. 34, no. 4, pp. 625–639, 1968.